

TRANSPORT PROPERTIES OF  
WIDE BAND GAP SEMICONDUCTORS

A Thesis  
Presented to  
The Academic Faculty

By:

Louis Tirino III

In Partial Fulfillment  
Of the Requirements for the Degree  
Doctor of Philosophy in Electrical Engineering

Georgia Institute of Technology

May 2004

# Transport Properties of Wide Band Gap Semiconductors

Approved by:

Dr. Kevin F. Brennan, advisor

Dr. W. Russell Callen, Jr., co-advisor

Dr. Thomas K. Gaylord

Dr. David S. Citrin

April 1, 2004

**Press On. Nothing in the world can take the place of persistence. Talent will not; nothing is more common than unsuccessful men with talent. Genius will not; unrewarded genius is almost a proverb. Education alone will not; the world is full of educated failures. Persistence and determination alone are omnipotent.**

*Calvin Coolidge, 1872*

*For Karen,*

*with love.*

# ACKNOWLEDGEMENT

The simple truth is that I have only gotten to this point because of a tremendous amount of guidance, support, assistance, understanding, and love from some incredible people. If a person is the sum of all their experiences up to a particular point in time, then the following people are largely responsible for where I am now...good, bad, otherwise.

I cannot begin by thanking anyone other my advisor, Dr. Kevin F. Brennan. Not only was Kevin my advisor and mentor, for which he would deserve my unending gratefulness, but Kevin was there for me, and my family, as a friend. He did not believe that his duties as an advisor ended outside the classroom or lab. And through his own difficult times, he continued to teach everyone in his presence how to live life with dignity and determination. For all the work required for this dissertation, his greatest gift was teaching me what it means to be a success. Not a day passes that we do not miss you.

Dr. W. Russ Callen, you have been there in Kevin's absence as an advisor and friend as Kevin would have. I thank you for the incredible feedback you have provided, your time, patience, and energy. Thank you for helping me with the last mile.

Dr. Thomas K. Gaylord and Dr. David S. Citrin, thank you for your assistance on both my proposal and thesis committees. Thank you for your feedback and comments, and for fitting me in to your demanding schedules. It is my honor to have your names on my thesis.

I would like to thank Dr. Enrico Bellotti for his tremendous guidance over the course of the work that comprises this thesis. He has been an amazing collaborator, and I hope we can continue working together in the future. It would be difficult to list the

specific contributions he has made, because he has been there for me every step of the way. He is a great teacher, and he is my friend.

Dr. David R. Hertling, thank you for all of your help this past year. You have also been there in too many ways to count, but your help and advice will be forever appreciated and remembered.

Some of this work would have been much more difficult without the input of Dr. Michele Goano, and his assistance with many of the electronic band structures. *Grazie, Michele!*

Michael Weber, my colleague and friend, thank you. It has been my privilege to work with you. We have been through quite a bit together during these five or so years, and you helped make it so much easier. I already miss the fun we have had in the lab.

I would like to thank some of my friends, some of the best people I will ever meet, for all of their support. They have all been there in one way or another at some very important times. You know who you are, but for the record, thank you Greg Wohlford, Serge Georges, Mike Barrett, Byron Atcheson, Billy Bradach, and last, but *hardly* least, Craig Cappai. What more can I say?

I must thank Brian and Joan Sopp for their incredible support and love. Neither of you flinched when your new son-in-law decided to start this endeavor. Even more, you have treated me like your own son from the start. I will always be thankful for all of your help and understanding. We have all been through a tremendous amount the past few years, and both Karen and I would have had a hard time making it without you both. Thank you.

Thank you to my parents, Lou and Vita, my brothers, Mike and Joe. You have always believed in me. Mom and Dad, thank you for giving me every opportunity, for teaching me right from wrong, and for setting the examples I use to live my life every

day. All of my achievements, past, present, and future, have begun with your love and generosity. Thank you.

Finally, but without question most importantly, and with all of my love and thanks, to my wife Karen. It has been quite a wild ride, and I would have never required the assistance of most of the people I have thanked so far, if it were not for you. You are my inspiration, my muse. You have believed in me more than I may have deserved. I could struggle for another five years to try to find the words necessary to express my feelings for you and for what our marriage means to me, but I suspect you would like me to graduate...now. So instead, I hereby dedicate this document to you.

# TABLE OF CONTENTS

ACKNOWLEDGEMENT .....	V
TABLE OF CONTENTS .....	VIII
LIST OF TABLES .....	X
LIST OF FIGURES .....	XI
SUMMARY .....	XV
CHAPTER I .....	1
1.1 Wide Band Gap Semiconductors .....	1
1.2 History and Motivation .....	2
1.3 Initial Research .....	12
1.4 A Brief Look at Band Theory .....	16
CHAPTER II .....	20
2.1 Formulation of Phonon Mechanisms .....	20
2.2 Numerical Phonon Scattering Rate Expressions .....	21
2.3 Computational Requirements of Calculating Phonon Scattering Rates .....	25
2.4 Scattering Rate Calculation Parameters .....	31
CHAPTER III .....	34
3.1 Choice of Query Points .....	34
3.2 Material Parameters in Calculation of Scattering Rates .....	39
3.3 Calculation of Scattering Rates .....	40
CHAPTER IV .....	52
4.1 Impact Ionization .....	52
4.2 Impact Ionization Transition Rate .....	53
4.3 Impact Ionization Matrix Element .....	54
4.4 Calculation of Impact Ionization Transition Rate .....	56
CHAPTER V .....	61
5.1 Monte Carlo Simulator .....	61



5.2 Inputs: Band Structure and Pseudo Wave-Functions .....	63
5.3 Acoustic Deformation Potentials .....	64
CHAPTER VI.....	78
6.1 Temperature-Dependent Scattering Rates .....	78
6.2 Temperature-Dependent Impact Ionization Rates .....	81
6.3 Temperature-Dependent Transport Properties .....	83
6.4 More Temperature-Dependent Transport Properties of 3C-SiC .....	85
CHAPTER VII.....	99
7.1 Bipolar Simulations .....	99
7.2 General Bipolar Modifications to the Monte Carlo Simulator .....	100
7.3 Bipolar Impact Ionization Final States .....	101
7.4 Hole Transport in GaN-ZB .....	106
7.5 Avalanche Photo Diodes .....	109
7.6 APD Noise and Gain Theory .....	111
7.7 APD Results and Analysis .....	114
CHAPTER VIII.....	131
8.1 Summary of Results .....	131
8.2 Recommendations for Future Work .....	133
APPENDIX I .....	136
Derivation of Impact Ionization Matrix Element.....	136
REFERENCES.....	141

## LIST OF TABLES

Table 1: Parameters used in the calculation of the phonon scattering rates for the semiconductor systems discussed in this work. ....	40
Table 2: Acoustic deformation potential pairs obtained for the three semiconductor systems used in this work. ....	77
Table 3: Optical phonon energies for the three semiconductor systems used in this work. ....	80
Table 4: Sample sizes used in obtaining excess noise factors given the multiplication region size. ....	116

# LIST OF FIGURES

Figure 1: Material-theory-based modeling hierarchical chart. ....	11
Figure 2: Polar optical absorption in GaAs at $\Gamma$ ( $k = 0, 0, 0$ ). ....	26
Figure 3: Non-polar optical absorption in GaAs at $\Gamma$ ( $k = 0, 0, 0$ ). ....	28
Figure 4: Polar optical absorption in GaAs at low-energies. ....	29
Figure 5: Non-polar optical absorption in GaAs at low-energies. ....	30
Figure 6: Query points used in the calculation of electron-phonon optical scattering rates in GaAs [91]. ....	35
Figure 7: Electron query points for optical scattering rates in 3C-SiC. ....	36
Figure 8: Query points used in the calculation of electron-phonon acoustic scattering rates in GaAs. ....	38
Figure 9: Polar optical phonon scattering rate in GaAs. ....	42
Figure 10: Acoustic phonon scattering rate in GaAs. ....	43
Figure 11: Acoustic phonon scattering rate (absorption) in GaAs (red). The black points are densely packed and centered at 1 eV, 2 eV, and 3 eV. ....	44
Figure 12: Non-polar optical phonon scattering rate in GaAs. ....	45
Figure 13: Polar optical phonon scattering rate in 3C-SiC. ....	46
Figure 14: Acoustic phonon scattering rate in 3C-SiC. ....	47
Figure 15: Non-polar optical phonon scattering rate in 3C-SiC. ....	48
Figure 16: Polar optical phonon scattering rate in GaN-ZB. ....	49
Figure 17: Acoustic phonon scattering rate in GaN-ZB. ....	50
Figure 18: Non-polar optical phonon scattering rate in GaN-ZB. ....	51
Figure 19: Impact ionization transition rate for GaAs ....	58
Figure 20: Impact ionization transition rate for 3C-SiC. ....	59
Figure 21: Impact ionization transition rate for GaN-ZB ....	60
Figure 22: Logarithm of impact ionization coefficient in GaAs at an applied electric field strength of $350 \text{ kV/cm}$ as a function of the intra- and inter-band acoustic deformation potentials. ....	69
Figure 23: Impact ionization coefficient in GaAs at an applied electric field strength of $350 \text{ kV/cm}$ vs. the inter-band acoustic deformation potential as a function of the intra-band acoustic deformation potential. The dashed line represents the generally accepted value of the impact ionization coefficient at the applied field, while the	

black solid lines above and below represent 10% deviations of the accepted value.	70
Figure 24: Average particle energy in GaAs at an applied electric field strength of 350 $\text{kV}/\text{cm}$ vs. the inter-band acoustic deformation potential as a function of the intra-band acoustic deformation potential. The dashed line represents the generally accepted value of the average energy [24] at the applied field, while the black solid lines above and below represent 10% deviations of the accepted value.	71
Figure 25: Electron impact ionization coefficient vs. the inverse of the applied electric field in GaAs for several different pairs of acoustic deformation potentials. Also plotted is the theoretical work by M. Fischetti and S. Laux. The black lines represent the spread in reported impact ionization coefficients obtained by both experimental and theoretical methods.	72
Figure 26: Average carrier energy vs. applied electric field in GaAs for various pairs of acoustic deformation potentials. It is useful to notice that at these fields, there is a degree of insensitivity to the acoustic deformation potentials, indicating there is some room for error in exactly setting them.	73
Figure 27: Average carrier velocity vs. applied electric field in GaAs for various pairs of acoustic deformation potentials. It is useful to notice that, like the average energy, there is a degree of insensitivity to the acoustic deformation potentials, indicating there is some room for error in exactly setting them.	74
Figure 28: Average carrier velocity vs. applied electric field in 3C-SiC.	75
Figure 29: Electron impact ionization coefficient vs. the inverse applied electric field in 3C-SiC.	76
Figure 30: Total scattering rate for GaAs for the temperatures used in the bulk transport analysis simulations. Temperatures of 233K, 300K, 367K, and 433K were used.	88
Figure 31: Total scattering rate for GaN-ZB for temperatures used in the Monte Carlo transport analysis simulations. The total scattering rate is shown to rise with an increase in temperature. Temperatures of 300K, 367K, 433K, and 500K were used.	89
Figure 32: Total scattering rate for 3C-SiC for temperatures used in the Monte Carlo transport analysis simulations. The total scattering rate is shown to rise with an increase in temperature. Temperatures of 300K, 367K, 433K, and 500K were used.	90

Figure 33: Optical emission phonon occupancy number ( $N_{op}+1$ ) plotted versus temperature for GaAs, GaN-ZB, and 3C-SiC. ....	91
Figure 34: Impact ionization transition rate in GaAs at 233K and 433K.....	92
Figure 35: Impact ionization transition rate in GaN-ZB at 300K and 500K.....	93
Figure 36: Impact ionization transition rate in 3C-SiC at 300K and 500K. ....	94
Figure 37: Electron impact ionization coefficients in GaAs as a function of temperature. ....	95
Figure 38: Electron impact ionization coefficients in GaN-ZB as a function of temperature. ....	96
Figure 39: Electron impact ionization coefficients in 3C-SiC as a function of temperature. ....	97
Figure 40: Electron impact ionization coefficients in 3C-SiC as a function of temperature, with the additional temperature of 650K. ....	98
Figure 41: Energies of secondary electron and hole created from impact ionization event as a function of the energy of the initiating electron in GaN-ZB. ....	118
Figure 42: Energies of secondary electron and hole created from impact ionization event as a function of the energy of the initiating electron with fitting functions included for comparison. ....	119
Figure 43: Energies of secondary electron and hole created from impact ionization event as a function of the energy of the initiating hole in GaN-ZB. ....	120
Figure 44: Energies of secondary electron and hole created from impact ionization event as a function of the energy of the initiating hole with fitting functions included for comparison. ....	121
Figure 45: Total energy-dependent hole scattering rate in GaN-ZB including impact ionization. ....	122
Figure 46: Velocity v. electric field data for holes in GaN-ZB. The field range shown is the same as in [50] for comparison purposes.....	123
Figure 47: Average carrier energy v. electric field data for holes in GaN-ZB. The field range shown is the same as in [50] for comparison purposes.....	124
Figure 48: Hole impact ionization coefficient v. the inverse of the applied electric field in GaN-ZB using the unipolar impact ionization final state selector. The field range shown is the same as in [50] for comparison purposes.....	125
Figure 49: Comparison of bipolar and unipolar low-field hole velocity in GaN-ZB. ....	126

Figure 50: Comparison of bipolar and unipolar low-field hole average carrier energy in GaN-ZB.....	127
Figure 51: Mean electron gain for single electron injection into GaN-ZB multiplication regions of 0.125, 0.25, 0.50, and 1.00 $\mu\text{m}$ .....	128
Figure 52: Excess noise factor for single electron injection into GaN-ZB multiplication regions of 0.125, 0.25, 0.50, and 1.00 $\mu\text{m}$ .....	129
Figure 53: Standard deviation of gain as a function of multiplication region size.....	130

## SUMMARY

The objective of this research has been the study of the transport properties and breakdown characteristics of wide band gap semiconductor materials and their implications on device performance. Though the wide band gap semiconductors have great potential for a host of device applications, many gaps remain in the collective understanding about their properties, frustrating the evaluation of devices made from these materials.

The model chosen for this study is based on semiclassical transport theory as described by the Boltzmann Transport Equation. The calculations are performed using an ensemble Monte Carlo simulator. The simulator includes realistic, numerical energy band structures derived from an empirical pseudopotential method. The carrier-phonon scattering rates and impact ionization transition rates are numerically evaluated from the electronic band structure.

The Monte Carlo model is enhanced by removing all analytical assumptions about the material under investigation. In this way, the transport properties are essentially extracted from the electronic band structure. The analytical final-state selector, used after scattering events to determine the carrier's final state, is removed. In its place is a numerical final-state selector that relies solely on the states provided by the electronic band structure. In addition, the probability of a possible final state being selected is weighted based on the the overlap of the wave functions.

The bipolar final-state selector for impact ionization conserves energy and momentum. Secondary carrier energies are obtained directly from the band structure during the calculation of the impact ionization rates. In this way, carrier transport is described more accurately for electric fields well into breakdown.

It has been necessary to devise a computational method that yields the scattering and impact ionization rates both accurately and relatively quickly. The accuracy of the scattering rates is enhanced by both the inclusion of the full overlap integrals of the wave functions, and a judicious selection of the integration grid resolution. While an infinitely fine integration grid resolution would be preferable, it is not computationally feasible to use this approach. Therefore, the topic of the criteria used for the selection of the integration grid resolution is addressed in detail.

Several materials systems are discussed and compared. The temperature-dependent, high-field transport properties of electrons in gallium arsenide, zincblende gallium nitride, and cubic-phase silicon carbide are compared. A known figure of merit with regard to the high-field, breakdown properties of materials is the impact ionization coefficient as a function of the applied electric field. It is found that the impact ionization coefficients in gallium arsenide are very sensitive to changes in temperature, while they are relatively unaffected in silicon carbide. The root is traced to the sensitivity of the scattering rates, which is then a function of the magnitude of the phonon energy. Materials with large phonon energies, over the temperature range of interest, have total scattering rates that are insensitive to changes in the temperature, while the opposite is true of materials with small phonon energies. The high-field transport properties of the materials of interest are compared and discussed in detail.

Finally, the bipolar simulator is introduced for the simulation of devices whose performance is characterized by both electron and hole transport. In particular, the bipolar simulator is used in the study of the multiplication region of gallium nitride avalanche photodiodes as a function of the multiplication region thickness. Two important figures of merit in avalanche photodiodes are the noise and gain profiles as a function of the applied electric field. The gallium nitride multiplication regions are discussed for several thicknesses, and the results are discussed in detail. It is found,



and expected, that the thinner multiplication regions exhibit less noise. While the thinner multiplication is less noisy, that performance benefit is obtained at the expense of the requirement of a higher electric field to achieve a given gain. The simulations are performed as single-injection of electrons at near zero energy. It is possible, however, to inject holes as well. And either electrons or holes can be injected at any reasonable, user-defined energy.

# CHAPTER I

## 1.1 Wide Band Gap Semiconductors

Interest in the performance of wide band gap materials stems directly from known device limitations of silicon (Si) in the realm of high-frequency and high-power applications, and the use of these materials is improving many aspects of current electronics. The wireless communications market, for example, creates a demand for microwave transistors capable of high power densities. In addition, the data storage and optical communication systems markets have spurred the development of semiconductor materials used for blue- and ultraviolet-wavelength emitters and detectors. Therefore, the transport properties and breakdown characteristics of wide band gap semiconductor materials, including their implications on the performance of these materials in useful semiconductor devices, are of interest.

While these materials have great potential for a wide range of device applications, many gaps remain in the complete description of their transport properties, frustrating the evaluation of potential devices made from these materials. The lack of information about the wide band gap materials stems from their technological immaturity. It is difficult and expensive to produce reliably high-quality wide band gap material, given a technologically immature semiconductor system. The reasons include the lack of suitable substrates, difficulty in accurately controlling the growth processes, and general inexperience with these new systems.

To help account for this information void, a modeling technique known as material-theory-based modeling was developed. This approach makes it possible to obtain basic transport information directly from fundamental studies of the electronic band structure. That information, in turn, enables device-level simulations to be conducted. The approach makes it possible to study novel materials and to predict their

device behaviors without the need for experimental data. Though these theoretical results are not definitive, they provide an excellent means of understanding the intrinsic behaviors of materials under different conditions.

The basis for material-theory-based modeling is the determination of the electronic band structure. Once the band structure is determined, the phonon scattering rates and impact ionization transition rates can be calculated. All of the pieces necessary for determining the basic transport properties of the material are then available.

In this work, the basic transport properties are extracted from the electronic band structure and the associated scattering rates by an ensemble Monte Carlo simulator. The ensemble Monte Carlo simulator tracks the histories of several thousand charge carriers under the influence of an applied electric field. The information stored in the carrier histories can be interpreted to obtain the desired transport properties.

## **1.2 History and Motivation**

The definition and classification of a wide band gap semiconductor (WBGs) is not rigid; it may depend on the particular characteristics being considered for comparison. However, since many physical characteristics roughly scale with the energy gap, this parameter provides a reasonable classification vehicle. At the same time, direct comparison of the properties of a material to Si is natural; often, a material is classified as a wide band gap semiconductor if its energy band gap is at least twice the energy band gap of Si.

Following this guideline, the class of wide band gap semiconductors includes all materials with a band gap starting at roughly 2.0 eV, including indium nitride (InN) and

cubic phase silicon carbide (3C-SiC), up to materials such as aluminum nitride (AlN) and diamond, which have energy gaps on the order of 6.0 eV. The electronic band gap of gallium arsenide (GaAs) at room temperature is about 1.42 eV.

SiC has been recognized for a long time as a semiconductor of potential importance in advanced electronic applications [1, 2, 3, 4]. Because of its electronic properties, the possibility of easily growing a native oxide, and the presence of numerous polytypes, SiC can potentially be used in a wide range of applications including microwave and high-power devices.

Yet another material system, the III-Nitride family, has received considerable attention and development during recent years [5, 6]. Gallium nitride (GaN), indium nitride (InN), and aluminum nitride (AlN), including their alloys, are characterized by energy gaps spanning the range between 2.0 eV and 6.0 eV. In addition, since they have a direct band gap, the materials are well-suited for optoelectronic applications in the blue and ultraviolet portion of the electromagnetic spectrum; prior to the developments in these materials, this portion of the spectrum remained elusive to semiconductor-based devices.

One of the more important features of a semiconductor with a large band gap is the sustainability of a high breakdown field. A high breakdown voltage is associated with a large energy gap, which can be understood by examining the impact ionization transition rate. The relationship among impact ionization, breakdown, and the energy gap can be briefly summarized. Breakdown of a device occurs when charge-carriers begin to impact ionize, and secondary carriers are generated. The threshold of impact ionization is roughly scaled with the energy gap, and is near carrier energies of two times the band gap. Although this simplification omits some of the details, it is generally true that as the energy gap increases, the breakdown voltage increases correspondingly.

This important feature allows the design of power devices that can operate at much higher voltages. In addition, thermally generated leakage is drastically reduced, as compared to standard semiconductors, allowing devices to operate in high-temperature environments or in systems where leakage current negatively affects their performance, such as in photodetectors, charge-coupled devices (CCDs), and nonvolatile memories.

WBGs also tend to be characterized by a relatively high thermal conductivity, important for materials employed in power amplifiers or laser diodes or in hostile environments, such as engines. The WBGs usually have a smaller dielectric constant, which directly translates to devices with smaller parasitic components. While the low-field electron mobility is, in general, lower than that in currently used semiconductors, the hole mobility is at least comparable, and sometimes greater [6, 7]. WBGs also tend to have superior saturation velocities, which leads to potentially faster operating devices.

In optoelectronics, the large energy gap enables not only the fabrication of blue/UV emitters and detectors, but also the design of “solar blind” detectors, which are also much better radiation-hard performers. This final feature is important for devices intended for space-based applications.

GaAs fabrication and device technology can be considered mature today [8]. This technology has achieved excellent scalability and thermal management. GaAs-based devices offer impressive power performance from UHF to W-band frequencies, even in low-frequency applications. Below S-band, GaAs offers superior performance over other semiconductor technologies [8]. Above X-band, GaAs and InP HFETs and HBTs are the primary three terminal power devices available [8].

The  $\text{Al}_x\text{Ga}_{1-x}\text{As}/\text{GaAs}$  heterostructure system is useful for high-speed digital, high-frequency microwave, and electro-optic device applications [9]. In addition to the

higher-power applications where GaAs proves better suited than does Si, the presence of a direct band gap makes GaAs suitable for a host of optical applications.

While Si is the primary material used in solar cell applications, GaAs/AlAs alloys can potentially yield promising solar cell performance [10]. The excellent lattice match between the two materials yields heterostructures with low interface state densities and near-ideal properties [10]. The resulting band gap of the alloy (somewhere between that of GaAs and that of AlAs, depending on the mole fractions) suggests greater solar cell efficiencies, as well.

GaAs has been studied extensively [11, 12, 13, 14, 15], both theoretically and empirically. The use of GaAs in this work is twofold. First, as the numerical Monte Carlo simulator is developed, the simulation of GaAs allows a standard baseline to be set. Since there is ample information about the transport properties of GaAs, it will be possible to confirm that the simulator being developed is capable of providing reasonable data. Second, since it is a well-understood, representative cubic-phase material, it will then be possible to compare the results generated by the simulator to the results generated for other semiconductor materials.

SiC possesses a number of unique properties that make it a potential candidate for certain device applications [16]. It is resistant to high temperature and radiation, and is characterized as well by low diffusion rates of dopants. SiC polytypes have been recognized as one of the more promising material systems for high-frequency and/or high-power devices. The high breakdown field typical of these polytypes allows the design of metal-semiconductor field effect transistors (MESFETs) and metal-oxide semiconductor field effect transistors (MOSFETs) with high power densities, operated at very high frequencies.

The wireless market typically requires power amplifiers for base-station operation to perform effectively within the 100-1000 watt range [17]. Although silicon-based

devices have been employed for these applications, the use of SiC-based devices would reduce the number of devices needed to achieve a comparable output power, reducing costs and increasing reliability.

For devices required to operate at and beyond 2.5 GHz, silicon is no longer an option; GaAs and silicon germanium (SiGe) become possible alternatives. While these two materials are well suited for low- and medium-power microwave applications [18], SiGe would not, in particular, be able to provide the necessary power densities required in high-power situations. SiC-based devices are potential candidates for this class of systems. The advantage of SiC-based devices over III-V devices is that the required SiC technology is much simpler than that required to fabricate III-V-based high electron mobility transistors (HEMTs).

In recent years, SiC has been employed in the high-temperature electronics market, for example in the automotive market and in microelectrical mechanical systems (MEMS), where the superior structural properties of SiC are demanded.

There is an emerging commercial market for semiconductor optoelectronic devices, both emitters and detectors, which operate in the blue and ultraviolet regimes of the electromagnetic spectrum. Although GaN does not have as high a thermal conductivity as SiC, its other properties, such as breakdown field, saturation drift velocity, and carrier mobilities, compare favorably with SiC. This, too, makes it an attractive candidate for high-power, high-frequency applications.

The III-Nitride family of semiconductor materials includes AlN and InN, in addition to GaN, and their associated ternary combinations,  $\text{In}_x\text{Ga}_{1-x}\text{N}$ ,  $\text{Al}_x\text{Ga}_{1-x}\text{N}$ , and  $\text{In}_x\text{Al}_{1-x}\text{N}$ . These materials, in optoelectronic settings, provide wide spectral coverage, from the visible well into the far ultraviolet. Light emitting diodes (LEDs) based on the III-Nitride system can emit blue and green wavelengths through the ultraviolet portion of the electromagnetic spectrum. Green and blue LEDs can be used in flat-panel full-color all-

semiconductor displays. High power green, blue and, violet LEDs based on nitrides were first demonstrated by Nakamura et al. [19, 20].

The lifetimes of LEDs are more than an order of magnitude greater than the lifetimes of standard incandescent light sources. Moreover, LEDs consume 10-20% of the power consumed by light bulbs for the same luminous flux. Therefore, using nitride-based blue and green LEDs in combination with existing red LEDs makes full-color LEDs displays that can produce the entire visible spectrum possible. Already, red LEDs are used in traffic signals. In the past, incandescent bulbs were used and filtered to emit only red (or yellow or green) light. The use of a red LED is more efficient in this case.

There is a keen need for photonic emitters in the blue and ultraviolet portions of the spectrum. Aside from the obvious usage as a blue light emitter, the development of a blue or ultraviolet light source is of great importance in other applications. Of principal importance is the development of a coherent blue light source for laser printing, and as a read/write laser source for high-density optical mass storage systems. Shorter wavelength emitters extend the diffraction limit for optical systems, thus enabling far more compact storage of information.

Most device simulation packages, such as drift-diffusion and hydrodynamic models [21], require a detailed and accurate accounting of the transport parameters at the macroscopic level. While these simulators can often provide an accurate estimate of device behavior that can be directly compared to experiment, they rely on knowledge of parameters that need to be determined beforehand from either experiment or from other computational techniques. Of greatest importance as input parameters to these simulators are quantities such as the carrier mobilities, diffusivities, drift velocities, and carrier lifetimes, among others.



For WBGS, where the averaged macroscopic transport properties are either unknown, or at best, poorly known, application of drift-diffusion or hydrodynamic simulators is hampered. Therefore, a more fundamental approach is needed for the study of carrier transport and device operation in novel, emerging semiconductor materials.

As Fischetti et al. [22, 23, 24] have discussed, an accurate accounting of the physics that govern submicron device behavior requires a full-band ensemble Monte Carlo simulator. The approach utilizing the full-band structure was pioneered [24] by Hess [25, 26] and demonstrated in Si and GaAs and extended to other III-V compounds [27, 28], and to the noncubic semiconductor regime as well [29, 30], by Brennan.

The Boltzmann transport equation provides a comprehensive description of the carrier transport dynamics within a semiconductor under semi-classical conditions. Given the general complexity of the Boltzmann equation, one of the more useful approaches for its solution is the numerical Monte Carlo method [31]. The Monte Carlo method provides a direct solution of the Boltzmann equation through microscopic simulation of the trajectories of particles subject to the band structure, scattering mechanisms, applied potentials, and fields, as well as device geometries, if applicable [32].

The Monte Carlo method has been successfully employed to investigate a great variety of transport properties in semiconductors [33]. Subjected to the force of applied, external electric fields, the charge carriers follow trajectories determined by Newton's law [33]. The drift process is interrupted by scattering events that are considered to be local in space and instantaneous in time.

A fundamental advantage of the Monte Carlo method is that it provides a first-principles transport formulation based on the exact solution of the Boltzmann equation limited only to the extent by which the degree of underlying physics is included [32].

Although other techniques have been used to solve the Boltzmann equation [34, 35, 36], the Monte Carlo solution is the most common. Its ease of use and overall simplicity help make it the tool of choice.

This work applies material-theory-based modeling [32, 37, 38, 39] to the study of certain WBGS of interest. This technique provides a fundamental modeling methodology useful in the study of immature material systems. Figure 1 illustrates the modeling technique in the form of a hierarchical chart.

The first step deals with the calculation of the electronic band structure of the material under investigation. The band structure can be obtained either via empirical or *ab-initio* techniques. The former requires experimental information that is not always available for emerging materials. This information becomes more critical as the need to optimize the band structure increases [40].

Often, when it is not at all possible to obtain information to produce a reliable empirical band structure, the application of *ab-initio* methods makes it possible to calculate, at the least, a basic set of data that can be used as a starting point for empirical methods. In the past, producing a full-band structure with *ab-initio* methods was prohibitively time consuming and computationally intensive. Recent progress has been made, however, calculating *ab-initio* band structures [41].

To determine the transport properties of a material, it is necessary to describe the interaction between carriers and the semiconductor lattice. Techniques of different levels of sophistication can be employed to perform this task. Lattice dynamics, which describes the phonons, can be evaluated either analytically or numerically. The knowledge of the electronic structure and the lattice dynamics allows the carrier-phonon interaction to be determined. The final step of the method deals with the calculation of the transport properties and parameters that can subsequently be used in macroscopic simulators.

Four boxes in Figure 1 are related to the subject of this work. These boxes are highlighted with the double border; in particular, they are the calculation of the phonon scattering rates, the Monte Carlo calculation of the bulk transport parameters (two boxes), and the Monte Carlo device simulation.

While the calculation of the electronic band structure is necessary to this work, it is not the subject. Band theory is a complicated topic with many different approaches. The references listed here [42 -- 55] hardly scratch the surface of the subject. However, a (very) brief discussion will be given later in this chapter.



### 1.3 Initial Research

The determination of the potential to which a carrier is exposed within a semiconductor lattice is primarily the subject of the calculation of the electronic band structure. The subject of electronic band structure theory concerns the treatment of the electronic structure of the lattice and the creation of an appropriate Hamiltonian, which is used to solve the Schrödinger equation for a carrier wave function. The Born-Oppenheimer approximation is used to decouple the core and electronic parts of the total Hamiltonian. Since only the electronic structure is of interest, only the electronic parts of the Hamiltonian with cores assumed frozen in their equilibrium positions, are considered. This assumption implies that the lattice is at zero temperature.

In reality, however, the cores are not frozen in their equilibrium positions, and the effect of the core deviations from equilibrium is non-negligible. A lattice can be thought of as a collection of mass centers situated at definite positions and held together by the action of some elastic restoring force. There is a minimum potential energy to the system, and as a consequence, the system can oscillate as a harmonic oscillator about the equilibrium if it is slightly perturbed. The full details of the physics and the accompanying mathematics of the lattice vibrations can be found in texts such as Brennan [56] or Ridley [57].

To calculate the phonon scattering rates, several numerical considerations must first be addressed. After the rates are calculated and discussed, attention will be turned to the bulk Monte Carlo simulator itself. Most Monte Carlo simulation tools rely on some degree of parameterization, such as deformation potentials that are often not obtainable from experiment, are generally assumed direction and energy independent, and not readily found from theory.

Consequently, most of these parameters are chosen either to fit experimental results or, when experimental data are unavailable, a best estimate of their values is used instead. It is one of the goals of this thesis to introduce a fully numerical Monte Carlo routine that has only one adjustable, unknown parameter, the acoustic deformation potential, and to illustrate how its magnitude can be selected in a systematic manner.

Though the value of the acoustic deformation potential, in principle, can be determined from the use of a rigid ion model of the band structure, in practice such an approach is computationally demanding, since it generally requires calculation of the deformation potential as a function of direction and energy. Following the standard paradigm, an averaged constant value of the deformation potential is used instead [58]. A systematic approach for the selection of the acoustic deformation potential will be presented. The model is used to obtain the values of the acoustic deformation potential for GaAs, 3C-SiC, and GaN-ZB.

Once the acoustic deformation potentials have been selected, the attention will turn to transport properties, particularly the impact ionization coefficients. Much work has been done, both experimentally and theoretically [24, 59 — 72] on the determination of the impact ionization coefficients of various semiconductors. The impact ionization coefficients of a semiconductor are a useful tool in understanding the breakdown properties of a material under high electric field conditions.

High electric fields are typically encountered in device applications such as high-power metal-semiconductor field-effect transistors (MESFET), high-power switching diodes, and in avalanche photodiodes (APDs). Since there is some non-zero resistance to these materials, some portion of usable output power is lost to device heating. As the device heats up, the electrical properties of the material change.

An increased operating temperature is an important consideration of high-power, high-frequency transistors used for power amplifiers. In these applications, the high current densities of these devices result in significant Joule heating. Consequently, even with heat sinking, the temperature of the device increases significantly. Therefore, it is important to understand how high operating temperatures affect the performance of these devices, particularly their breakdown characteristics.

The interest in the wide band gap semiconductors, such as GaN, AlN, their related ternary alloys and SiC in high-power, high-frequency-transistor applications [73 - 82], has already been mentioned. In many of these applications, the operating temperature is much higher than room temperature because of either Joule heating or operation in a high-temperature environment, such as automobile or jet engines. The workings of these devices at elevated temperatures are consequently of great importance.

One of the more important characteristics of power transistors is their breakdown behavior. The maximum output power is restricted by the breakdown voltage of the device. Knowledge of the breakdown behavior, particularly at high operating temperatures, is then of great importance in understanding the limitations of power devices. Though some work has been done in the past on the temperature dependence of the impact ionization coefficients [24, 59, 83], there has been no thorough study and comparison of the temperature dependence of the impact ionization coefficients in the wide band gap semiconductors.

A comprehensive study of the temperature dependence of the impact ionization coefficients in representative cubic-phase, wide band gap semiconductors will be presented. The behavior of the wide band gap materials will be compared to that of bulk GaAs.

On the atomic scale, thermal power dissipation is captured in the details of both carrier-phonon scattering and impact ionization events. A change in the temperature will affect both the phonon scattering rate and the impact ionization transition rate. As is generally known, an increase in the temperature leads to a decrease in the energy gap and consequently the impact ionization transition rate turns on at a lower energy. In contrast, increasing temperature increases the phonon scattering rate, which acts to cool the carrier distribution.

The interplay of these two mechanisms with respect to temperature has a direct effect on the impact ionization coefficients. The choice of the materials studied here will be particularly fortunate because of the range of values of their phonon energies. Their temperature-dependent performance illustrates a trend in the behavior of materials at various temperatures.

The low phonon energy of GaAs produces a large change in the impact ionization coefficients at elevated temperatures. Conversely, the high phonon energy of 3C-SiC produces a meager change in the impact ionization coefficients at higher temperatures. The phonon energy of GaN-ZB, which is more than 2.5 times higher than the phonon energy of GaAs, results in impact ionization coefficients that decrease much less with temperature than those for GaAs.

Therefore, there will be several parts to this research. First is the calculation of the numerical phonon scattering rates, which includes the solution to the inherent computational difficulties. Then, the numerical, bulk Monte Carlo simulator will be devised with the adjustable acoustic deformation potential. The acoustic deformation potentials will be chosen in a systematic fashion for GaAs, GaN-ZB, and 3C-SiC. The effect of temperature on the scattering rates will be addressed. The temperature-dependence of the phonon scattering rates will be incorporated into a comprehensive study of the high-field transport properties of the three subject semiconductor materials.



The final area of research to be examined is twofold. First, the Monte Carlo simulator will be enhanced to allow both carrier species to be simulated simultaneously. This will require several modifications to the single carrier species simulator, including a new formulation of the final state selector for impact ionization processes. Once the bipolar simulator has been implemented, the research will examine the performance of the multiplication region of APDs. The multiplication region of an APD plays a crucial role in determining the overall gain and multiplication noise of the entire device [84]. Gain in an APD is dictated by the magnitude of the impact ionization rate of the injected carrier species, while the noise is closely related to the variance of the gain. The bipolar simulator is used to examine the gain and noise characteristics of intrinsic GaN-ZB multiplication regions as a function of the region thickness.

There is good chemical stability and a wide, direct electronic energy band gap in nitride-based semiconductor systems. Therefore, GaN-based APDs are of interest in photodetector applications operating in the ultraviolet (UV) region of the electromagnetic spectrum [85].

## **1.4 A Brief Look at Band Theory**

The fundamental basis for the theoretical examination of the electrical transport properties is the electronic band structure. The basic problem to be addressed by the determination of the electronic band structure is that a many-electron system within a periodic potential must be solved. While quantum mechanics allows, in principle, that a solution exists, no closed-form solution is obtainable due to computational constraints; drastic simplifications must be introduced [39]. Two different approaches, which lie at opposite ends of the spectrum of possible methods, are the empirical pseudopotential

method (EPM) and the linear augmented plane wave method (LAPW) within the framework of density functional theory (DFT).

The essential difference between the two approaches is the manner in which the core states, those related to the ionic charge and filled valence shells, are treated. The Born-Oppenheimer approximation is used to de-couple the core and electronic parts of the total Hamiltonian, since it is the electronic part that ultimately facilitates the production of the band structure. The Hartree mean field approximation is then used to reduce the many-electron problem down to a single-electron problem. The problem is now tractable, and all that remains is an expression for the ionic potential seen by the electrons.

The construction of a pseudopotential has been made possible by a simple technique known as the Phillips-Kleinman cancellation theorem. The details have been omitted, but can be found in [56], among other places. From this approach, two classes of techniques can be used in the construction of the pseudopotential, the *ab-initio* pseudopotential and the empirical pseudopotential [39]. The *ab-initio* methods build the pseudopotential in a self-consistent fashion by the simultaneous solutions of the Poisson and Schrödinger equations.

The empirical pseudopotential is built differently. Available experimental data are used as fitting parameters. Examples of experimental data used in the construction of the empirical pseudopotential are measured energy gaps, the dielectric response, and effective masses [39]. The relative simplicity of EPM compares favorably with the relative accuracy of the band structure it produces.

With EPM, the total crystal potential is determined by fitting the band structure to experimental data [39]. The use of LAPW in the context of DFT, however, starts with the electronic structure of the atoms present in the semiconductor material.

The basic theorems of the DFT deal with the solutions of the many-body problem for an electronic system by using the charge density as the quantity that describes the electronic properties of the system. In principle, the many-body problem can be solved by finding a method to determine the charge density that minimizes the total energy [39]. LAPW is a method that is used to construct expressions for the ionic potential and the wave functions. The description of the electronic structure is self-consistent and begins with an initial guess for the wave function. From this point, the charge density and potentials are calculated. The process is iterated until some convergence criteria are satisfied.

Computationally, the LAPW method is much more demanding than EPM. As such, the inclusion of LAPW in transport simulators is hampered, although recent progress has been made. In [86], the authors employ a DFT-computed band structure, however, it is done with the use of the local density approximation (LDA), as opposed to LAPW. Nevertheless, it is a powerful tool in the computation of band structures, particularly for materials where very little experimental data is available, leaving EPM calculations frustrated. Also, LAPW can be extremely useful in computing highly complicated band structures.

Another method that bears mention, particularly for its application to band structures calculated using the LAPW method, is known as the ***k*·*p*** method. The ***k*·*p*** method has been used alone in order to derive a Hamiltonian and the associated band diagram [53]. Due to some intrinsic properties of the technique, it is particularly useful at investigating valence bands [87, 88]. In addition, it can be used as an interpolation method in conjunction with LAPW.

Thus, the choice of EPM as the band structure technique in this work is due to its relative simplicity and accuracy, as well as its smooth integration into the Monte Carlo simulator. The accuracy afforded by the quadratic interpolation method [24] (to be

discussed further in Chapter V) provides further evidence to its value. Excellent discussions on the state-of-the-art in band structure calculations as computed for GaN-ZB [89] and 3C- and 2H-SiC [90] via different methods, including EPM and DFT, among other techniques, are available in the relevant literature.

## CHAPTER II

### 2.1 Formulation of Phonon Mechanisms

The semiconductor crystal lattice and the corresponding potential it poses to a charged carrier are not perfect. There are several mechanisms by which the crystal is disturbed from its equilibrium, one of which is lattice oscillations. The atoms at the lattice sites may oscillate about their equilibrium positions, disturbing the perfect lattice potential. Then, the potential seen by carriers is no longer perfectly uniform for all times.

Other disturbances can cause the lattice atoms to deviate from their equilibrium positions as well. For example, the presence of a foreign atom, in either an interstitial or substitutional site, can cause a change to the otherwise perfect lattice potential. Dislocations and/or deformities in the lattice will also upset the lattice potential. And last, though not least, the physical surface of the end of a device will cause the long-range crystal properties to be violated, also resulting in a change in the lattice potential.

Generally, the effect of lattice vibrations on the motions of electrons in a crystalline solid can be treated with perturbation theory. It is assumed that the effect of lattice vibrations on the electron dynamics is sufficiently weak such that a first-order perturbation treatment is acceptable [56]. The transition rate from one electron-state to another as a result of a phonon interaction is specified by Fermi's golden rule:

$$W_{kk'} = \frac{2\pi}{\hbar} \left| \langle n'k' | V | nk \rangle \right|^2 \delta(E_{n'k'} - E_{nk}) \quad (1)$$

The transition rate is  $W$ , where  $nk$  is some definite initial state, and  $n'k'$  is some definite final state. The components of a state,  $nk$ , contain all of the information necessary to completely describe the precise state of a carrier. The momentum of a particle is denoted by  $k$ , the wave vector, and the band index is denoted by  $n$ . The perturbation is given by  $V$ , and the delta function conserves energy between the initial

and final states. This interaction is the adiabatic electron-phonon interaction and it is weak enough for  $V$  to be regarded as a small perturbation, which in the usual way induces transitions between unperturbed states [57].

## 2.2 Numerical Phonon Scattering Rate Expressions

To obtain the numerical expressions for the phonon scattering rates of interest, it is necessary to express (1) in a form that describes the desired lattice vibration in a manner that can be evaluated numerically. To begin, the perturbation,  $V$ , is formulated for each of the scattering mechanisms; there will be  $V_{PO}$ ,  $V_{NP}$ , and  $V_{AC}$  for the polar optical, non-polar optical, and acoustic perturbations, respectively. The precise formulations for the perturbations are derived and can be found in Brennan [56] or Ridley [57].

From the perturbations, it is possible to obtain the probability of a scattering event from one initial state,  $n\mathbf{k}$ , to some final state,  $n'\mathbf{k}'$ . Folding the band indices into the wave vector, the probability of a scatter from  $\mathbf{k}$  to  $\mathbf{k}'$  is noted as  $P(\mathbf{k}, \mathbf{k}')$ . The total scattering rate, then, is obtained by integrating  $P(\mathbf{k}, \mathbf{k}')$  across all possible initial and final states in momentum space.

The probability of a polar optical scatter,  $P_{PO}(\mathbf{k}, \mathbf{k}')$  is

$$P_{PO}(k, k') = \frac{2\pi}{\hbar} \frac{2\pi e^2 \hbar \omega_{PO}}{4\pi V q^2} \left( \frac{1}{\epsilon_\infty} - \frac{1}{\epsilon_0} \right) I(k, k') \left[ N_{OP} + \frac{1}{2} \pm \frac{1}{2} \right] \delta(E_f - E_i \pm \hbar \omega_{PO}) \quad (2)$$

The term  $e^2$  is the square of the unit of electrical charge, while  $q^2$  is the square of the magnitude of the  $\mathbf{q}$ -vector between initial and final states. The volume of the Brillouin zone,  $V$ , is included, and not to be confused with the perturbation. The polar optical phonon energy, which is assumed constant, is  $\hbar \omega_{PO}$ . The static and high-

frequency dielectric values are expressed as  $\epsilon_0$  and  $\epsilon_\infty$ , respectively, and the term  $I(\mathbf{k}, \mathbf{k}')$  is the squared overlap of the Bloch initial and final states. The phonon occupancy number is  $N_{OP}$  and is consistent with the statistical mechanics of bosons:

$$N_{OP} = \frac{1}{e^{\frac{\hbar\omega}{kT}} - 1} \quad (3)$$

Finally, the  $\pm$  term applies to emission and absorption mechanisms, respectively. The total rate is found by integrating  $P_{PO}(\mathbf{k}, \mathbf{k}')$  over all possible states in the Brillouin zone:

$$\frac{1}{\tau_{PO}} = \frac{V}{8\pi^3} \int_{V_{BZ}} P(k, k') d^3k \quad (4)$$

Substituting for  $P_{PO}(\mathbf{k}, \mathbf{k}')$  into (4) gives

$$\begin{aligned} \frac{1}{\tau_{PO}} = \frac{V}{8\pi^3} \int_{V_{BZ}} \frac{2\pi}{\hbar} \frac{2\pi e^2 \hbar \omega_{PO}}{4\pi V q^2} \left( \frac{1}{\epsilon_\infty} - \frac{1}{\epsilon_0} \right) I(k, k') \\ \left[ N_{OP} + \frac{1}{2} \pm \frac{1}{2} \right] \delta(E_f - E_i \pm \hbar \omega_{PO}) d^3k \end{aligned} \quad (5)$$

Recalling that  $N_{OP}$  is constant, since the polar optical phonon energy is assumed constant, the terms are rearranged by taking all constant terms outside of the integral.

This produces the final expression for the polar optical scattering rate:

$$\frac{1}{\tau_{PO}} = \frac{e^2 \omega_{PO}}{8\pi^2} \left( \frac{1}{\epsilon_\infty} - \frac{1}{\epsilon_0} \right) \left[ N_{OP} + \frac{1}{2} \pm \frac{1}{2} \right] \int_{V_{BZ}} \frac{I(k, k')}{q^2} \delta(E_f - E_i \pm \hbar \omega_{PO}) d^3k \quad (6)$$

Unfortunately, (6), like the expressions for all of the scattering rates, cannot be solved analytically; it must be done numerically. The reason is the  $E(\mathbf{k})$  dispersion relation. Since the electronic band structure is not a function, it is necessary to find the pairs of wave vectors that satisfy the energy delta function manually. This is a time-consuming process and will be addressed in detail further in the chapter. To transform

(6) into an equation that can be solved numerically, it is necessary to make it a discrete summation within discretized momentum space. This transformation is shown here:

$$\frac{1}{\tau_{PO}} = \frac{e^2 \omega_{PO}}{8\pi^2} \left( \frac{1}{\epsilon_\infty} - \frac{1}{\epsilon_0} \right) \left[ N_{OP} + \frac{1}{2} \pm \frac{1}{2} \right] \sum_{BZ} \frac{I(k, k')}{q^2} \delta(E_f - E_i \pm \hbar \omega_{PO}) \Delta^3 k \quad (7)$$

By correctly obtaining  $P_{NP}(\mathbf{k}, \mathbf{k}')$  and  $P_{AC}(\mathbf{k}, \mathbf{k}')$  for non-polar optical and acoustic scattering, the scattering rates can be obtained in the same fashion as was done for the polar optical scattering rate. The details of the derivations are nearly identical, so the expressions for the total rates only will be presented. The non-polar optical phonon scattering rate is

$$\frac{1}{\tau_{NP}} = \frac{\pi (D_t k)^2}{(2\pi)^3 \rho \omega_{NP}} \left[ N_{OP} + \frac{1}{2} \pm \frac{1}{2} \right] \sum_{BZ} I(k, k') \delta(E_f - E_i \pm \hbar \omega_{NP}) \Delta^3 k \quad (8)$$

In (8), several terms appear that were not present in the polar optical scattering rate. The density,  $\rho$ , of the material is in the denominator of the first term. The non-polar optical phonon energy is now  $\hbar \omega_{NP}$ , and  $D_t k$  is the optical deformation potential field.  $N_{OP}$  is formulated in the same way as was done for the polar optical scattering rate; however the two values,  $N_{OP, polar}$  and  $N_{OP, non-polar}$ , may not be equal since the phonon energies may not necessarily be equal.

Integrating  $P_{AC}(\mathbf{k}, \mathbf{k}')$  yields the acoustic phonon scattering rate:

$$\frac{1}{\tau_{AC}} = \frac{\pi E_1^2}{(2\pi)^3 \rho} \sum_{BZ} \left[ N_{AC}(q) + \frac{1}{2} \pm \frac{1}{2} \right] \frac{q^2 I(k, k')}{\omega(q)} \delta(E_f - E_i \pm \hbar \omega_{AC}(q)) \Delta^3 k \quad (9)$$

In the numerator of the term before the summation,  $E_1$  is the acoustic deformation potential. In practice, two acoustic deformation potentials,  $E_1$  and  $E_2$ , are used.  $E_1$  is the intraband deformation potential, and  $E_2$  is the interband deformation potential. The intraband deformation potential is used for scattering transitions within the lowest conduction (or highest valence) band, while the interband deformation potential is



used for all other transitions. The use of the deformation potentials will be addressed later in considerable detail.

Unlike the cases of the optical phonon mechanisms, the acoustic phonon energy is not constant. Instead, the acoustic phonon energy contains a  $\mathbf{q}$ -dependence.

Therefore,  $N_{AC}(\mathbf{q})$  and  $\hbar\omega_{AC}(\mathbf{q})$  are calculated for each potential initial and final wave vector pair. While  $N_{AC}(\mathbf{q})$  has the same form as the phonon occupancy numbers for the optical phonon mechanisms, it is re-evaluated each time a phonon energy is calculated. The acoustic phonon energy is calculated as:

$$\hbar\omega(q) = \begin{cases} \hbar\omega_{\max} \sqrt{1 - \cos\left(\frac{qa}{4}\right)} & \text{for } q < 1.0 \\ \hbar\omega_{\max} & \text{otherwise} \end{cases} \quad (10)$$

Where:

$$\omega_{\max} = \frac{4v_l}{a} \quad (11)$$

In (11),  $a$  is the lattice constant, and  $v_l$  is the longitudinal sound velocity.

The calculation of the acoustic phonon scattering rate is extremely time-consuming as a direct result of the non-constant acoustic phonon energy. For a given initial wave vector, one possible final wave vector is selected from all possible final wave vectors in the irreducible wedge. The phonon energy,  $\hbar\omega_{AC}(\mathbf{q})$ , is calculated based on  $\mathbf{q}$  between the wave vectors. If the combination of the initial state, final state, and phonon energies satisfies the energy conservation requirements for either absorption or emission, the phonon occupancy number is calculated along with the rest of the terms in the rate. These additional calculations and conservation checks add considerably to the computation time.

## 2.3 Computational Requirements of Calculating Phonon Scattering Rates

The three scattering rate equations, which are comprised of absorption and emission processes, have several features in common. First, it is possible to combine several terms in the equations into a constant pre-factor, which is computed once, and multiplied by the results inside of the summation.

The difficulty in computing the rates, however, is owed to terms inside the summations. Within the summations, all of the equations have three terms in common: the squared overlap of the Bloch states,  $I(\mathbf{k}, \mathbf{k}')$ , the Dirac delta function,  $\delta(E_f - E_i \pm \hbar\omega)$ , and the integration grid resolution,  $\Delta^3\mathbf{k}$ . The polar-optical rate contains an additional  $\mathbf{q}$ -dependent term. There are no additional terms for the non-polar rate, while the acoustic rate is laden by multiple  $\mathbf{q}$ -dependent terms.

In general, the  $\mathbf{q}$ -dependent terms are individually composed of a few terms, and are computationally burdensome because of the number of times the calculations are required. The overlap integral is also burdensome as a result of the number of times the calculation must be performed, but it is also itself a time consuming calculation. Each overlap integral is the product of two matrices, which are each (113x2). The matrices in the overlap integral are the wave functions for both the initial and final  $\mathbf{k}$ -points in the calculation.

The true computational difficulty, however, lies in the Dirac delta function, the integration grid resolution, and their relationship to each other. The complication posed by the Dirac delta function is twofold. First, the delta function cannot be solved explicitly because it relies on the energy-momentum dispersion relationship revealed by the electronic band structure. Solving the delta function, then, requires knowledge of all possible final and initial points with energies that satisfy the delta function. These pairs cannot be known *a priori*; instead they are found manually. This is a time consuming

process, further complicated by the relationship between the delta function and the integration grid resolution, as shown in Figure 2.

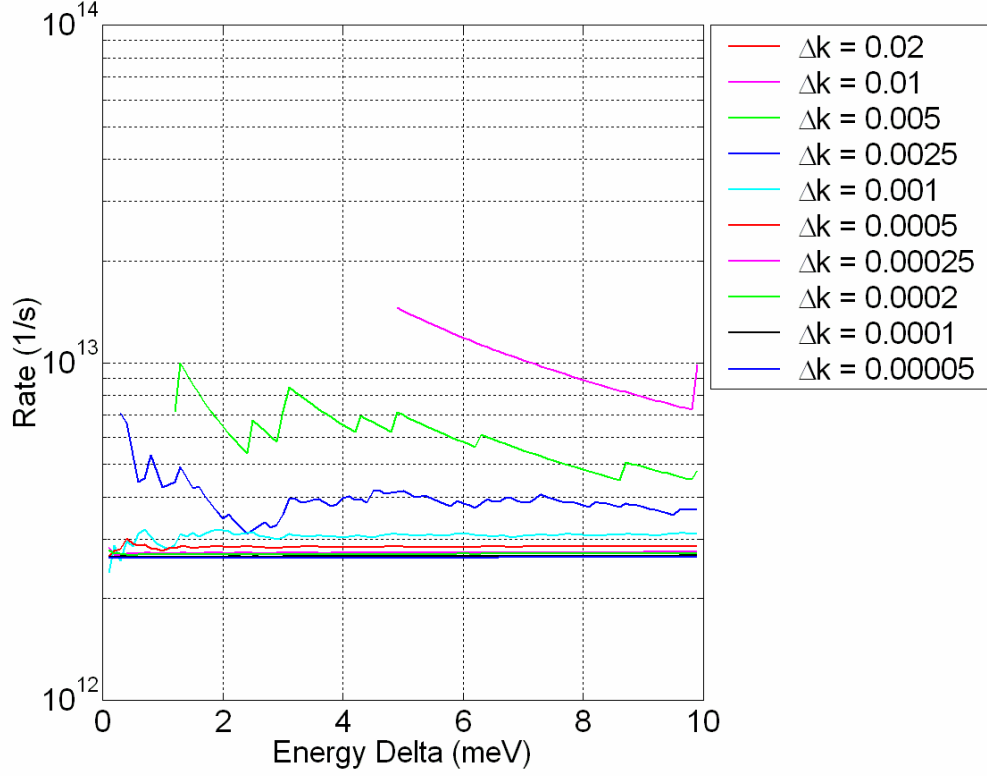


**Figure 2: Polar optical absorption in GaAs at  $\Gamma$  ( $k = 0, 0, 0$ ).**

The integration for the scattering rates is performed over a discrete grid in three-dimensional momentum space. Realistic grid resolutions forbid the Dirac delta function from being satisfied exactly as  $\delta(E_f - E_i \pm \hbar\omega)$ . In practice, the delta function is  $\delta(E_f - E_i \pm \hbar\omega \pm E_D)$ , where  $\pm E_D$  is the “Energy Delta” shown on the x-axis in Figure 2. The energy delta can be thought of as a tolerance parameter, which assists the conservation of energy in discrete space. In Figure 2 the polar optical phonon absorption rate in GaAs at  $\Gamma$  is illustrated as a function of the grid resolution and the tolerance level in the Dirac delta function.

Three observations are made. First, as the energy delta gets larger, the noise in the value of the rates decreases. Second, as the resolution of the grid becomes finer, the value of the rate converges to some value. Third, by combining the first two observations, it is clear that at sufficiently fine grid resolutions, the dependence on the energy delta disappears. Since the inclusion of the energy delta arises from numerical considerations and is not a physical parameter, the rate should be independent of this parameter.

A large energy delta, particularly one that is unnecessarily large, only serves to make the computation more time consuming, since more initial and final point pairs must be used in any  $q$ -dependent calculations. The dependence of the rate on the energy delta appears to be removed with integration grid resolutions finer than  $\Delta k = 0.0025$ .

Analytical approximations for the scattering rates have been used in the past [25, 48]. The analytical approximations were derived by making assumptions about the shape of the band structure at low energies. Therefore, these analytical approximations were shown to provide good results in bulk studies at low energies. The polar optical scattering rate given a non parabolic band structure is given as [48, 56]

$$\frac{1}{\tau_{PO}} = \frac{q^2 \sqrt{m} \omega_0}{4\pi\epsilon_0 \sqrt{2} \hbar} \left[ \frac{1}{\epsilon_\infty} - \frac{1}{\epsilon_0} \right] \frac{1}{\sqrt{E}} \ln \left| \frac{\sqrt{E} + \sqrt{E'}}{\sqrt{E} - \sqrt{E'}} \right| \left\{ \frac{N_0}{N_0 + 1} \frac{absorption}{emission} \right\} \quad (12)$$

In GaAs, the analytical rate of  $2.63 \times 10^{12}$  1/s is approached at  $E = 0.0$  eV as the grid resolution becomes finer than  $\Delta k = 0.0025$  [91]. The same convergence results can be seen with the non-polar optical phonon scattering rate in Figure 3.

The importance of the grid resolution is evident at energies greater than 0.0 eV as well. In Figure 4, the polar optical phonon absorption rate is shown in the low-energy regime.

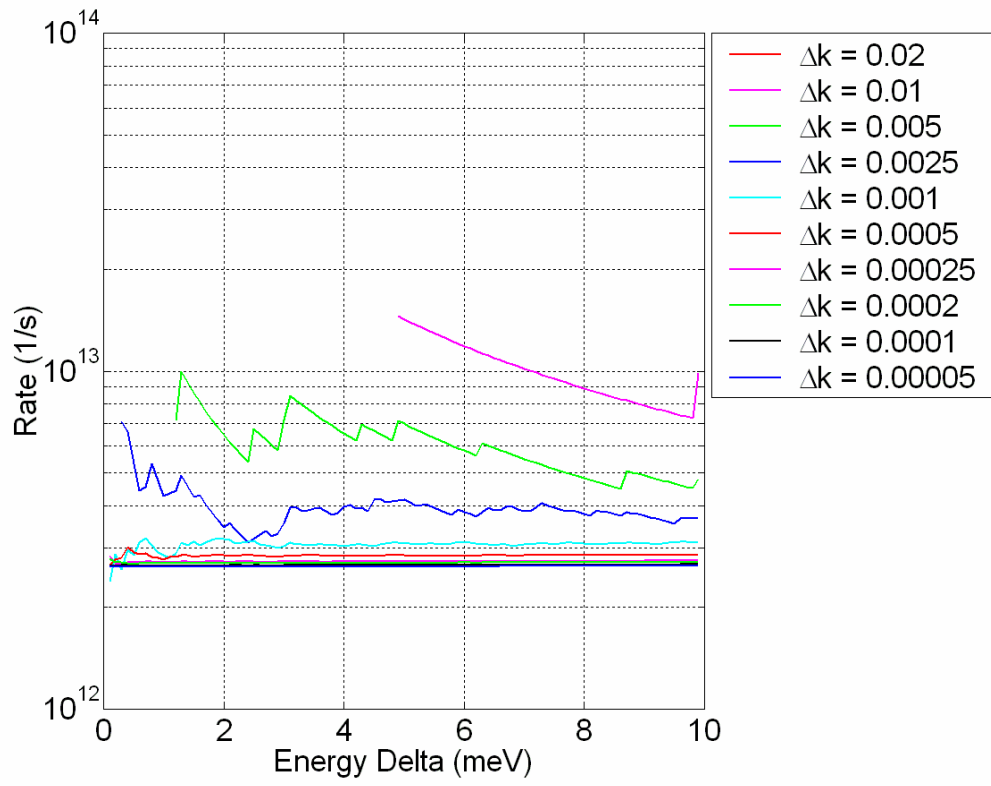


**Figure 3: Non-polar optical absorption in GaAs at  $\Gamma$  ( $k = 0, 0, 0$ ).**

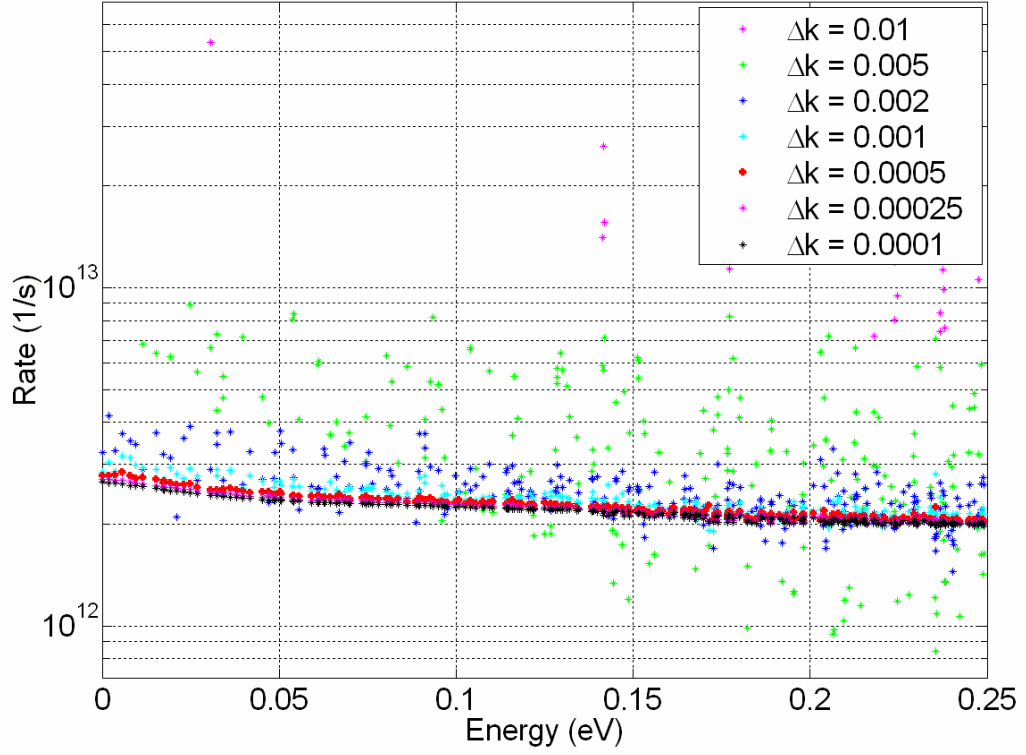


**Figure 4: Polar optical absorption in GaAs at low-energies.**

In Figure 4, the polar optical absorption in GaAs is plotted for energies less than 0.25 eV as a function of the integration grid resolution. The rate was calculated with a fixed energy delta of  $E_D = 0.5$  meV. The convergence in the low-energy regime for the non-polar optical scattering rate is shown similarly in Figure 5. In both figures, it is clear that a sufficiently fine grid resolution is necessary to obtain reasonable numerical phonon scattering rates.

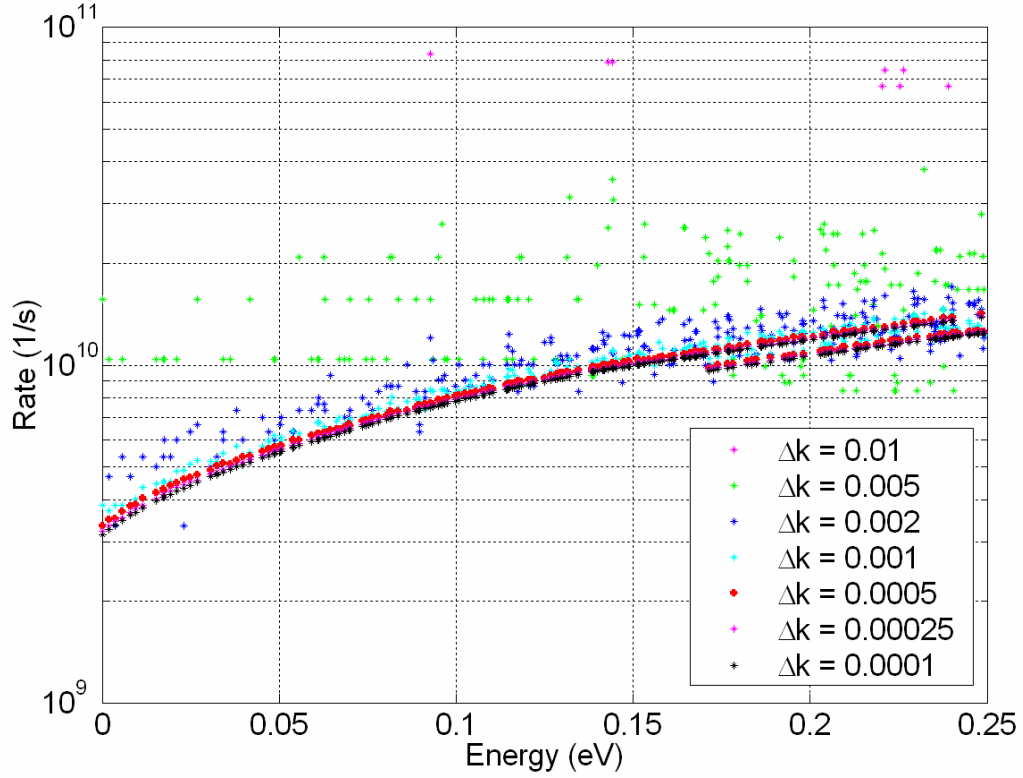


**Figure 5: Non-polar optical absorption in GaAs at low-energies.**

From inspection of the figures, it is reasonable to state that a minimum acceptable integration grid resolution would be  $\Delta k = 0.001$ , while the finest grid resolution used in these examples was  $\Delta k = 0.0001$ . While it is preferable that the grid resolution be as fine as possible, it is not computationally practical.

The electronic band structure used in the Monte Carlo simulator is calculated at discrete  $k$ -points on a grid of resolution  $\Delta k = 0.02$  in and around the irreducible wedge. There are 14,560 grid points for the band structure per band. With four conduction bands there are effectively 58,240 integration grid points. Each time the integration grid resolution is halved, in other words  $\Delta k' = 0.5\Delta k$ , the effective number of grid points increases roughly eightfold. Therefore, a grid resolution of  $\Delta k = 0.01$  would contain

approximately 465,920 total grid points. The finest grid resolution used in the examples above, with  $\Delta k = 0.0001$ , is 100 times finer than the 465,920 grid points with resolution  $\Delta k = 0.01$ . The result would be an integration grid database with roughly 175 trillion points.

This number of integration points is too large to be used for calculations in a reasonable amount of time. Each grid point consists of the vector coordinates ( $k_x$ ,  $k_y$ ,  $k_z$ ), the energy at that point, and the band number. Assuming the coordinates and the energy are stored as a “float,” and the band is an “integer,” each point would then require 16 bytes of memory. The entire integration grid would require in excess of 780 GB. This would exceed the memory capacity of the available computational facilities. In addition, the integration grid is not the only large database item that must be stored in memory, such as the wave function database.

## 2.4 Scattering Rate Calculation Parameters

The scattering rates in this work have been calculated with an integration grid resolution of  $\Delta k = 0.0005$  and an energy delta,  $E_D = 0.5$  meV. At an integration grid spacing of  $\Delta k = 0.0005$ , there are about 2.7 billion integration grid points. Storing the entire grid would require nearly 45 GB. This is still in excess of available memory capacities, so another technique is employed [91].

Instead of storing the entire integration grid in memory, the grid is sliced into segments of roughly 30 million points. Each 30-million-point slice is generated and sorted by energy. This list is used with the desired initial query points, at which the rate is sought. This process is repeated, once for each slice generated, until the entire



irreducible wedge is covered. These parameters allow the scattering rates to be calculated with acceptable accuracy and within an acceptable amount of time [91].

Before each calculation of the scattering rates, a soft limit is placed on the number of grid points in each slice of the irreducible wedge. Generally, this limit is set to 30 millions points. The position of  $\mathbf{k}_y$  is monitored closely; after each complete mini-slice of the irreducible wedge is generated, the  $\mathbf{k}_y$  indicator is updated and the number of points generated to that point is compared to the soft limit.

Consideration must now be paid to the appropriate choice of the query points, the points at which the rate will be calculated. Since the bulk and device Monte Carlo simulators use energy-averaged scattering rates, some latitude is afforded in choosing the query points. Points can be chosen so as to obtain high accuracy where necessary, while fewer query points can be used in energy regimes that do not require the same degree of accuracy.

Since GaAs and GaN-ZB both have a direct band gap, the low-energy regime in the conduction band is centered on the  $\Gamma$ -symmetry point. In contrast, the low-energy regime in 3C-SiC is centered on the X-symmetry point. A large number of points are required in the low-energy regimes where there is a considerable amount of detail that must be captured.

At higher energies, however, the mitigating factor in whether or not a particle scatters via a particular scattering mechanism during a simulation lies in the relative magnitudes of the individual scattering rates with respect to each other. As a result, it is possible to use a coarser coverage of query points at higher energies.

Since the acoustic phonon scattering rate uses a non-constant phonon energy value, the calculation of the acoustic rate requires roughly 50 times more computational time. Therefore, far fewer query points can be used in the calculation of the acoustic phonon scattering rate. The query points for the polar optical and non-polar optical

scattering rates are generally the same. The appropriate choice of query points for the calculation of the acoustic scattering rate, then, is even more critical in obtaining the correct scattering rates in a reasonable amount of time.

## CHAPTER III

### 3.1 Choice of Query Points

The time constraint imposed by the limit of the available computational power requires that the minimum number of query points that will provide an accurate and complete picture of the phonon scattering rates must be found. Redundant query points are those points with energies very similar to other query points. While contributing to the completeness of the results, these points may be eliminated to obtain the numerical scattering rates in a more reasonable amount of time.

In general, and unless otherwise noted, this section refers to the query points chosen to generate the scattering rates in GaAs. Since GaN-ZB is also a direct band gap material, the choice of query points for all scattering mechanisms is similar. The primary difference is that the high-density points at low energies extend to a higher energy in GaN-ZB than they do in GaAs as a result in differences in the density of states between the materials. The query points used for calculating the scattering rates in 3C-SiC, however, are much different since the conduction band minimum is at the X-symmetry point.

Given that the polar optical and non-polar optical phonon energies are constant, the entire process of calculating the scattering rates is accelerated by an algorithm technique such as *QuickSort*. The calculation of the scattering rate is primarily a function of identifying a block of the energy-sorted integration grid slice, currently stored in memory that satisfies the energy conservation requirements, and doing some calculations with those points. As a result of the constant phonon-energy approximation, the addition of another query point does not significantly increase the total computation time. Therefore, more query points can be used than in the calculation of the acoustic phonon scattering rate.

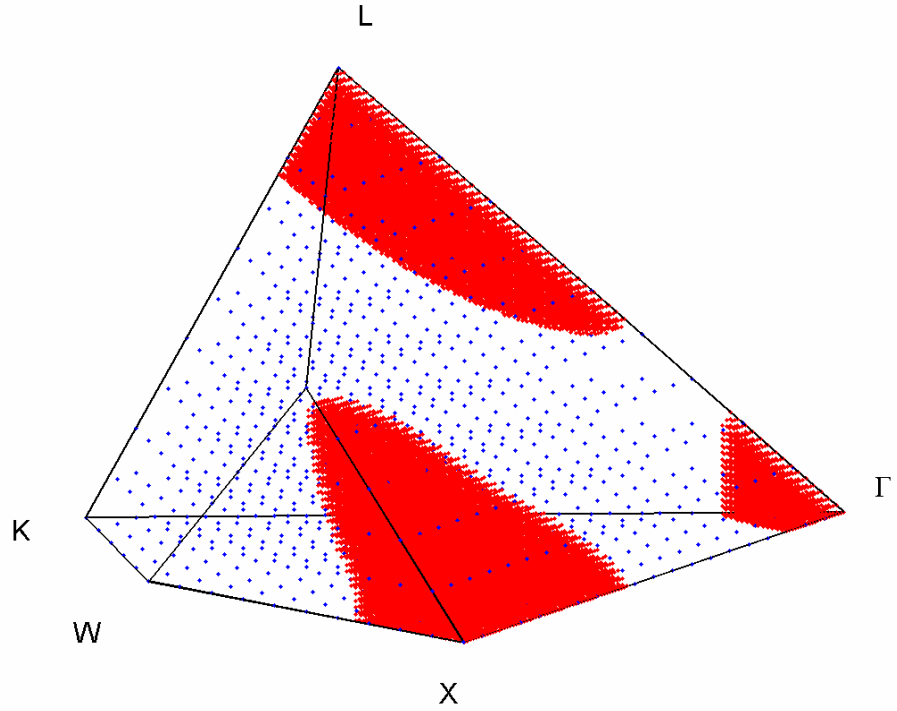


**Figure 6: Query points used in the calculation of electron-phonon optical scattering rates in GaAs [91].**

The one consideration that is necessary, particularly for the polar optical phonon scattering rate, however, is the detail of the scattering rate at very low energies. The polar optical scattering rate, both absorption and emission, has a very distinct shape at low energy. Also, at these very low energies ( $E_k \leq E_g$ ), polar optical scattering is the dominant scattering mechanism. Therefore, the accuracy of its representation in the Monte Carlo simulator is critical. The query points up to energies comparable to the band gap are very densely packed. Outside of this energy range, the points are spread much more coarsely within the remainder of the irreducible wedge. The coverage of the query points in the irreducible wedge for GaAs is shown in Figure 6.

Inspection of Figure 6 reveals the details of the chosen query points. In particular, there are multiple levels of density in the query points. The low-energy regimes in GaAs are centered on the X-, L-, and  $\Gamma$ -symmetry points. These points are red in Figure 6. The rest of the irreducible wedge is sparsely covered by the blue points. The red, low-energy points are almost entirely in the lowest conduction band, while the blue points have quadruple degeneracy for the four conduction bands.

In 3C-SiC the coverage is quite different, and is illustrated in Figure 7.

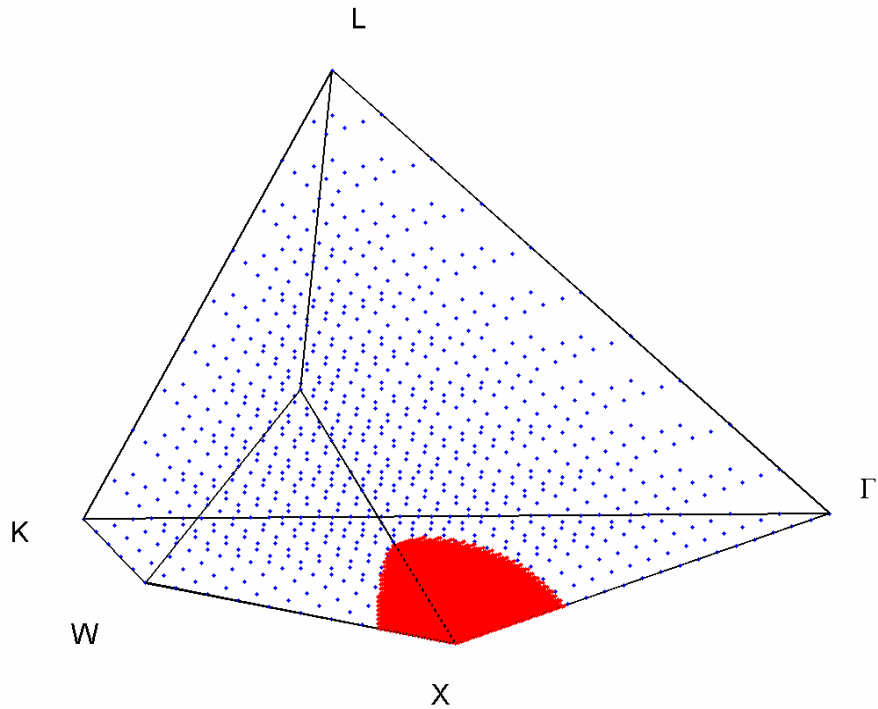


**Figure 7: Electron query points for optical scattering rates in 3C-SiC.**

In Figure 6 and Figure 7, the tightly packed points at very low energies (red points) are spaced at 0.005 in normalized  $k$ -space and usually lie in the lowest conduction band. The tightly packed points are selected up to an energy that sufficiently captures the turn-on detail of the particular scattering rate. The sparsely spaced query

points are spaced 0.02 in  $k$ -space in the lowest conduction band and 0.05 in the higher conduction bands.

If the tightly packed, low-energy query points were chosen at 0.02 spacing, which would correspond to the spacing of the band structure mesh, nearly all of the turn-on of the emission mechanism would be omitted. For example, in a mesh of 0.02 in GaAs, the first three points in the irreducible wedge would be (0.00, 0.00, 0.00), (0.00, 0.02, 0.00), and (0.02, 0.02, 0.00).

The energy at the first point is 0.000 eV, corresponding to the minimum of the conduction band. The polar optical emission rate is obviously zero here. The energy at the second point is 0.0305 eV, still less than the required threshold energy. The energy at the third point is 0.0592 eV. At this point, the rate is nearly completely on; all of the detail in the turn-on is lost. The turn-on occurs very sharply within a very small energy range above the threshold energy.

The computational difficulty in integrating the acoustic phonon scattering rate has been briefly introduced. The use of a  $q$ -dependent phonon energy in the equation results in very time consuming computations for each query point. Since the algorithm has already been optimized for speed, the only method available to get the acoustic phonon scattering rate calculated is to reduce the number of query points.

The risk exists, however, that needed information may be eliminated. One of the benefits of studying the cubic semiconductors is the degree of isotropy in the scattering rates for a given scattering mechanism. The acoustic scattering rate is highly energy dependent, with much weaker wave vector dependence. As a result, as long as all possible energies are represented, other  $k$ -points can be disregarded without the concern for loss of information.

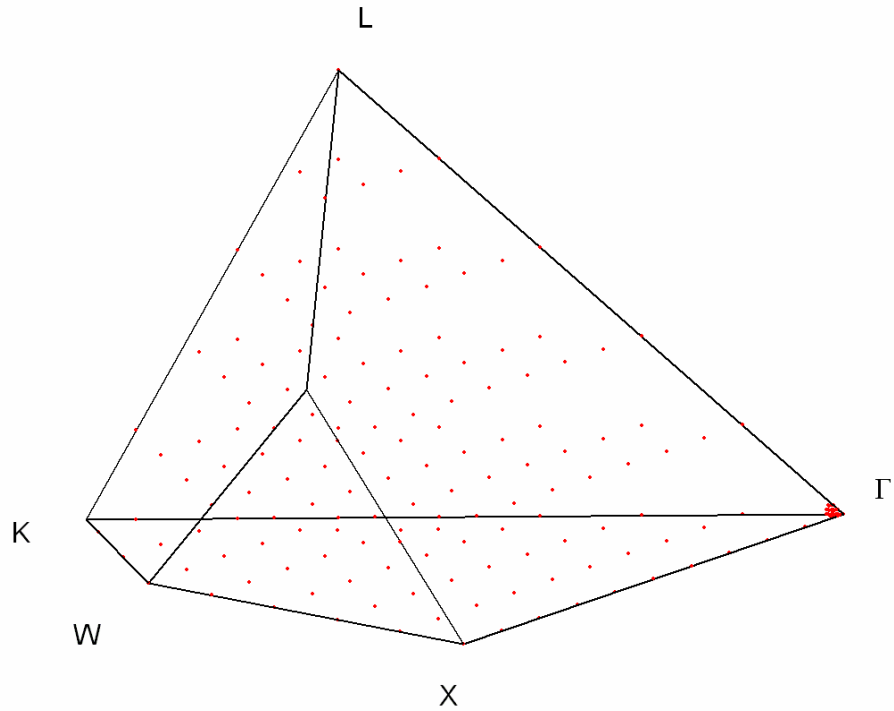


**Figure 8: Query points used in the calculation of electron-phonon acoustic scattering rates in GaAs.**

This claim is verified graphically as well. The acoustic phonon scattering rate will be shown in Figure 10 for GaAs. The graph is quite sparse compared to Figure 9, where nearly 50 times more query points were used. The points used in the acoustic scattering rate calculation produce a rate that is fairly isotropic. It is unclear, however, if the rate appears isotropic because of the sparse number of points or if this is the nature of the acoustic rate.

The one sure approach to answer this question is to produce the acoustic rate at all of the points omitted; however, this was already rejected because the calculation is too time consuming. Therefore, the next possible method of checking the argument made above is to do it in limited regions. The acoustic phonon rate was calculated at an

additional 700 points. However, these points were densely spaced and limited to states with energies only within specific bands. In this case, the energy bands were 1 eV, 2 eV, and 3 eV,  $\pm 0.02$  eV. The grid resolution in normalized  $k$ -space was 0.02.

The results are plotted in Figure 11 for acoustic absorption in GaAs. The results show that the densely packed points (black) bracket the full rate (red) at all three of the energy bands and do not vary wildly. For the case of the 1 eV energy band, it is clear that there is a split in the band. The reason for this is related to the distribution of points at this energy in the lowest two conduction bands. The resulting energy-averaged acoustic phonon rate loses no more  $k$ -dependence than in the other mechanisms, and the energy bands centered on 2 eV and 3 eV show that the acoustic absorption rate is highly isotropic there. The results are similar for the acoustic emission rate.

The number of query points used for the calculation of the optical scattering rates in GaAs is about 39,000. The number of points used for the calculation of the acoustic rate in GaAs is roughly 700. The choice of acoustic phonon query points is illustrated in Figure 8. It is clear that the points are spaced coarsely throughout most of the irreducible wedge, with the densely spaced points at the lowest energies, at  $\Gamma$  in GaAs.

### 3.2 Material Parameters in Calculation of Scattering Rates

The scattering rates incorporate certain physical properties of the materials, outside of the electronic band structure. Usually, these physical values are included in the pre-factor that is outside the summations in the scattering rate equations, except in the case of the acoustic rate. While these parameters are constants, they serve to establish orders of magnitude for the scattering rates.

The physical parameters for GaAs, 3C-SiC, and GaN-ZB are listed in Table 1.



**Table 1: Parameters used in the calculation of the phonon scattering rates for the semiconductor systems discussed in this work.**

Physical Parameter	GaAs	3C-SiC	GaN-ZB
Static Dielectric Constant	12.90	9.72	9.50
High-frequency Dielectric Constant	10.92	6.52	5.35
Energy Gap (300 K) (eV)	1.424	2.20	3.20
Energy Gap (0 K) (eV)	1.519	2.39	3.299
Longitudinal Sound Velocity (m/s)	5240	6440	4570
Lattice Constant (Å)	5.64	4.35	4.50
Density (kg/m <sup>3</sup> )	5360	3166	6095
Optical Deformation Potential Field (eV/m)	$2.10 \times 10^{10}$	$1.30 \times 10^{11}$	$1.00 \times 10^{11}$
LO Phonon Energy (meV)	35.36	120.0	92.0
TO Phonon Energy (meV)	33.29	98.0	92.0
Acoustic Deformation Potential (intra-band)	17	8	12
Acoustic Deformation Potential (inter-band)	11	10	12

### 3.3 Calculation of Scattering Rates

All of the rates presented in this chapter were calculated at a lattice temperature of 300K; however the work presented later in this proposal will require scattering rates calculated at other temperatures. The details of the adjustable lattice temperature, used for the scattering rate calculations and the bulk simulator, will be presented later.

Three features are apparent in the following nine figures. First, in the figures of the acoustic and non-polar optical phonon scattering rates for all three materials, the rates closely follow the shape of the density of states for the given material. This does not come as a complete surprise, since the analytical expressions for these two mechanisms are functions of the density of states. In the case of the analytical acoustic

phonon scattering rate, in the limit of the equipartition approximation [56], the expression is

$$\frac{1}{\tau} = \frac{\sqrt{2m^3} k_B T}{\pi \hbar^4 s^2 \rho} \sqrt{E} \quad (13)$$

The density of states is included in (13), and can be written alone as

$$D(E) = \frac{1}{2\pi^2} \left( \frac{2m}{\hbar^2} \right)^{\frac{3}{2}} \sqrt{E} \quad (14)$$

The second feature of interest in the scattering rate figures is the detail in the very low energy regime of the polar optical phonon scattering rate plots. The first detail is the sharp turn-on of the emission rate; this is particularly clear in Figure 13, the polar optical phonon rate for 3C-SiC. The figure shows the emission rate climbing roughly one and a half orders of magnitude within a very small energy range, beginning just above the optical phonon energy. This is also evident in the plot for GaN-ZB, although the magnitude of the rate does not change as greatly as was shown for 3C-SiC. One additional example of this feature can be observed in the polar optical rate for GaN-ZB in Figure 16. A second turn-on can be found between 1.4 and 1.5 eV, which coincides with the position in the band structure of the secondary X valleys.

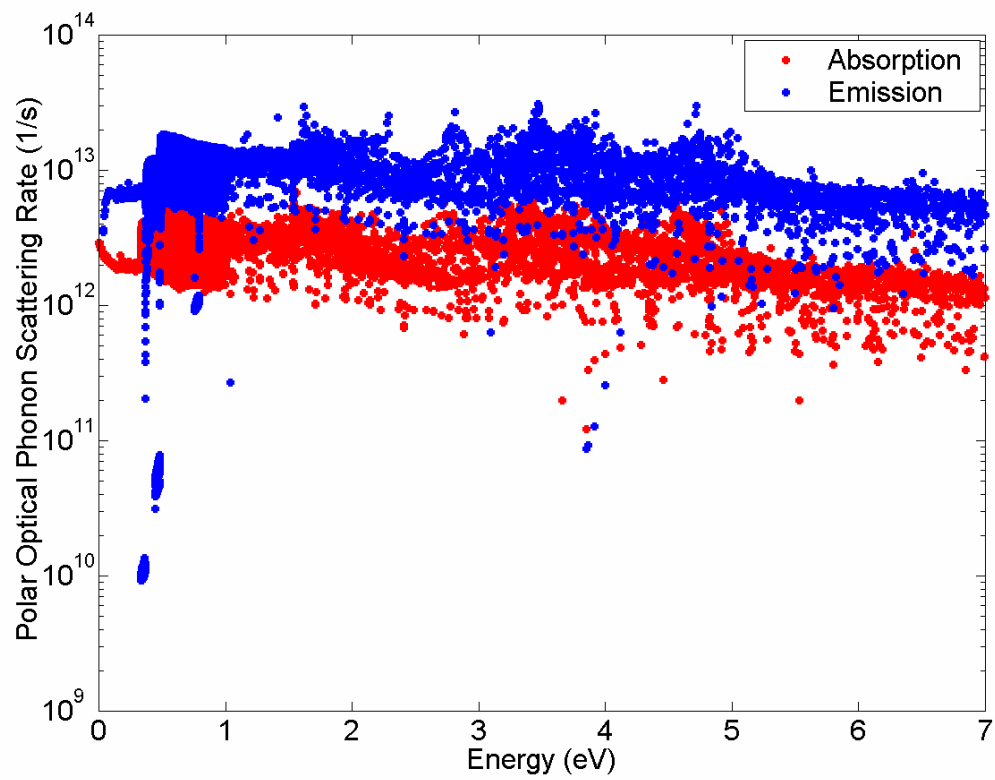


**Figure 9: Polar optical phonon scattering rate in GaAs.**

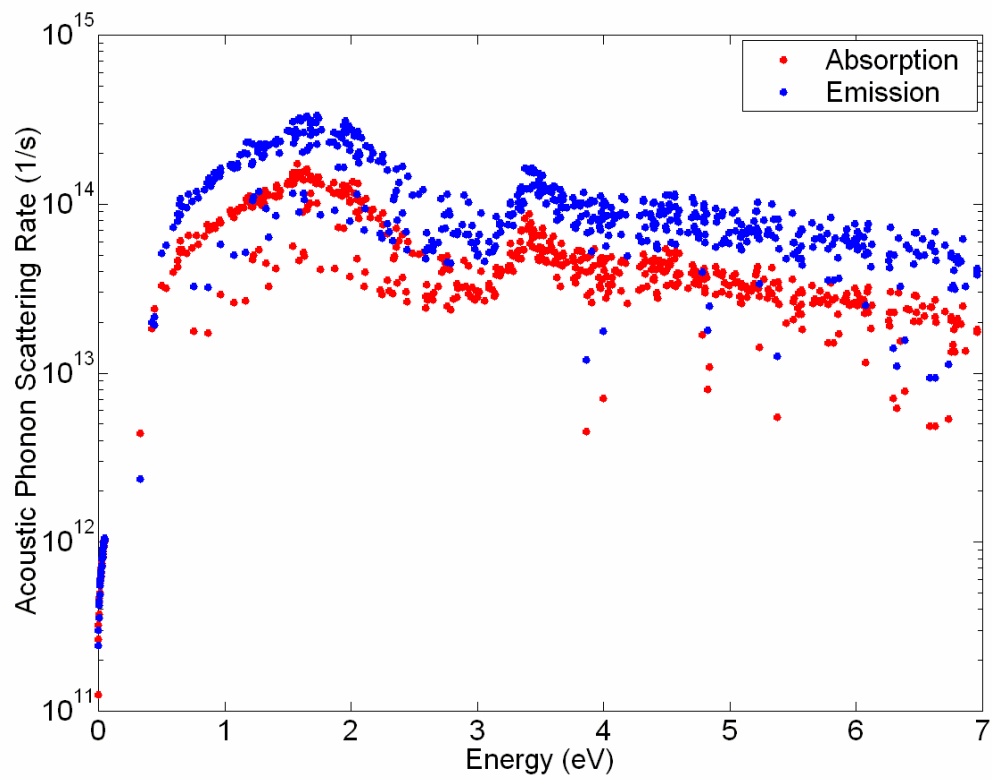


**Figure 10: Acoustic phonon scattering rate in GaAs.**

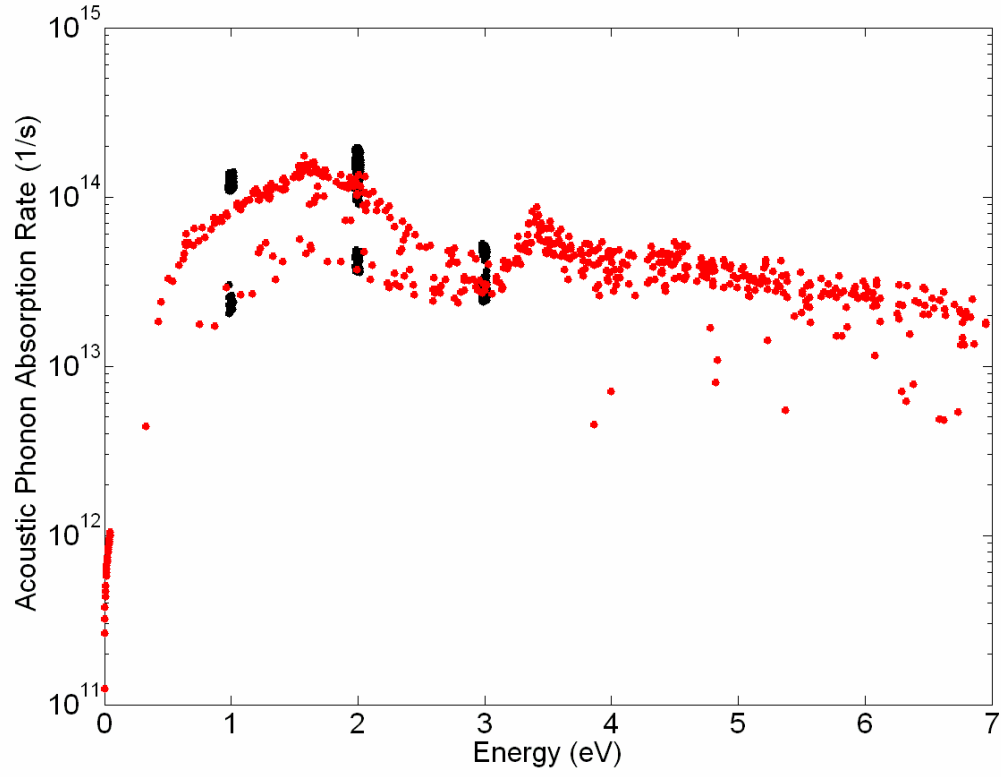


**Figure 11: Acoustic phonon scattering rate (absorption) in GaAs (red). The black points are densely packed and centered at 1 eV, 2 eV, and 3 eV.**

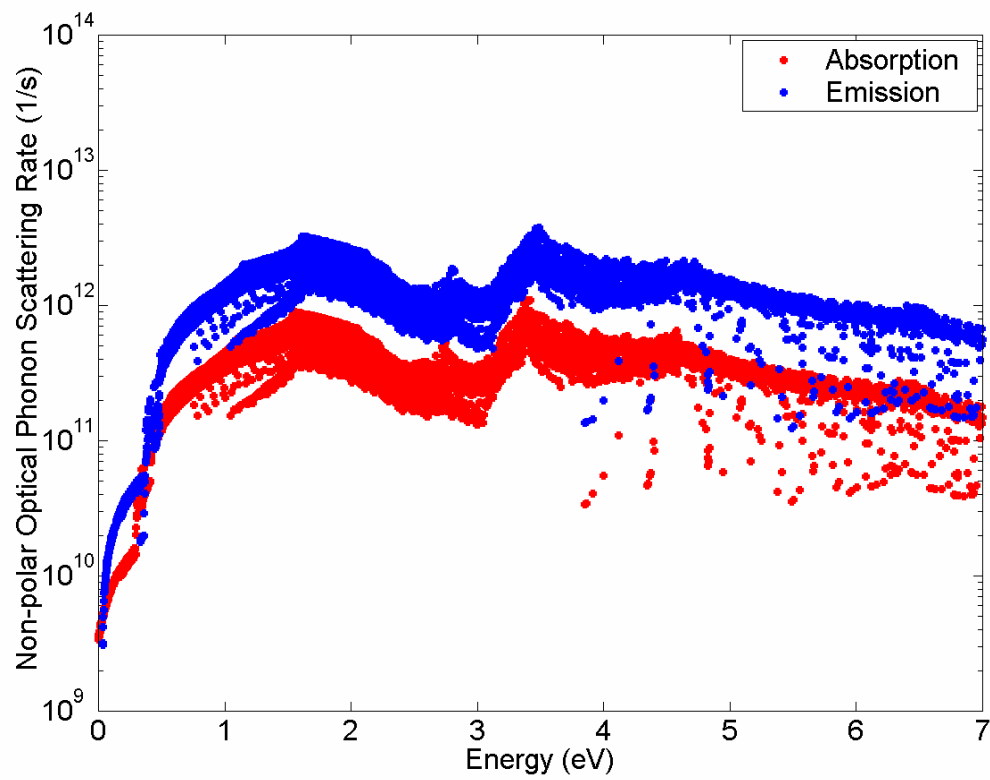


**Figure 12: Non-polar optical phonon scattering rate in GaAs.**

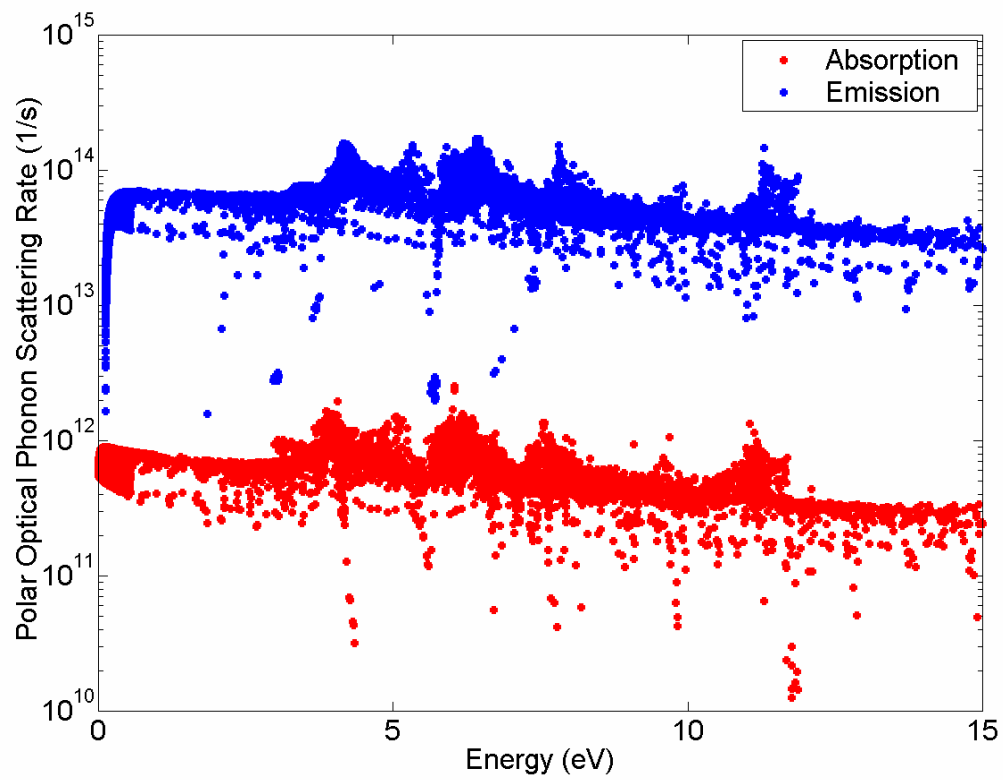


**Figure 13: Polar optical phonon scattering rate in 3C-SiC.**

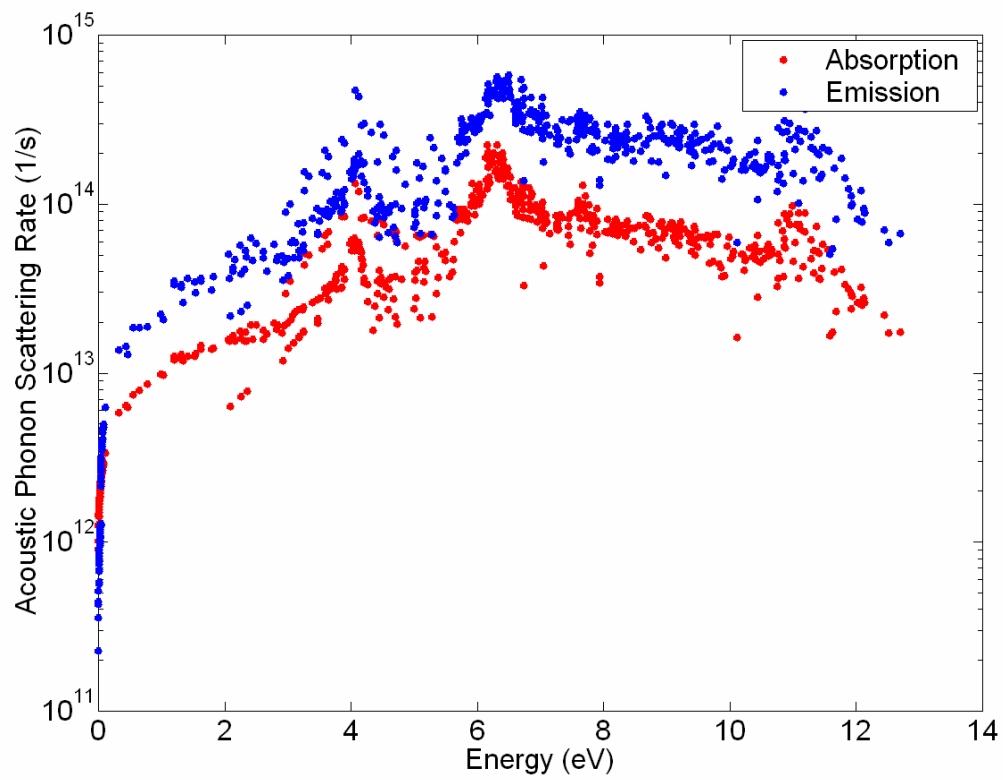


**Figure 14: Acoustic phonon scattering rate in 3C-SiC.**



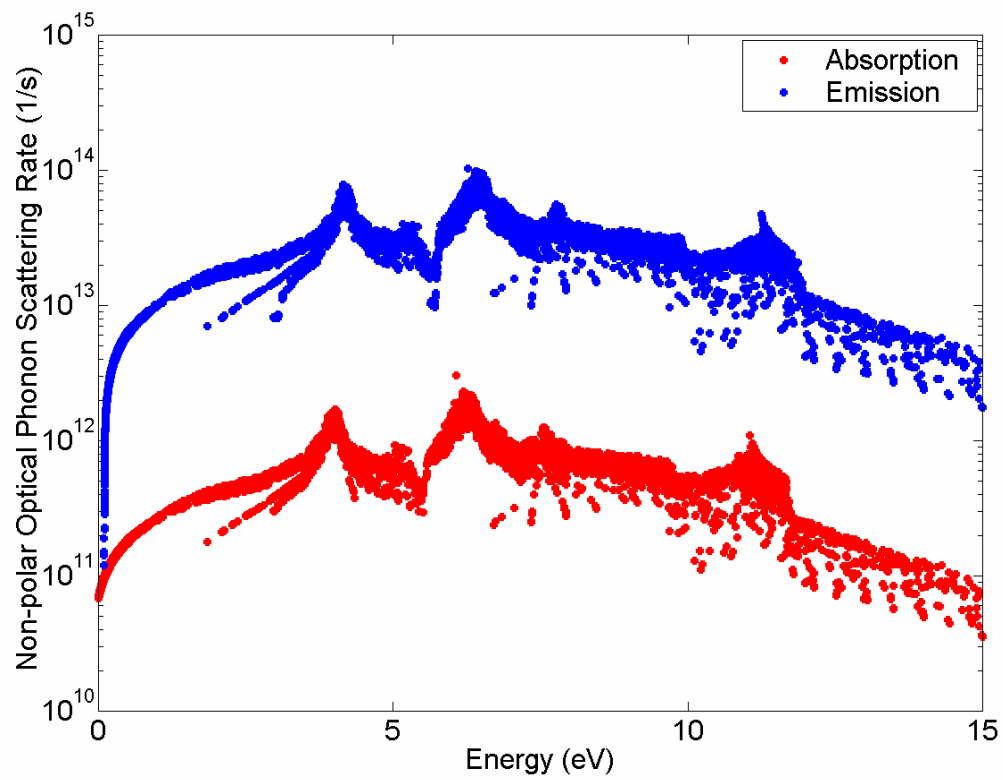
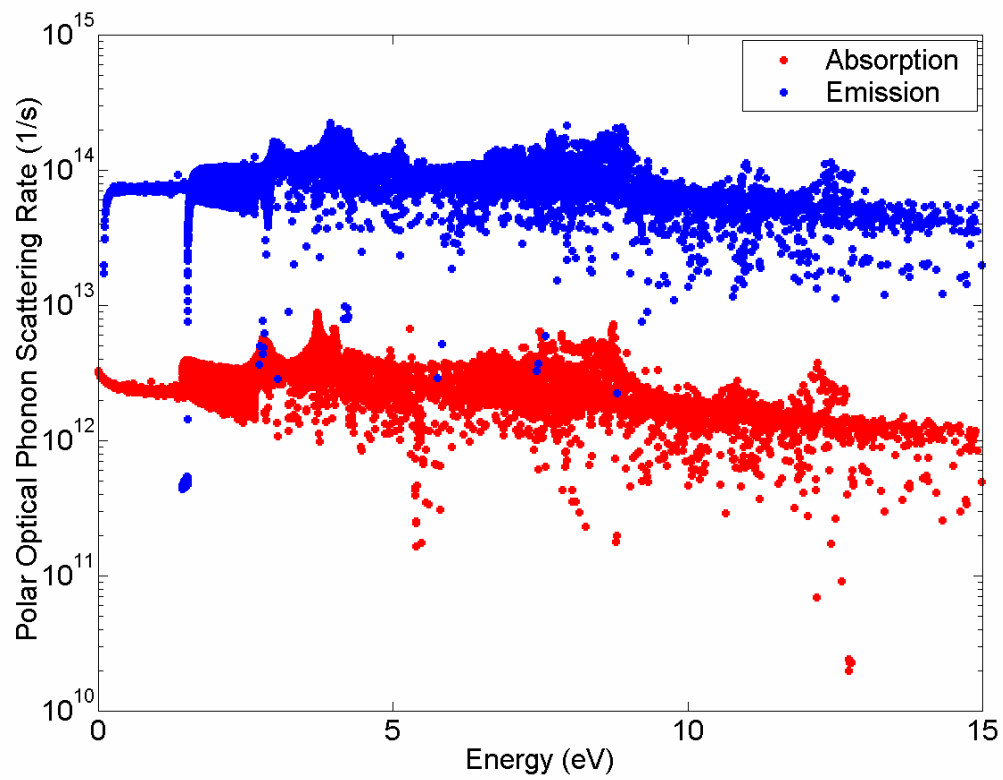
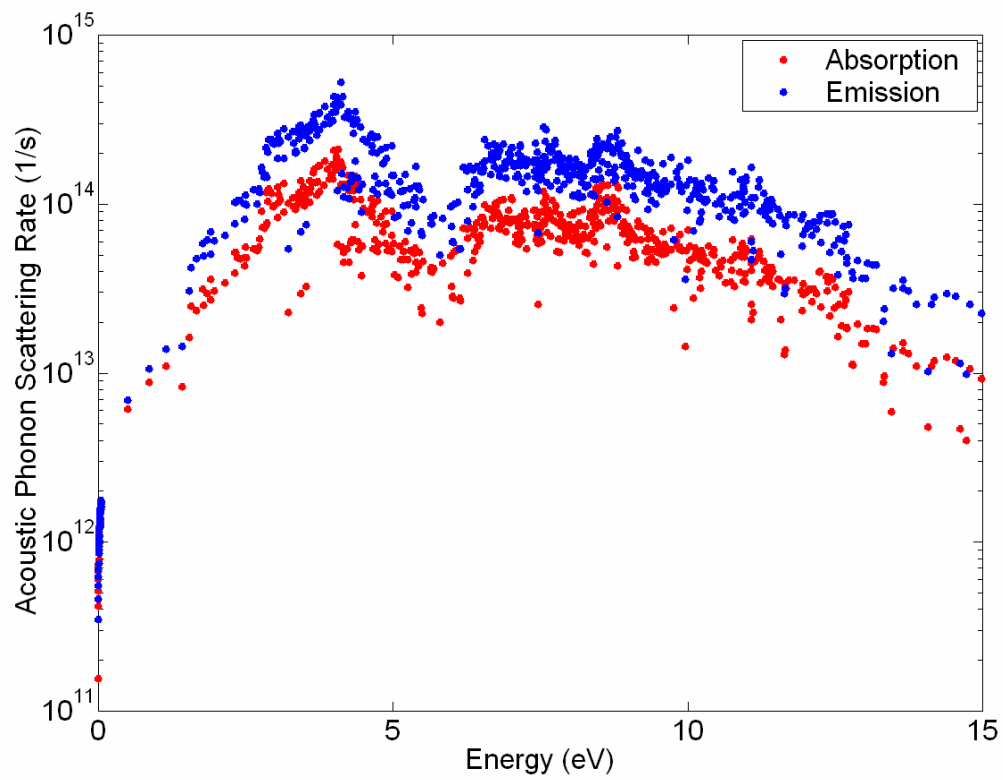


Figure 15: Non-polar optical phonon scattering rate in 3C-SiC.



**Figure 16: Polar optical phonon scattering rate in GaN-ZB.**



**Figure 17: Acoustic phonon scattering rate in GaN-ZB.**

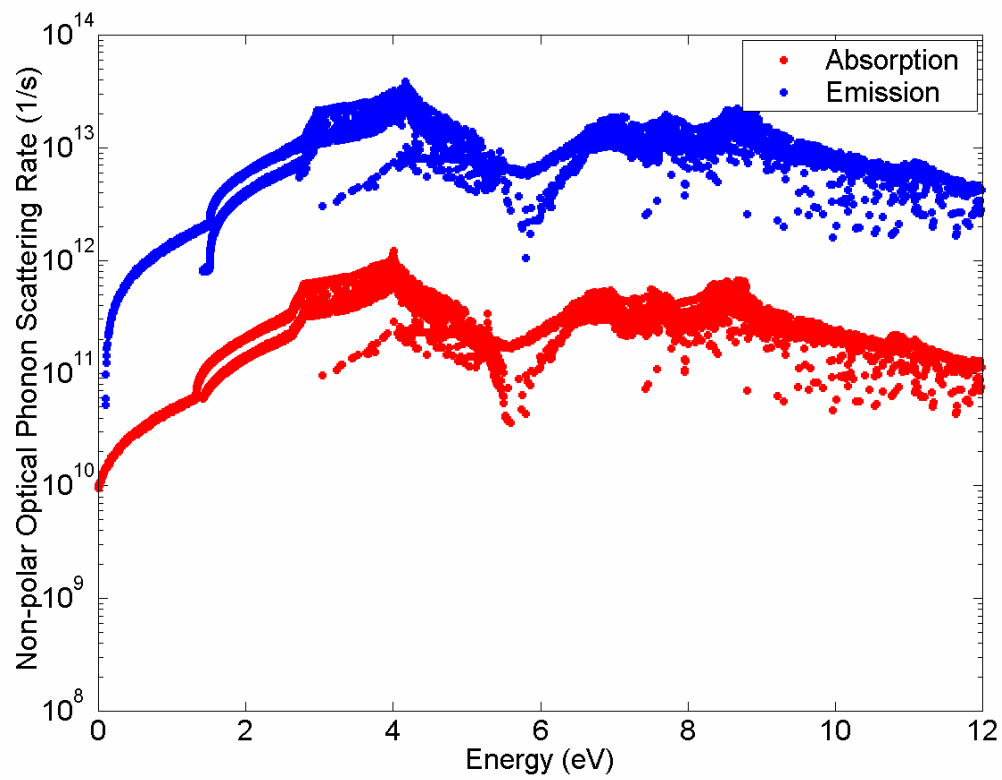


**Figure 18: Non-polar optical phonon scattering rate in GaN-ZB.**

## CHAPTER IV

### 4.1 Impact Ionization

An impact ionization event occurs when a high-energy carrier collides with the semiconductor lattice. During this collision, the initial, high-energy carrier transfers some portion of its kinetic energy to a bound electron. This transfer of energy may be sufficient to liberate the bound carrier, thereby creating a secondary electron-hole pair. The initiating, high-energy carrier may be either a hole or an electron. In order for the initiating carrier to free a bound carrier, the energy of the initiating carrier must be equal to or greater than the band gap.

The study of the transport properties of wide band gap semiconductors under high electric field conditions cannot proceed without an accurate description of the impact ionization process. Impact ionization will limit the maximum operating voltage of some electronic devices because runaway avalanche breakdown may harm the device or alter its performance. In other situations, such as in APDs, impact ionization, and the resulting avalanche breakdown, is the governing mechanism that defines device performance.

Therefore, an accurate model of the impact ionization transition rate within a material is necessary in order to determine reliably the breakdown properties of both materials and devices. Whether the impact ionization event is to be relied on or is to be avoided during device operation, the use of simple, analytical models is unreliable [92]. Instead, an impact ionization transition rate obtained directly from the electronic band structure provides the most complete description possible.

## 4.2 Impact Ionization Transition Rate

The impact ionization transition rate is derived from Fermi's golden rule [i]. The full derivation of the impact ionization transition rate from first principles can be found in Ridley [57]. As obtained by Ridley, the impact ionization transition rate is

$$W_{ii}(n_1, k_1) = \frac{2\pi}{\hbar} \frac{V^3}{(2\pi)^9} \sum_{n_1, n_2, n_2'} \iiint d^3k_2 d^3k_1' d^3k_2' |M_{tot}|^2 \delta(E_f - E_i) \quad (15)$$

The expression of the impact ionization transition rate in (15) is the most commonly found form, as found in Kolnik et al [93]. In this form, the initial states are noted by  $(n_1, \mathbf{k}_1)$  and  $(n_2, \mathbf{k}_2)$ , consistent with the notation of Bude [94], while the final states are primed, i.e.  $(n_1', \mathbf{k}_1')$  and  $(n_2', \mathbf{k}_2')$ .

The term  $|M|^2$  is the squared matrix element [95, 96, 97, 98]. The matrix element contains the details of the overlap integrals and material-specific dielectric screening effects. It is comprised of both the direct,  $M_D$ , and the exchange,  $M_E$ , terms. Although it is not directly evident in (15), it is necessary to include Umklapp processes in the matrix element, and therefore the numerical calculation of the impact ionization transition rate [96]. Umklapp processes refer to transitions that occur via wave vector states outside of the first Brillouin zone. With phonon scattering, momentum is not conserved because the momentum transfer is assumed to be very small [96]. With impact ionization, however, this momentum transfer is frequently large and cannot be ignored [99].

The two-body interaction is described using a statically screened Coulomb potential. The entire process is characterized by the inverse Debye length. The wave

<sup>i</sup> An alternative form of Fermi's golden rule, which is used in this case is:

$W = \frac{2\pi}{\hbar} \left| \langle k | V | s \rangle \right|^2 \delta(E_k - E_s)$ . This form uses a delta function in place of the final density-of-states function. This alternative form is valid over long time durations and applies to single-state transitions [56].

vector-dependent dielectric function is evaluated numerically, again from the pseudopotential band structure, and incorporated into the matrix element of (15). The details of the calculation of the dielectric function are discussed further in Wang et al [100].

### 4.3 Impact Ionization Matrix Element

For simplicity, assume the high-energy, initiating carrier is an electron. The impact ionization is then a two-electron process. Some portion of the energy of the initial, high-energy electron is used to ionize the valence band electron from its atomic bond into the conduction band. The result of the initial, high-energy electron interaction with the lattice is that two conduction band electrons and one valence band hole are produced; one electron is the final state of the initial electron and the second electron is the event-generated electron.

This process can occur for holes, whereby a high-energy hole collides with the lattice resulting in two valence band holes and one conduction band electron. The work in this section will generally refer to electrons, although the equations and the process of calculating the rate are nearly identical. The hole impact ionization rates will be calculated and presented later for the work on APDs. The derivation of the impact ionization transition rate follows that of Bude [94] and will briefly be outlined below.

The electron-electron interaction is designated as  $V_{ee}(\mathbf{r}, \mathbf{r}')$  and is a two-particle interaction with two spatial coordinates. The interaction between two-particle states are written as:

$$|n_1 k_1 \sigma_1; n_2 k_2 \sigma_2\rangle_A \equiv \frac{1}{\sqrt{2}} \left[ \begin{aligned} &\psi_{n_1 k_1}(\vec{r}_1) \psi_{n_2 k_2}(\vec{r}_2) \sigma_1(s_1) \sigma_2(s_2) \\ &- \psi_{n_1 k_1}(\vec{r}_2) \psi_{n_2 k_2}(\vec{r}_1) \sigma_1(s_2) \sigma_2(s_1) \end{aligned} \right] \quad (16)$$

The terms  $s_1$  and  $s_2$  are the spin coordinates and the  $\sigma$  terms are the Pauli spin matrices. The coordinate wave functions,  $\psi$ , are normalized Bloch wave-functions. Via (16), the matrix element of the electron impact ionization event can be written:

$$M(12;34) \equiv \langle n_1 k_1 \sigma_1; n_2 k_2 \sigma_2 | V_{cc} | n_3 k_3 \sigma_3; n_4 k_4 \sigma_4 \rangle \quad (17)$$

The matrix element contains four terms with different arrangements of the coordinates and the wave functions. For simplicity of notation, the product state  $|12\rangle$  is written:

$$|12\rangle = \psi_{n_1 k_1}(\vec{r}_1) \psi_{n_2 k_2}(\vec{r}_2) \quad (18)$$

By (18), (17) becomes:

$$M(12;34) \equiv \frac{1}{2} \left[ \begin{aligned} &\delta_{\sigma_1 \sigma_3} \delta_{\sigma_4 \sigma_2} \langle 34 | V_{cc} | 12 \rangle - \delta_{\sigma_1 \sigma_4} \delta_{\sigma_2 \sigma_3} \langle 43 | V_{cc} | 12 \rangle \\ &- \delta_{\sigma_1 \sigma_4} \delta_{\sigma_2 \sigma_3} \langle 34 | V_{cc} | 21 \rangle + \delta_{\sigma_2 \sigma_4} \delta_{\sigma_1 \sigma_3} \langle 43 | V_{cc} | 21 \rangle \end{aligned} \right] \quad (19)$$

For a given initial spin state  $\sigma_1$ , there are three distinct situations with equal probabilities of occurrence. These situations correspond to the different configurations of the remaining spin indices. The situations are:

1.  $\sigma_1 = \sigma_2 = \sigma_3 = \sigma_4$
2.  $\sigma_1 \neq \sigma_2$ :  $\sigma_1 = \sigma_3$ ,  $\sigma_2 = \sigma_4$
3.  $\sigma_1 \neq \sigma_2$ :  $\sigma_1 = \sigma_4$ ,  $\sigma_2 = \sigma_3$

The rate for each configuration must be calculated separately, as done by Bude, and then summed to give the total rate independent of spin. Bude makes the following definitions:

$$\begin{aligned} M_1 &= \langle 34 | V_{cc} | 12 \rangle \\ M_2 &= \langle 43 | V_{cc} | 12 \rangle \end{aligned} \quad (20)$$



Then, from spin configurations in the list of the three possible situations, the squares of the matrix elements can be written in terms of  $M_1$  and  $M_2$  as:

1.  $|M_1 - M_2|^2$
2.  $|M_1|^2$
3.  $|M_2|^2$

The probabilities are summed to give the total matrix element:

$$M_{tot}^2 = 2|M_1|^2 + 2|M_2|^2 - (M_1^* M_2 + M_2^* M_1) \quad (21)$$

For the details on how (21) was obtained from the different possible spin configurations, see Appendix I.

#### 4.4 Calculation of Impact Ionization Transition Rate

As was the case with the phonon scattering rates, the equation for the impact ionization transition rate is a continuous integral in wave vector space. Whereas the phonon scattering rate equations were integrated over one final state, the impact ionization transition rate is integrated over three other states. Nevertheless, (15) is converted to discrete summations for computational purposes.

With the calculation of the phonon scattering rates, the rate was solved completely for each query point over the final-point grid of 2.7 billion points. Due, however, to the requirements of energy and momentum conservation for the impact ionization transition rate, the rate cannot be obtained via a complete solution to the summations and integrals of (15). Instead of using the grid of final states employed for the phonon rates, the final states for the impact ionization integration are selected

randomly in accordance with Monte Carlo integration techniques. Generally, five million final states are examined for each initial state.

For purposes of numerical evaluation, the delta functions are replaced by rectangles with height  $\delta E^{-1}$ , and width  $\delta E$ . A constant value of 5 meV has been chosen for  $\delta E$ . This broadening factor should be physically related to intra-collisional field and collision broadening effects; however these effects have been neglected explicitly here, as is usually done. Recent work [101] has shown that energy broadening effects the impact ionization transition rate only near the threshold energy and has little effect at higher energies where most ionization events occur.

The impact ionization transition rate is calculated for a three dimensional grid covering the irreducible wedge of the first Brillouin zone. The grid spacing of initial states is 0.05 in normalized  $\mathbf{k}$ -space, and yields a total of 916 points per band. The electron-initiated impact ionization transition rate is calculated for query points in all four conduction bands; the results are plotted in the figures at the end of this chapter. It can be seen that the 3664 query points provide thorough coverage across the entire energy ranges of interest. Even with the relative speed of the Monte Carlo integration technique, the computation of the impact ionization transition rate can take at least three days for the 3664 points.

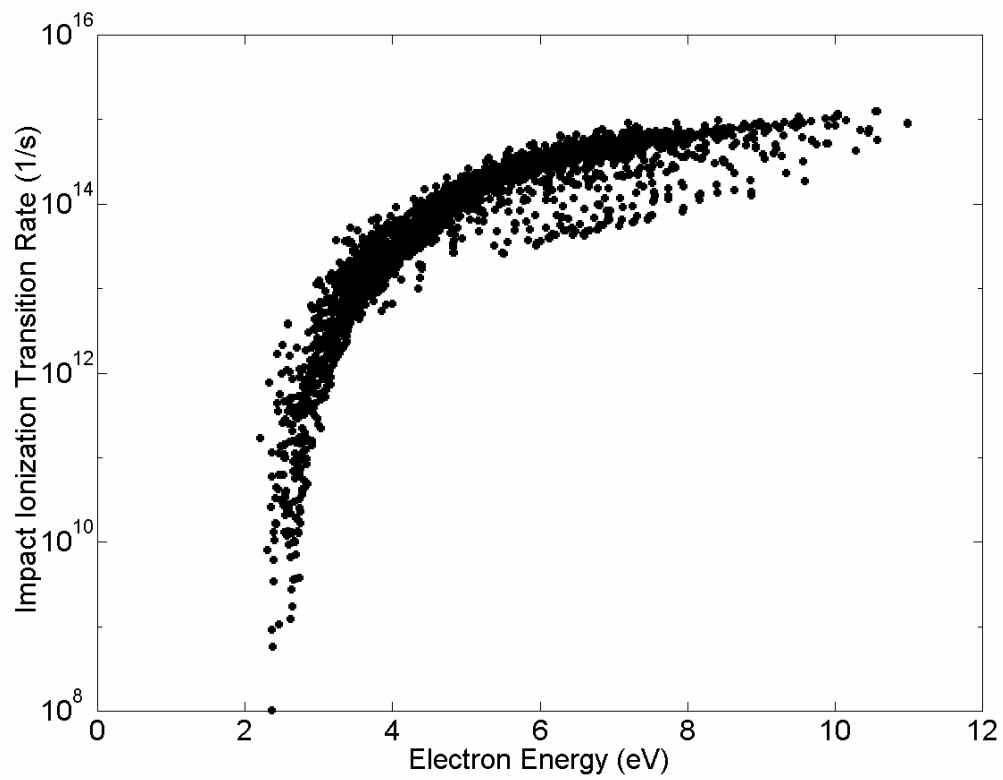


**Figure 19: Impact ionization transition rate for GaAs**

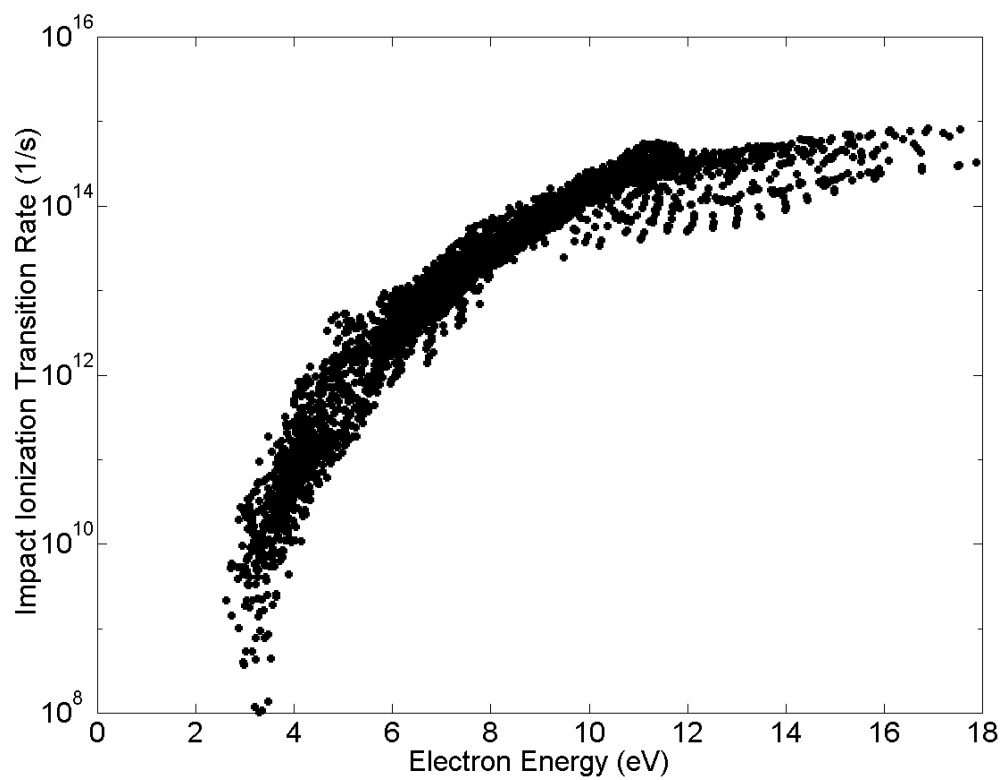


**Figure 20: Impact ionization transition rate for 3C-SiC**

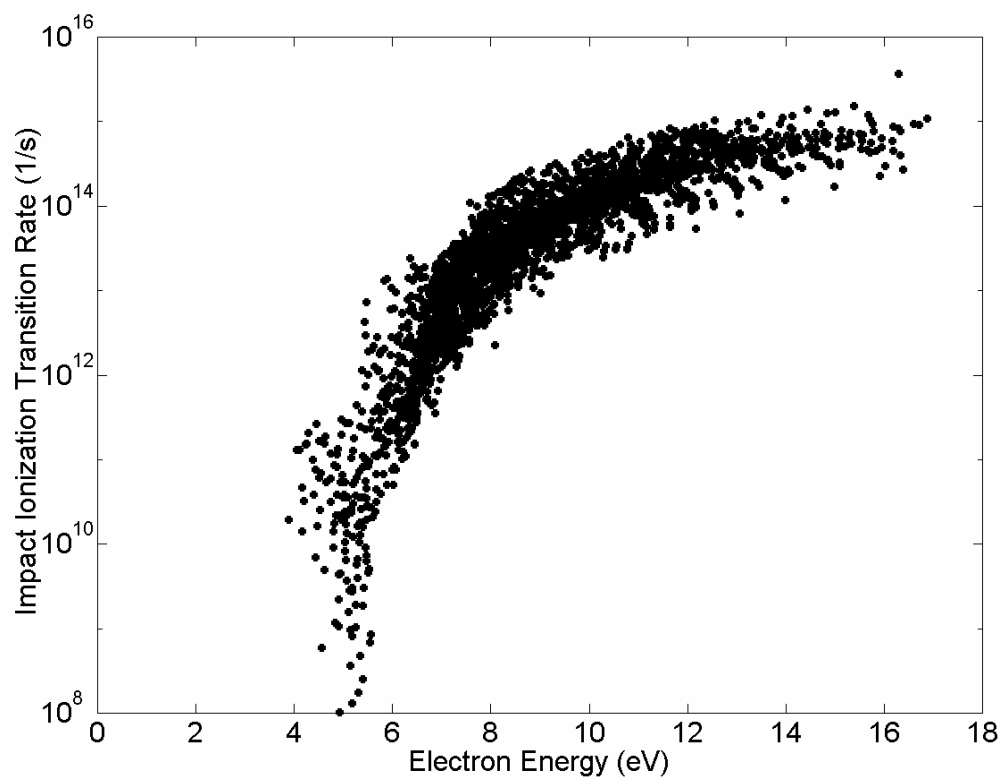


**Figure 21: Impact ionization transition rate for GaN-ZB**

# CHAPTER V

## 5.1 Monte Carlo Simulator

To describe broadly the Monte Carlo bulk simulator, it could be stated that the simulator consists of two basic mechanisms: drifting and scattering. Each particle simulated drifts due to the applied electric field, and if a carrier-phonon interaction occurs, the particle is scattered. Statistics are collected along the way.

Each carrier is stored in memory with its wave vector, band index, and energy. Under a given applied electric field, for a given ballistic time-step, the particle drifts, according to Newton's Laws of motion, by updating the wave vector,  $\mathbf{k}$ , by some amount,  $d\mathbf{k}$ , where:

$$d\vec{k} = -\frac{e}{\hbar} F(\vec{r}) dt \quad (22)$$

The carrier charge,  $e$ , carries the sign of the associated carrier type [102]. After the new wave vector is obtained, the carrier energy is updated via a quadratic interpolation scheme described by Fischetti [24, 102]. Following carrier value updates, global statistics such as average energy change per drift can be updated before moving to the second phase of the transport process. After a given particle drifts and its kinetic energy is updated, a random number [ii] is generated to determine if a carrier will scatter, based on the total scattering rate at the carrier energy.

In the trivial case, no scattering event occurs, in which case the simulator considers the next carrier. However, if it is determined that a carrier will scatter, another

<sup>ii</sup> A note on random numbers is made. Most random number generators included as base features of most operating systems are not sufficient. The Monte Carlo simulator requires a random number generator that has an even distribution function, and that is not necessarily true of standard random number generators. For that reason, many algorithms can be found, such as in *Numerical Recipes*, where the distribution function is even. Other algorithms are optimized for

random number is generated to determine the particular scattering mechanism (polar-optical, acoustic, etc.) This is accomplished by comparing the value of the random number to the relative strengths of the individual scattering mechanisms at the carrier energy. For the case of the phonon scattering events, each mechanism consists of two possibilities, absorption and emission.

Once a scattering mechanism is chosen, it is then necessary to determine the carrier's final state. Based on the type of mechanism, and whether the process is one of absorption or emission, the final carrier energy is known, since the phonon energies are assumed constant. The unknown, however, is the new carrier wave vector. The determination of the new carrier wave vector is the primary role of final state selection algorithms. The final state selection employed in the Monte Carlo simulator is similar to, and based on, the work by Fischetti and Laux [22].

Given an initial carrier with initial state  $(\mathbf{k}, E)$ , its final energy,  $E'$ , is known. The mesh in the irreducible wedge is searched for all momentum states with energy  $E'$ . The resulting list of possible final states is stored and weighted by the squared overlap integral and the squared matrix element. The squared matrix element is dependent on the particular scattering mechanism. The final state is chosen randomly from this list of weighted possible final states.

After the scattering process is complete, the simulation statistics are again updated. The drift/scatter process repeats for the pre-determined simulation time, generally between two and five picoseconds for bulk simulations, but may be much longer for certain device simulations.

speed, as well. This is particularly valuable in Monte Carlo simulations given the frequency with which random numbers are required.

## 5.2 Inputs: Band Structure and Pseudo Wave-Functions

The band structure is calculated for a mesh in the irreducible wedge at a grid spacing of 0.02 in normalized  $\mathbf{k}$ -space. The grid is extended slightly outside of the defined edge of the zone in order to implement the quadratic energy interpolation for points near the zone edge. Unpublished work required for this thesis showed that the use of a 0.02 band structure resulted in interpolation errors of less than 0.1%, even near the band edge in GaAs; moving to a band structure spacing of 0.01 did not provide sufficient error minimization to justify the roughly 8-fold increase in the number of mesh points. The 0.02 grid was particularly successful, especially compared to the results of the 0.05 grid reported by Laux and Fischetti in their work with Si [102].

For reference, any  $\mathbf{k}$ -point that satisfies the following conditions is in the irreducible wedge of a zincblende material [96]:

1.  $0 \leq k_x + k_y + k_z \leq 1.5 \left( \frac{2\pi}{a} \right)$
2.  $0 \leq k_z \leq k_x \leq k_y \leq \frac{2\pi}{a}$

Therefore, the irreducible wedge of a zincblende crystal, including additional edge points for interpolation purposes, requires 14,560 total grid points. Also, each of the 14,560 grid points has a degeneracy of eight, as each point is used for four conduction and four valence bands. For each point, in each band, several pieces of information are stored, including the energy at the point, along with nine additional values related to the first and second derivatives. The derivatives are required by the quadratic interpolation; three values correspond to  $dE/dk_x$ ,  $dE/dk_y$ , and  $dE/dk_z$ . The next six values correspond to the second derivatives, namely,  $d^2E/d^2k_x$ ,  $d^2E/d^2k_y$ ,  $d^2E/d^2k_z$ ,  $d^2E/dk_xdk_y$ ,  $d^2E/dk_xdk_z$ , and  $d^2E/dk_ydk_z$ .



### 5.3 Acoustic Deformation Potentials

While most of the coupling constants used in the Monte Carlo simulator are generally agreed upon values, such as the polar optical phonon energy, some may be difficult, at best, to obtain. Much of the uncertainty arises quite simply from lack of detailed experimental information. Either it is premature to find reliable experimental results for a novel semiconductor system, or the values are difficult to obtain. In other cases, some uncertainty exists due to a considerable spread in measured values [32].

The acoustic deformation potential acts as the only user-adjustable parameter in the Monte Carlo simulator. It can, in effect, act to correct small errors in the band structure by modifying the carrier transport dynamics. The value of the acoustic deformation potential is selected such that the calculated transport quantities are in good agreement with experimental results, when applicable [58].

The ideal end result is to have a Monte Carlo bulk and device simulator that is reliant primarily only on the electronic band structure. For this reason, then, any deficiencies in the energy-momentum dispersion relation will be exposed as inaccurate bulk and device performance results. While the development of the bulk and device simulators has been successful, the results are only as reliable as the available band structure.

Small discrepancies in the band structure give way to transport errors. For this reason, a tunable acoustic deformation potential is used. The acoustic deformation potential can be adjusted in such a way that the transport properties reported by the simulator match experimental results. In the absence of experimental results, the simulator can predict a range of probable transport parameters.

In accordance with the standard paradigm [103], the acoustic deformation potential is chosen to be isotropic and hence has no wave vector dependence itself.

This is a reasonably valid, and more importantly, general assumption. It is found that the deformation potential does, however, need to be energy dependent, in order to simultaneously satisfy the results for the velocity-field, average energy-field and impact ionization coefficients. This is consistent with the earlier work of Fischetti and Laux [103], where two values of the deformation potential have been chosen. It is possible that the deformation potential has multiple values or may vary continuously with energy, but the choice of only two values yields the simplest and most general picture, while introducing the lowest degree of parameterization.

Given that the deformation potential is to have at least two values, the transition point in energy separating the two ranges of the deformation potential must be established. In order to avoid an additional arbitrary parameter, one deformation potential is chosen to apply to intra-band transitions, transitions within the first conduction band (or first valence band in the case of holes.) The other deformation potential is associated with inter-band transitions, transitions between carriers in any other combination of bands. Thus, the energy range for which each deformation potential value is used is naturally established by the band structure of the material.

For GaAs, for instance, there is ample experimental transport data available, so for convenience the simulator calculations are compared to accepted results for the velocity vs. field, energy vs. field, and impact ionization coefficients. It is important to note that other sets of experimental measurements, such as mobility, saturation velocity, etc. may be used to determine the acoustic deformation potentials.

The first step is to calculate the impact ionization coefficient at a fixed field for various pairs of deformation potentials. The logarithm of the calculated impact ionization coefficient as a function of the intra-band and inter-band deformation potentials at an electric field strength of  $350 \text{ kV/cm}$  is shown in Figure 22. The intersecting plane in the

figure corresponds to the generally accepted value of the impact ionization coefficient at that field.

There are several pairs of deformation potentials that produce an ionization coefficient that is consistent with the experimental value. Next, the average energy and impact ionization coefficients are plotted as a function of the inter-band deformation potential, with the low deformation potential as a parameter in Figure 23 and Figure 24.

The dashed horizontal line in Figure 23 and Figure 24 corresponds to the accepted value of the impact ionization coefficient and the average particle energy [24] at an applied electric field of  $350 \text{ kV/cm}$ , respectively. Inspection of Figure 23 shows that there are three sets of deformation potential pairs that produce a calculated result in agreement with accepted values. These pairs are (14, 18), (16, 14), and (18, 6) for the intra- and inter-band deformation potentials, respectively. Thorough inspection of Figure 24 shows that the average energy is too high for the (14, 18) pair, while the (16, 14) and (18, 6) pairs bracket the accepted average energy. Thus, the target deformation potential pair lies between these two sets.

The intermediate and approximate average of (17, 11) is chosen for the target deformation potential pair, between the (16, 14) and (18, 6) pairs. It will be shown shortly that there is a fair amount of tolerance of the calculated results to variations in the values of the deformation potential, provided, of course, that they are between bracketing values.

The impact ionization coefficients as a function of inverse field are plotted in Figure 25, along with the range of experimental values [104] and the calculations by Fischetti [24]. As can be seen from the figure, the impact ionization coefficients calculated using the (17, 11) pair lie well within the range of experimental values throughout the full range of applied electric fields.

It is useful to examine the sensitivity of the calculated ionization coefficients to the choice of the deformation potentials. Two different deformation potential pairs, (16, 12) and (18, 10), which bracket the (17, 11) pair are used. As can be seen from Figure 25, in the case of both (16, 12) and (18, 10), the calculated impact ionization coefficients lie within the range of experimental values and again form acceptable pairs. The calculated ionization coefficients are somewhat tolerant of the choice of the deformation potentials.

Figure 26 shows a log-log plot of the calculated average electron energy as a function of applied electric field strength in bulk GaAs. It is readily seen from the figure that the average energy varies little with the choice of the deformation potential pairs over the full range of electric field strengths. The calculations are also in excellent agreement with those of Fischetti [24]. As with the case of the calculated ionization coefficients, the average energy is robust to small fluctuations in the choice of the acoustic deformation potential.

Further understanding can be gleaned from analysis of the low field transport calculations by examining the dependence of the calculated velocity-field curve on the choice of deformation potentials. The calculated velocity-field curve as a function of applied electric field with the deformation potential pairs as a parameter is shown in Figure 27. There is only a slight variation in the velocity with deformation potential changes. If the deformation potential is chosen such that the impact ionization coefficients and average energy are reasonably satisfied, other transport parameters, such as the velocity-field relation, are naturally satisfied as well. The calculated velocity is in good agreement with previous studies [24] and reproduces the salient features of low field transport in bulk GaAs.

This model has been applied to the transport properties of bulk 3C-SiC. The procedure for obtaining the acoustic deformation potentials and the concomitant

macroscopic transport quantities, e.g., average energy, velocity vs. field, impact ionization coefficients, etc., is nearly identical to that used for GaAs.

Again, two energy-dependent acoustic deformation potentials are used, one for intra-band and the other for inter-band scattering transitions. The values of the two deformation potentials obtained by the model, and used in the simulations are (10, 8). The values of the deformation potentials were determined using average energy vs. field and velocity vs. field information in the same manner as was done for GaAs.

The calculated average carrier velocity vs. applied electric field, and impact ionization coefficients are plotted in Figure 28 and Figure 29, respectively. Inspection of Figure 28 shows that the electron drift velocity decreases with increasing field strength beyond  $300 \text{ kV/cm}$ . This result has also been observed by Nilsson [105]. The magnitude of the calculated velocity and impact ionization coefficients is very close to that obtained by Nilsson [105] wherein a different, *ab initio* band structure was used.

Finally, the work was extended to GaN-ZB. Table 2 shows the acoustic deformation potential pairs for all three of the materials used in the remainder of this work.

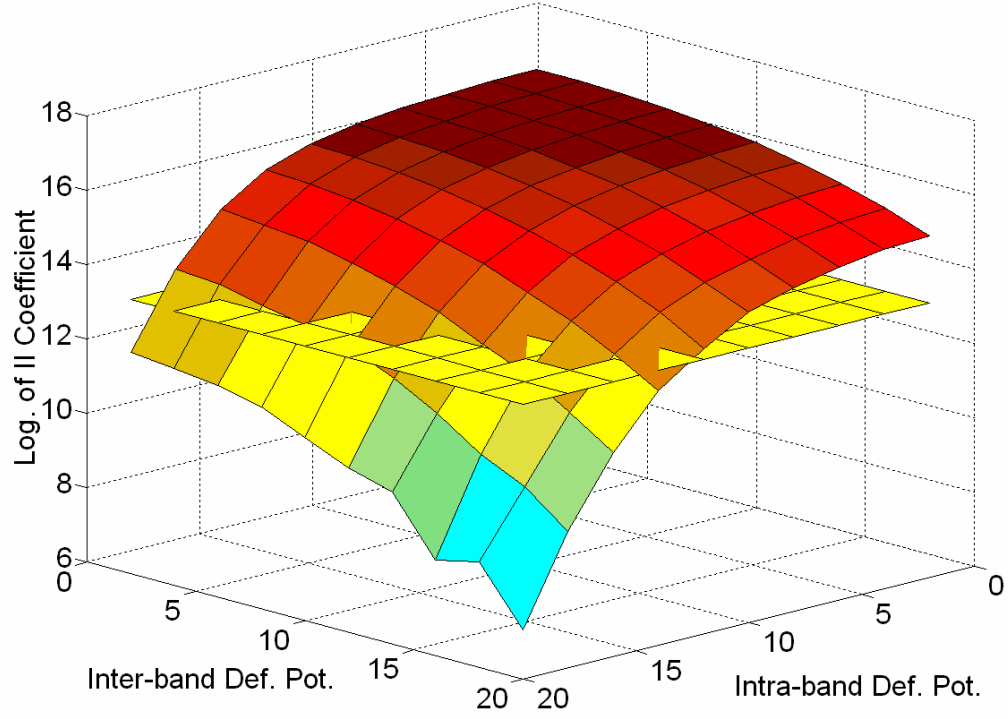


**Figure 22: Logarithm of impact ionization coefficient in GaAs at an applied electric field strength of  $350 \text{ kV/cm}$  as a function of the intra- and inter-band acoustic deformation potentials.**

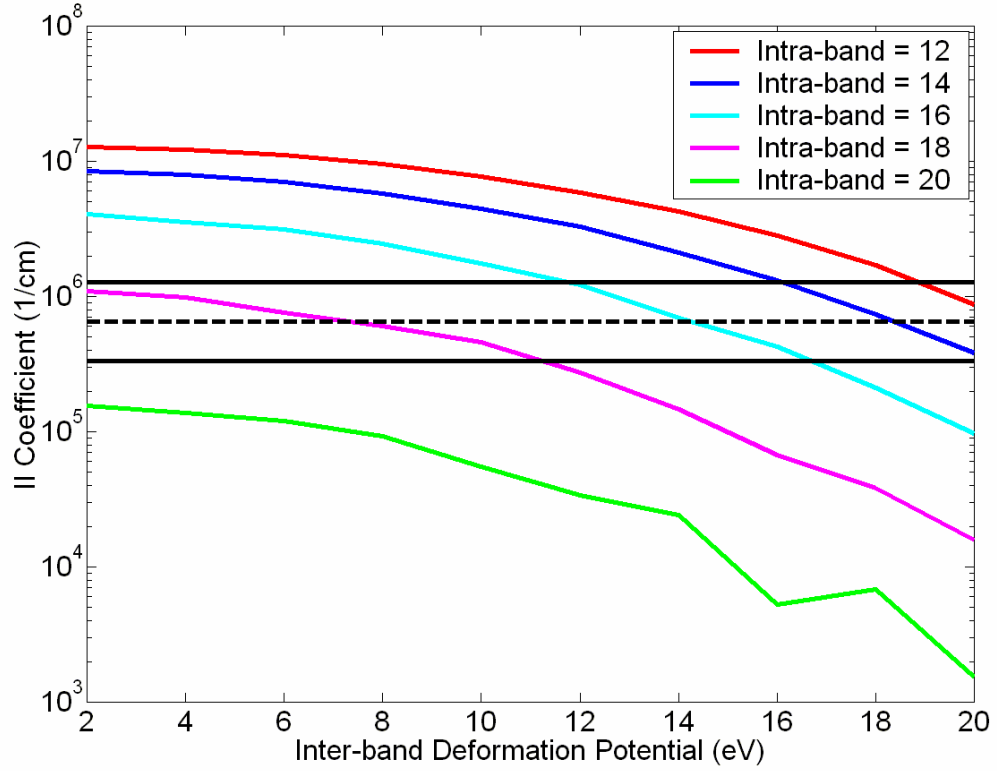


**Figure 23: Impact ionization coefficient in GaAs at an applied electric field strength of  $350 \text{ kV/cm}$  vs. the inter-band acoustic deformation potential as a function of the intra-band acoustic deformation potential. The dashed line represents the generally accepted value of the impact ionization coefficient at the applied field, while the black solid lines above and below represent 10% deviations of the accepted value.**

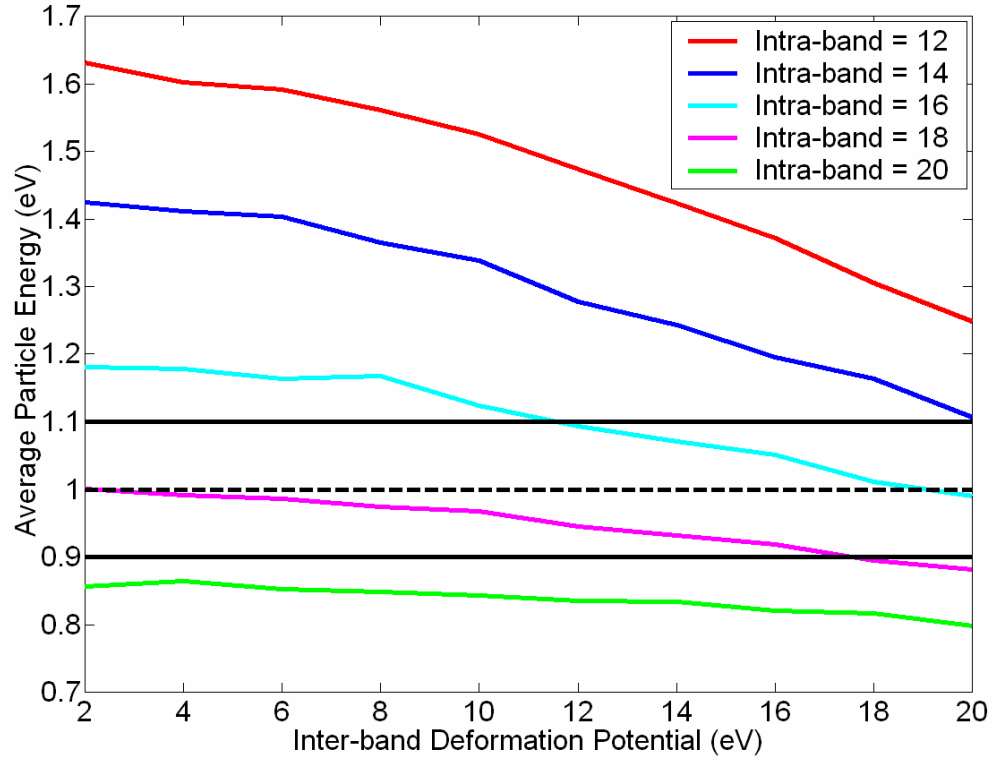


**Figure 24: Average particle energy in GaAs at an applied electric field strength of  $350 \text{ kV/cm}$  vs. the inter-band acoustic deformation potential as a function of the intra-band acoustic deformation potential. The dashed line represents the generally accepted value of the average energy [24] at the applied field, while the black solid lines above and below represent 10% deviations of the accepted value.**



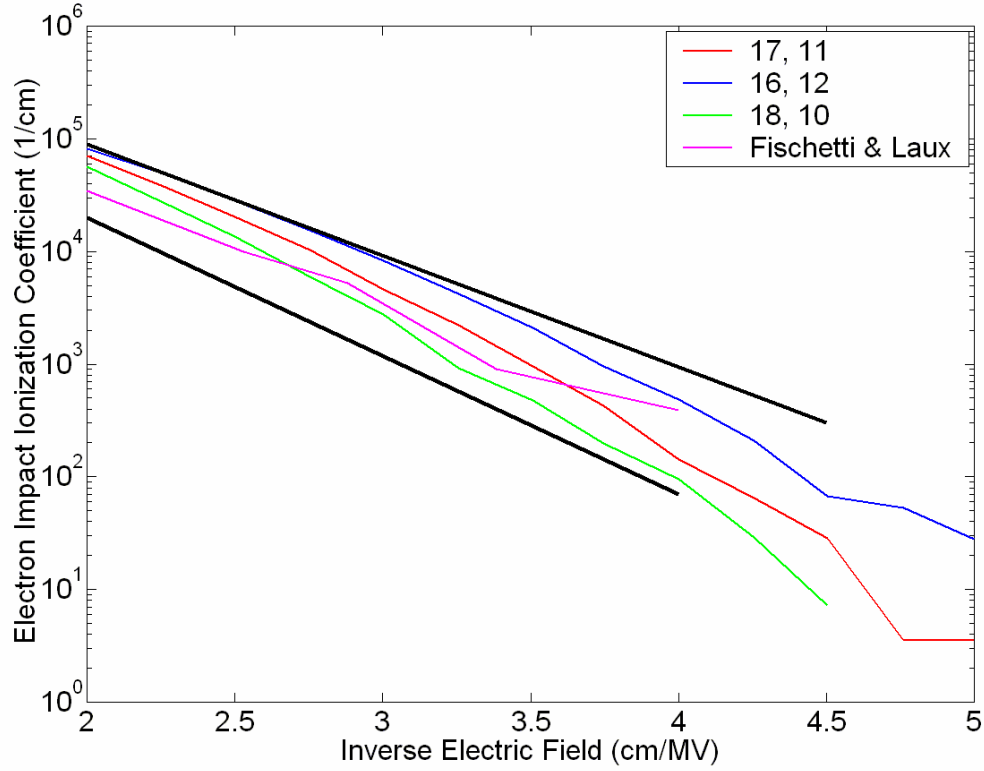


**Figure 25: Electron impact ionization coefficient vs. the inverse of the applied electric field in GaAs for several different pairs of acoustic deformation potentials. Also plotted is the theoretical work by M. Fischetti and S. Laux. The black lines represent the spread in reported impact ionization coefficients obtained by both experimental and theoretical methods.**

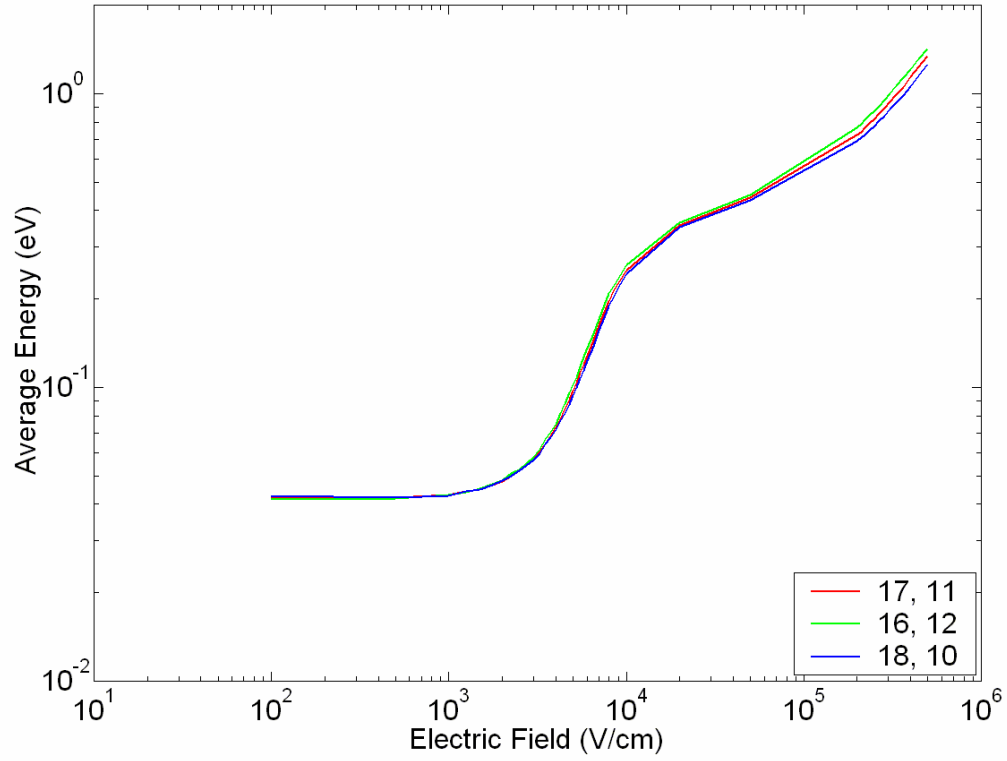


**Figure 26: Average carrier energy vs. applied electric field in GaAs for various pairs of acoustic deformation potentials. It is useful to notice that at these fields, there is a degree of insensitivity to the acoustic deformation potentials, indicating there is some room for error in exactly setting them.**

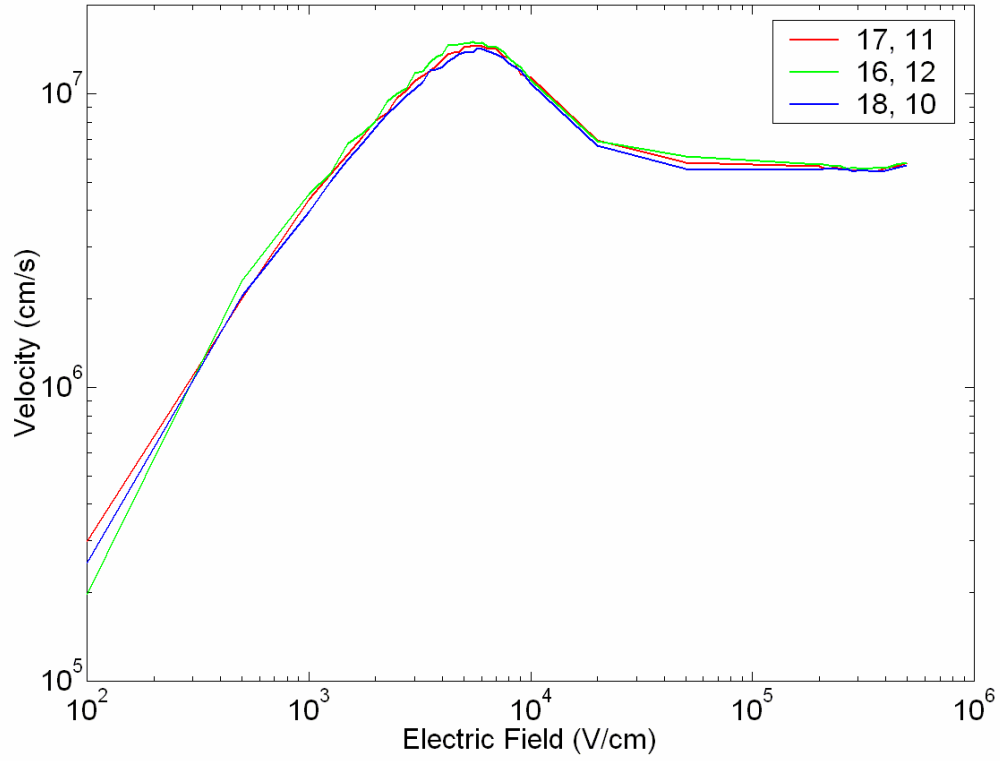


**Figure 27: Average carrier velocity vs. applied electric field in GaAs for various pairs of acoustic deformation potentials. It is useful to notice that, like the average energy, there is a degree of insensitivity to the acoustic deformation potentials, indicating there is some room for error in exactly setting them.**

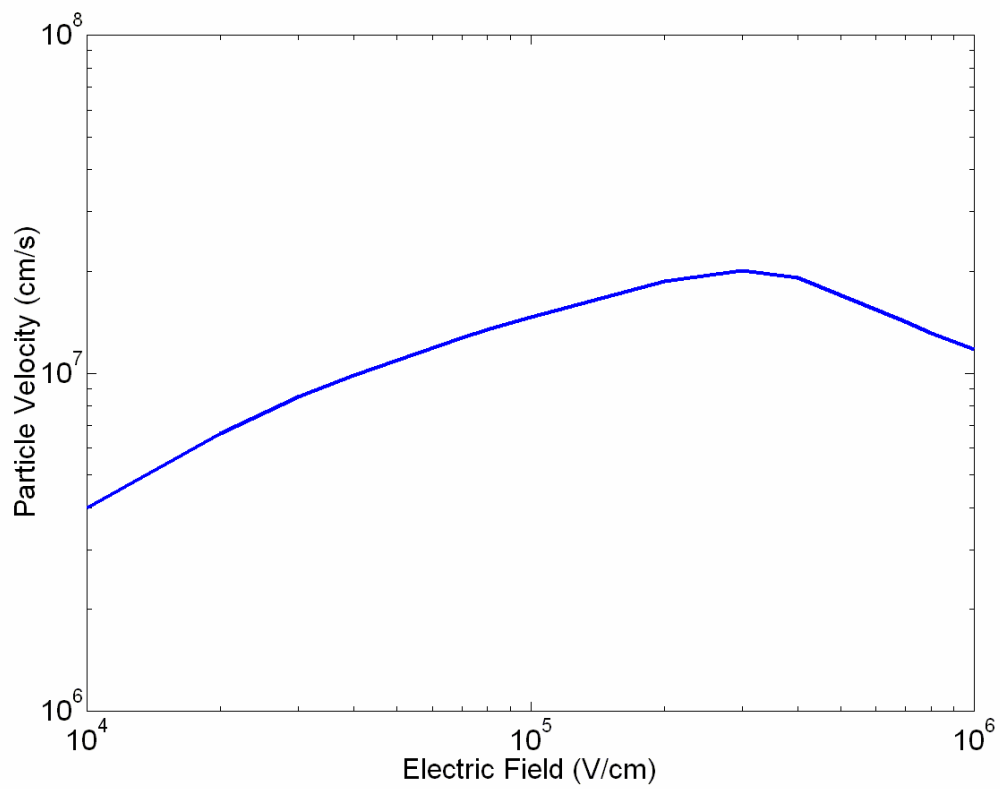


**Figure 28: Average carrier velocity vs. applied electric field in 3C-SiC.**

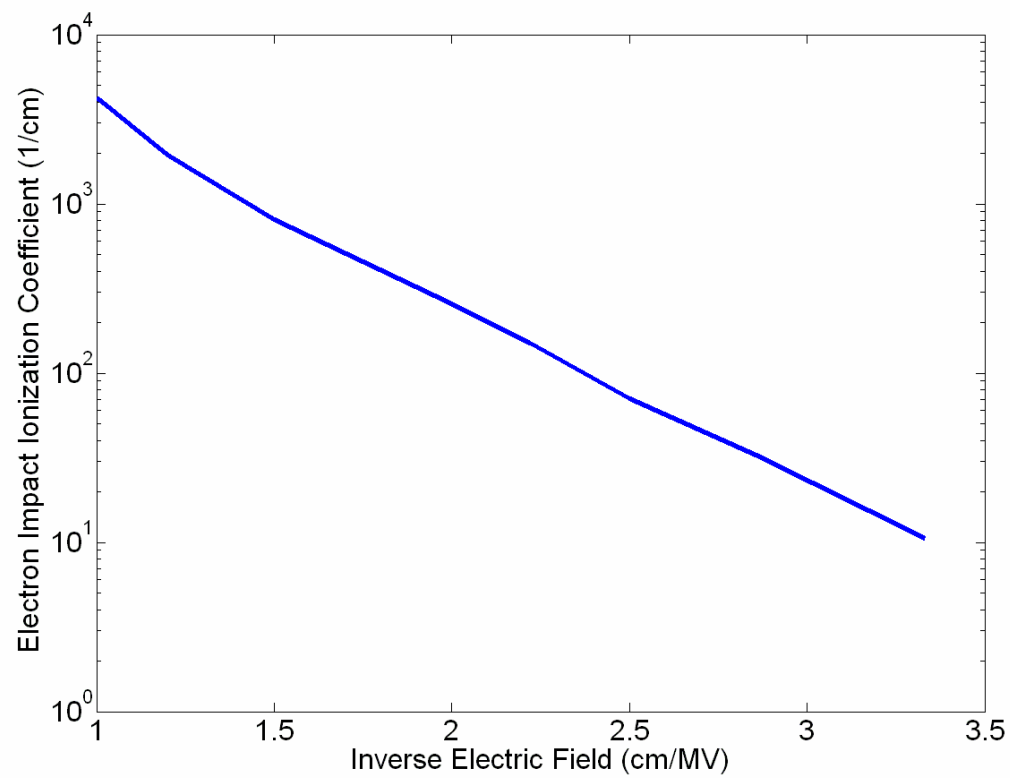


**Figure 29: Electron impact ionization coefficient vs. the inverse applied electric field in 3C-SiC.**

**Table 2: Acoustic deformation potential pairs obtained for the three semiconductor systems used in this work.**

<b>Material</b>	<b>Intra-band</b>	<b>Inter-band</b>
GaAs	<b>17</b>	<b>11</b>
GaN-ZB	<b>10</b>	<b>10</b>
3C-SiC	<b>10</b>	<b>8</b>

## CHAPTER VI

### 6.1 Temperature-Dependent Scattering Rates

Unless otherwise noted, the work in this chapter has been published here [106]. By the nature of the empirical pseudopotential method, the energy-momentum dispersion relation is calculated with the lattice ions frozen in their equilibrium positions, meaning that the lattice is at zero temperature.

The phonon scattering rates have already been discussed and calculated. One consequence of the phonon scattering rates is to introduce the effect of the nonzero temperature of the lattice, via core deviations from equilibrium, on the transport dynamics of electronic carriers. In the results presented already, the temperature was set to 300K. This section will examine how the phonon scattering rates, as well as the impact ionization transition rates, change with temperature.

The temperature dependence of the phonon scattering rates is perhaps not apparent in (7), (8), and (9). The only temperature-dependence is contained within the phonon occupancy number,  $N_{op}$  or  $N(\mathbf{q})$ , as shown in (3), and repeated here:

$$N_{op} = \frac{1}{e^{\frac{\hbar\omega}{kT}} - 1} \quad (23)$$

The term  $\hbar\omega$  is the phonon energy for a particular scattering mechanism and is material-specific. This is generally assumed constant, except in the case of acoustic phonon scattering. The effect of temperature on the scattering rates can now be understood.

The temperature is expressed in the denominator of the exponent of the exponential function in the phonon occupancy number. An increased temperature will reduce the exponent in the denominator of the occupancy number, which lowers the

entire denominator in (23). Consequently, this will increase the total phonon occupancy number, raising the scattering rates.

The three scattering mechanisms, acoustic and polar and non-polar optical, are calculated as a function of temperature. The temperatures used for GaAs are 233K, 300K, 367K, and 433K. GaN-ZB and 3C-SiC, which are stable at higher temperatures, are studied at 300K, 367K, 433K, and 500K.

The effect of temperature on the scattering rates is illustrated in Figure 30, Figure 31, and Figure 32. The total scattering rate is averaged over energy and plotted for the various temperatures. The total scattering rate is presented for clarity, as opposed to the individual, wave vector-dependent scattering rates. There is no loss of information by examining the total scattering rate. The mechanisms included are polar optical, non-polar optical, and acoustic phonon scattering. (The temperature-dependence of the impact ionization transition rate will be discussed separately.)

The total scattering rate changes more with a given change in temperature in GaAs than it does in GaN-ZB. The change in the total scattering rate is even less for 3C-SiC. The nature of this effect is contained in (23) and the polar optical phonon energies,  $\hbar\omega$ , of the three materials. Both the polar optical and acoustic scattering mechanisms are dominant over much of the useful energy bandwidth, until impact ionization becomes significant.

The acoustic phonon energies are small and do not vary widely among materials. In the calculation of the acoustic phonon scattering rate, the rate at each wave vector is comprised of possible final states across many values of  $\mathbf{q}$ . Therefore, the average phonon energy across all final wave vectors varies slowly. The polar optical phonon energies, however, are dramatically different across the three materials and are listed below in Table 3:



**Table 3: Optical phonon energies for the three semiconductor systems used in this work.**

Material	Polar Optical Phonon Energy
GaAs	35.36 meV [22]
GaN-ZB	92.0 meV [37, 107]
3C-SiC	120.0 meV [108, 109]

For these scattering mechanisms, the temperature determines the magnitude of  $N_{op}$  or  $N_{AC}(\mathbf{q})$ , and therefore the magnitude of the change in the rate with a given change in temperature. With equal changes in temperature, as was done with 3C-SiC and GaN-ZB, then, the only item that accounts for the unequal changes in the phonon scattering rates are the phonon energies.

Both phonon absorption and emission are present in each material. The emission rate is generally higher than the absorption rate due to the presence of the additive factor of one in the phonon occupancy number,  $N_{op} + 1$ , or  $N_{AC}(\mathbf{q}) + 1$ . Changes in the emission rate as a function of temperature are far more important than changes in the absorption rate in affecting the total scattering rate. In GaAs, for example, the polar optical phonon emission rate is nearly an order of magnitude higher than the absorption rate. It is useful to examine how the emission rate changes with temperature by examining the temperature dependence of the phonon occupation number.

The value of  $N_{op} + 1$ , where the optical phonon energy is used, for GaAs, GaN-ZB, and 3C-SiC as a function of temperature, is plotted in Figure 33. Inspection of Figure 33 shows that the change in the phonon occupancy number in GaAs from 300 – 433K is +21.7%, and +35.2% over the full temperature range, 233 – 433K. In contrast, the change in the emission occupancy number for 3C-SiC over the same temperature range is only +3.2% and +5.6% over the full temperature range, 300 – 500K. Therefore, the emission rate changes much more as a function of temperature in GaAs than in 3C-

SiC. The change in the emission phonon occupancy number in GaN-ZB is +10.2% over the temperature range 300 – 500K.

## 6.2 Temperature-Dependent Impact Ionization Rates

The effect of the temperature is also hidden in the calculation of the impact ionization transition rate. The calculation of the rate requires four carrier states: the initial and final states of the original particle, and the initial and final states of a secondary particle. The initial state of the secondary particle lies within the valence band, and the valence band maximum lays a distance, in energy,  $E_g$  from the conduction band minimum. This distance  $E_g$  is a function of the temperature. As the energy band gap changes, different initial valence-band states, and thus different final conduction-band states, will satisfy the energy and momentum requirements of (15). In this way, the effect of temperature is incorporated in the calculation of the impact ionization transition rate.

The only direct effect of the temperature on the band structure in this model is reflected in the adjustment of the energy band gap. Typically, empirical data, such as the Varshni equation [110, 111], is used in order to incorporate the correct energy band gap as a function of temperature. In this way, the impact ionization transition rates can be calculated at all temperatures of interest, simply by altering the band gap. It is assumed that any other alterations of the band structure as a result of the change in temperature, as well as the effect on the wave functions, is negligible.

For all three materials, it is evident that the changes in temperature have little effect on the transition rate, by inspection of Figure 34, Figure 35, and Figure 36. The reason lies in the magnitude of the change in the band gaps, as a function of

temperature. 3C-SiC is referred to as an example. The band gap of 3C-SiC at 300K is 2.20 eV, and about 2.07 at 500K. The energy gap narrows by 5.77% with a 66.7% increase in temperature. Such a small shift in the energy band gap has a nearly negligible effect on the calculated transition rate. The high-energy portion of the scattering rate spectrum, including impact ionization, where impact ionization dominates, remains unaffected by temperature for all three materials.

It is assumed that the only effect of consequence of a change in temperature on the electronic band structure is manifested by a change in the energy band gap. This follows from the use of band structures calculated with the empirical pseudopotential method. Second, a change in temperature has a variable effect on the total phonon scattering rate, particularly emission, depending on the magnitude of the optical phonon energy. A relatively small optical phonon energy results in a total scattering rate that can change significantly with a given temperature change.

Conversely, materials with relatively large optical phonon energies have emission scattering rates that tend to be immune to temperature changes, at least for the extent of the temperatures discussed thus far. Finally, while the energy band gap narrows with increased temperature, it does so modestly with the temperatures discussed in this chapter. This change in the energy band gap has been shown here to be insufficient to affect substantially the density of states that satisfy the energy and momentum requirements of the solution to the impact ionization transition rate. This leads to the effect of temperature on the transport properties of the materials discussed thus far.

### 6.3 Temperature-Dependent Transport Properties

In the calculation of the transport properties, including the velocity v. electric field curve, average energy v. electric field, and impact ionization coefficients, the same general methodology was used for all of the materials. The only difference among the materials studied was the set of electric fields and temperatures used. Since GaN-ZB breaks down at much higher fields than does GaAs, it is necessary to perform the simulations over different field strengths. In addition, the larger energy band gaps of 3C-SiC and GaN-ZB compared to the energy gap of GaAs implies that GaAs becomes intrinsic at lower temperatures. Once the semiconductor becomes intrinsic, it is not only unusable in most semiconductor devices, but many of the assumptions of the model may be called into question. Therefore, temperatures of 300K, 367K, 433K, and 500K are used for both GaN-ZB and 3C-SiC, while GaAs is limited to 233K, 300K, 367K, and 433K.

In each bulk transport simulation 10,000 initial particles are used. The final number of particles, of course, varies by material and field, as a result of the creation of secondary carriers after impact ionization events. Fewer than 8,000 new particles are created during the highest simulation field for GaAs, while well in excess of 1,000,000 particles are created during the highest simulation field for GaN-ZB. Each calculation, at each field, is performed for a simulation time of 5 ps. The first 2.5 ps allow the material to reach steady state, and the second 2.5 ps is used to evaluate the impact ionization coefficients. Statistics related to average energy and carrier velocities are collected continuously, and averaged over several time steps; this acts as a rudimentary noise-reduction mechanism.

The impact ionization coefficient segment of the simulations, at each temperature, were repeated five times, for two reasons. First, it allowed the effective

particle count being simulated to be 50,000 initial particles. The increased sample size increases the accuracy of the results, particularly at the onset of breakdown where a small number of impact ionization events may occur. Even smaller deviations in the number of impact ionization events, then, can cause noisy fluctuations in the impact ionization coefficients at these fields. Second, by simulating several groups of 10,000 particles, error measurements in the results can be discussed.

Since the high-field transport properties are most applicable to high-power, high-frequency devices, it is most informative to examine the effect of temperature on the impact ionization coefficients. The impact ionization coefficients change noticeably with temperature in GaAs. This is illustrated in Figure 37, and is consistent with the experimental results observed by Zheng, et al [61]. The error of as much as 10-15% at the lowest fields illustrates the somewhat noisy number of impact ionization events at the onset of breakdown. The error at electric field strengths above  $\sim 10^3 \text{ kV/cm}$  is much less, on the order of  $\sim 1-3\%$ .

The impact ionization coefficients for GaN-ZB and 3C-SiC are plotted, as well, in Figure 38 and Figure 39, respectively. The magnitude of the decrease in the impact ionization coefficients is smaller in GaN-ZB than in GaAs. Ando, et al [112] note this behavior in GaN-ZB as well. Their work also suggests the change in shape of the impact ionization coefficient curves at very high fields, as well. The decrease is even smaller in 3C-SiC; and in fact, the impact ionization coefficients display almost no variation at the examined temperatures in 3C-SiC.

Since the band gap energy for all of these materials changes with temperature by a relatively small amount, the calculated decrease in the impact ionization coefficients in GaAs cannot be fully attributed to the shift in the band gap. As discussed above, the impact ionization transition rates for all three materials are relatively temperature insensitive, at least for the range of temperatures examined here. Therefore, the

measurable change with temperature of the ionization coefficients must be attributable to the temperature dependence of the phonon scattering rates instead.

The decrease in the impact ionization coefficients not only follows the experimental work of Bulman [60] in GaAs, but it also follows the theoretical work with *p*-Si by Roze, et al [113]. In the work by Roze, et al, the hole impact ionization coefficients were examined for temperatures between 77-450K. Their work agrees with this work in two important respects.

First, the impact ionization coefficients, in general, decrease with increasing temperature. The explanation for this effect is one of the primary themes of this chapter. Second, Roze, et al observed that at very high fields, the coefficients tended to be relatively insensitive to the increase in temperature.

That phenomenon is observed in the impact ionization coefficients for the three semiconductors discussed in this work. Once a material is under the influence of a sufficiently high electric field, the magnitude of the scattering rates is irrelevant, since the average carrier energy would suggest that a larger segment of the total carrier distribution is subject to impact ionization as the dominant scattering mechanism.

Finally, the experimental work of Ruch and Kino [11] at low fields in GaAs show that the velocity *v*. field curve shifts down as the temperature is increased. Although not presented here, the Monte Carlo simulator does produce the same results in low-field transport analysis.

## **6.4 More Temperature-Dependent Transport Properties of 3C-SiC**

In the previous section, it was shown that the impact ionization coefficients of 3C-SiC are relatively immune to the change in temperature over the range of temperatures

examined. Much of the argument centered on the effect of temperature on the phonon scattering rates, and in particular the emission of phonons. However, it is likely that at some temperature the impact ionization coefficients will decrease as a result of sufficiently elevated phonon scattering rates.

With a change in temperature from 300K to 500K, the term  $1+N_{op}$  in GaN-ZB changes by +10.2%. As was shown in Figure 38, this change in temperature had a noticeable effect on the impact ionization coefficients, particularly at the lower fields. It was then simple to find a temperature that caused a comparable increase in  $1+N_{op}$  for 3C-SiC to see its effect on the impact ionization coefficients. Between temperatures of 300K and 650K,  $1+N_{op}$  in 3C-SiC changes by +12.2%. There is a +6.3% increase in  $1+N_{op}$  between 500K and 650K. Recall, the increase of  $1+N_{op}$  between 300K and 500K was +5.6%. The results of the impact ionization coefficient analysis are shown in Figure 40, which is Figure 39 with the inclusion of the impact ionization coefficients at 650K.

Figure 37 shows that over the temperature range of interest for GaAs, the impact ionization coefficients dropped between a half and a full order of magnitude. The drop in the impact ionization coefficients for GaN-ZB was less, as discussed above, and approximately half an order of magnitude. With the +12.2% increase of  $1+N_{op}$  in 3C-SiC, the impact ionization coefficients drop by over an order of magnitude.

The temperature of 650K is high by most standards; it is over 710°F. In order to accept the analysis of a temperature of 650K on the impact ionization coefficients of 3C-SiC, it is first necessary to establish that the model is valid. A measure of the validity of the model is the intrinsic carrier concentration,  $n_i$ , at this temperature. The equation for  $n_i$  is written [114]:

$$n_i(T) = 2 \left( \frac{2\pi k T}{h^2} \right)^{3/2} (m_e^* m_h^*)^{3/4} e^{-E_g/2kT} \quad (24)$$

In (24),  $E_g$  is the energy gap evaluated as  $E_g(T)$ . The terms  $m_e^*$  and  $m_h^*$  are the effective masses at the conduction band minima and valence band maxima, respectively. The hole effective mass is taken as  $1.00m_0$ , while the electron effective mass is taken as  $0.344m_0$  [110]. Using the same empirical data used in the temperature-dependent impact ionization analysis thus far, the energy gap of 3C-SiC at 650K is taken as 1.997eV.

The intrinsic carrier concentration,  $n_i$ , at 300K is  $8.8 \times 10^{-22} \text{ cm}^{-3}$ , while at 650K it is  $4.8 \times 10^{-10} \text{ cm}^{-3}$ . It is not expected that a change in the intrinsic carrier concentration of this magnitude would affect the validity of the material-theory based model [115]. Instead, this elevated temperature would more likely contribute to collisional-broadening effects [115].



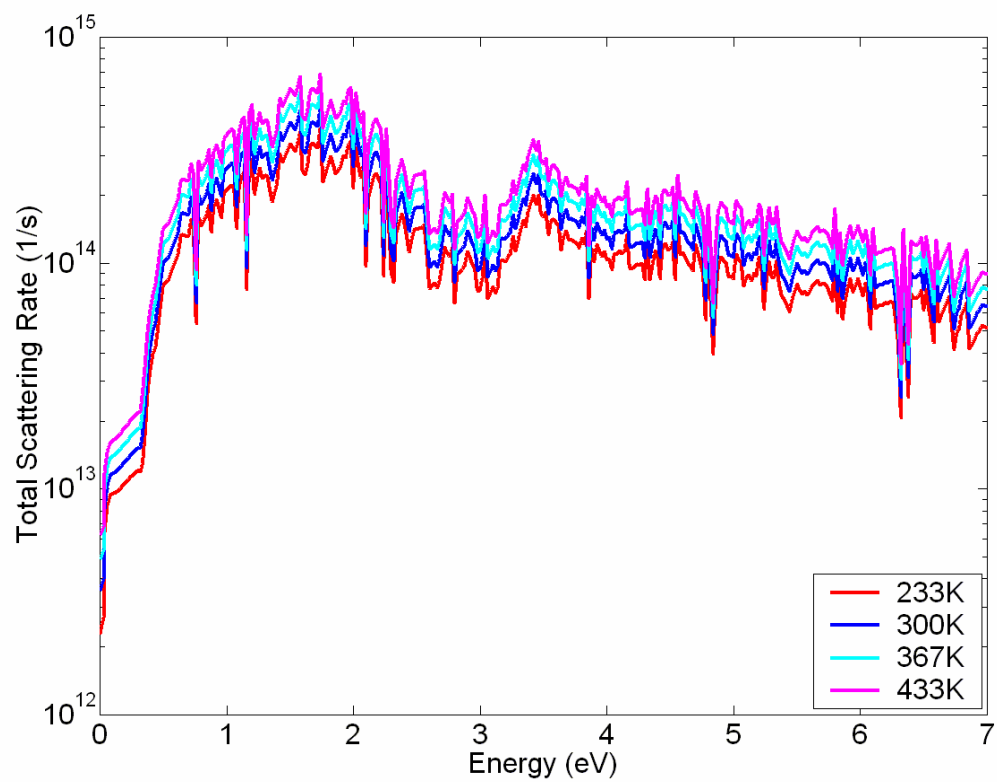


**Figure 30: Total scattering rate for GaAs for the temperatures used in the bulk transport analysis simulations. Temperatures of 233K, 300K, 367K, and 433K were used.**

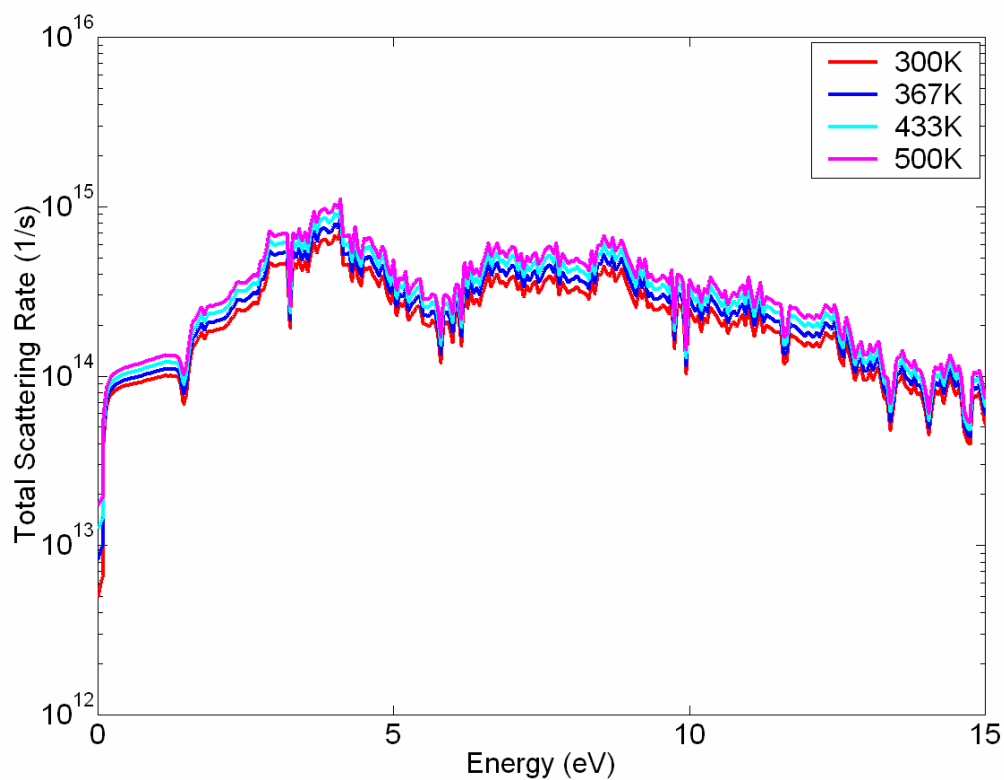


**Figure 31: Total scattering rate for GaN-ZB for temperatures used in the Monte Carlo transport analysis simulations. The total scattering rate is shown to rise with an increase in temperature. Temperatures of 300K, 367K, 433K, and 500K were used.**

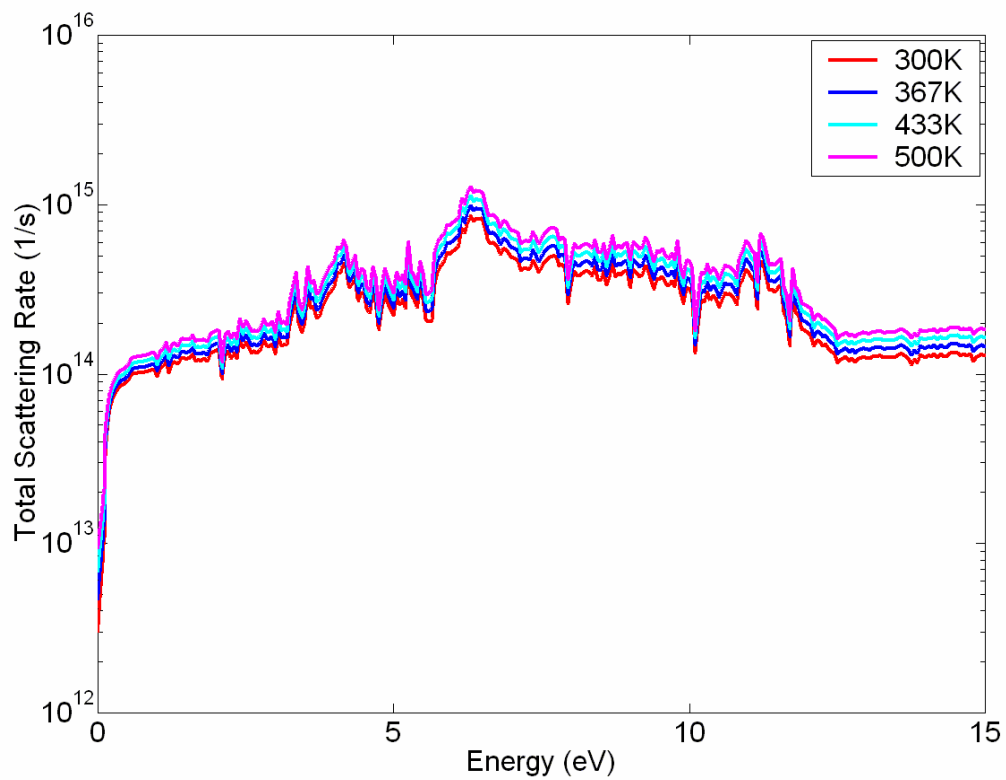


**Figure 32: Total scattering rate for 3C-SiC for temperatures used in the Monte Carlo transport analysis simulations. The total scattering rate is shown to rise with an increase in temperature. Temperatures of 300K, 367K, 433K, and 500K were used.**

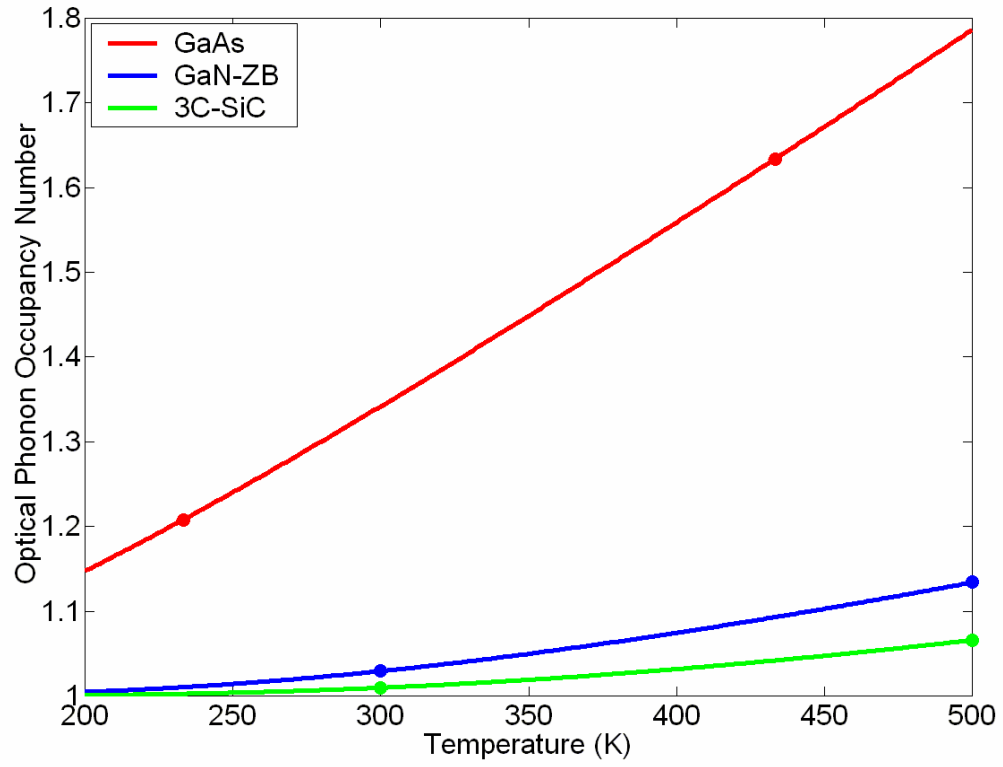


**Figure 33: Optical emission phonon occupancy number ( $N_{op}+1$ ) plotted versus temperature for GaAs, GaN-ZB, and 3C-SiC.**

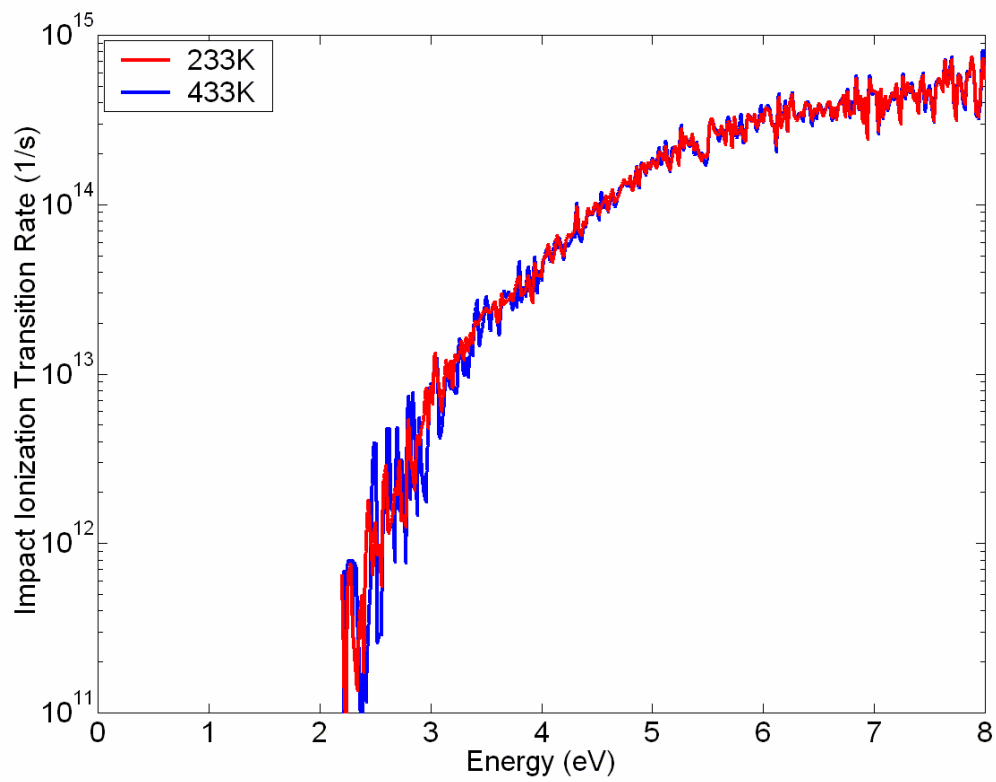


**Figure 34: Impact ionization transition rate in GaAs at 233K and 433K.**

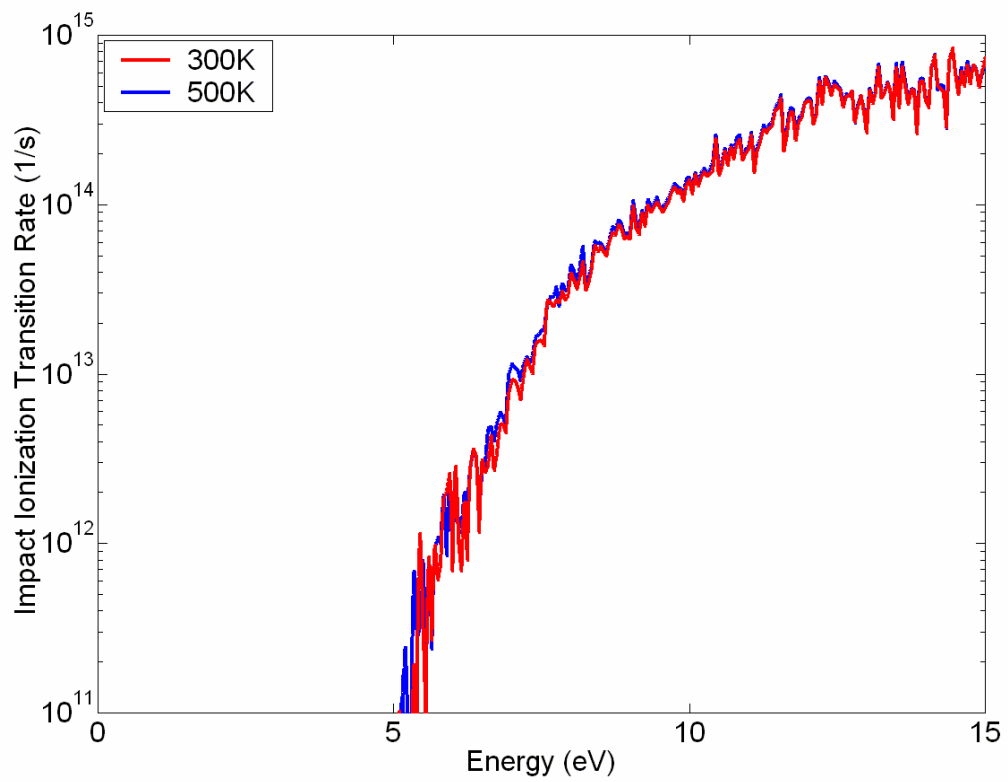


**Figure 35: Impact ionization transition rate in GaN-ZB at 300K and 500K.**

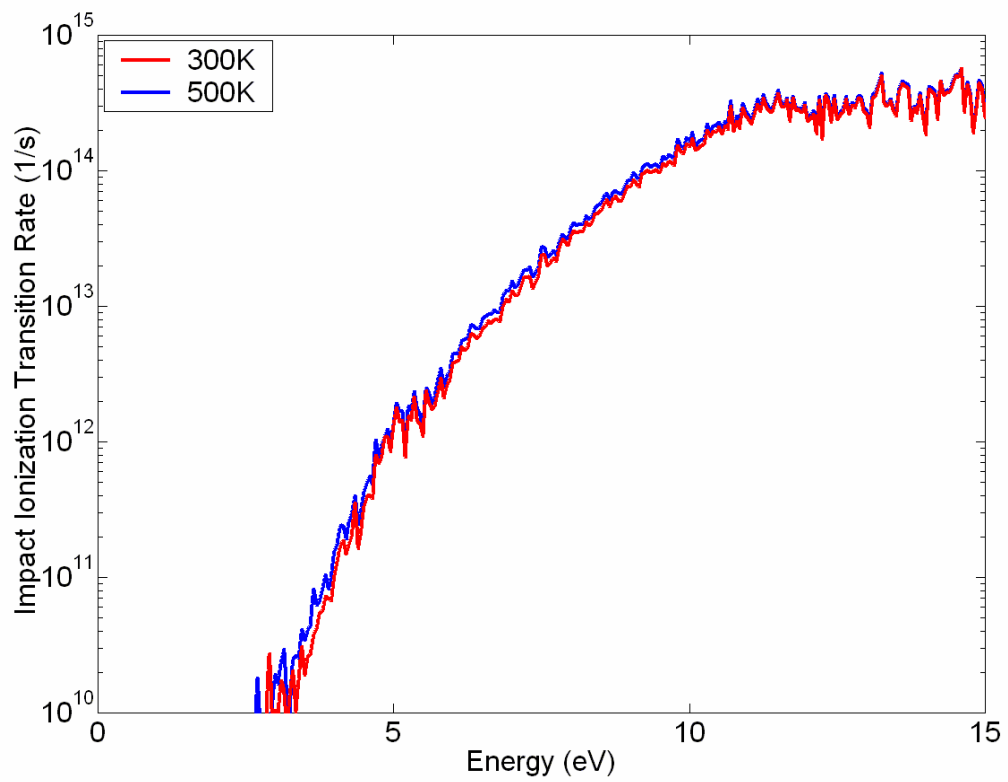


**Figure 36: Impact ionization transition rate in 3C-SiC at 300K and 500K.**

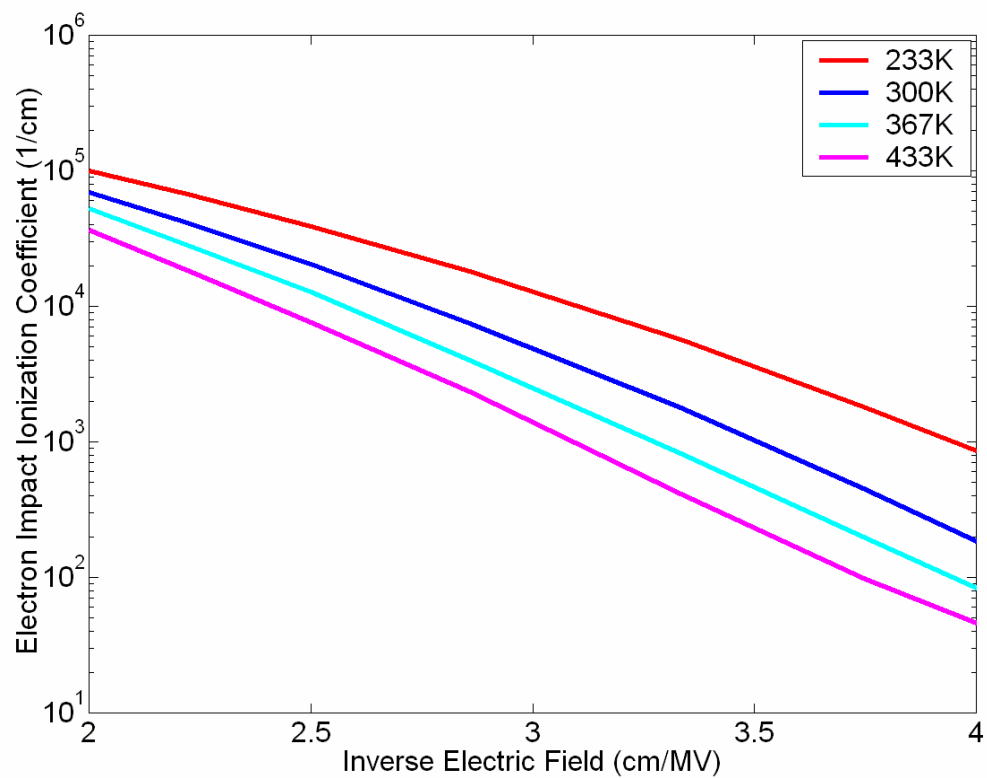


**Figure 37: Electron impact ionization coefficients in GaAs as a function of temperature.**



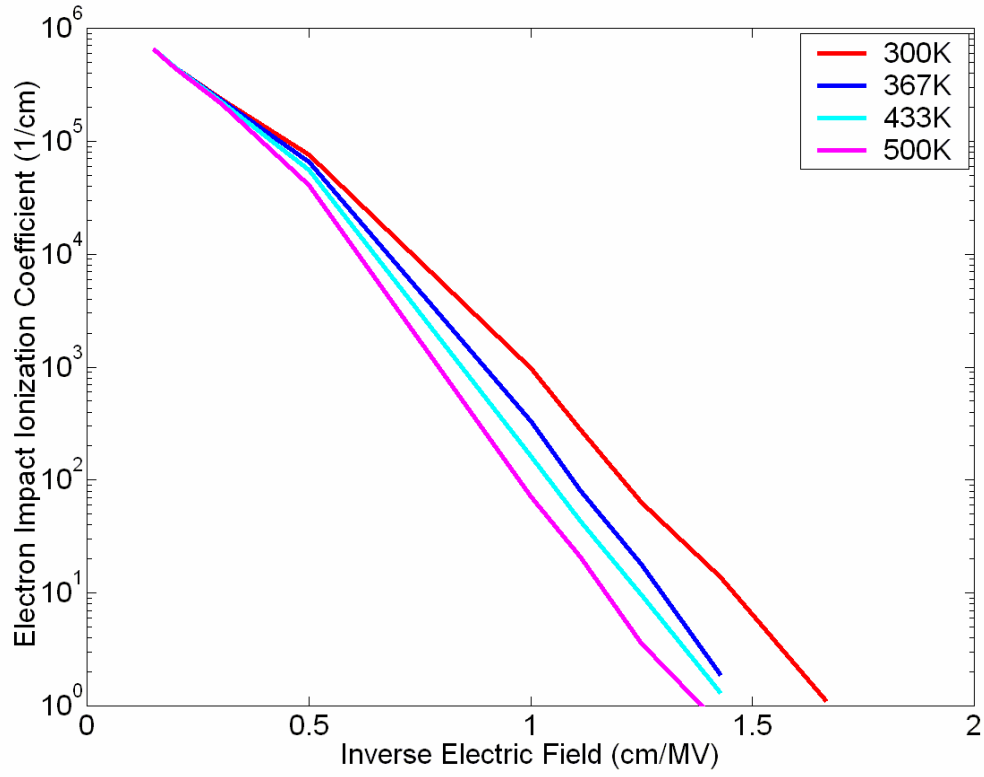


**Figure 38: Electron impact ionization coefficients in GaN-ZB as a function of temperature.**

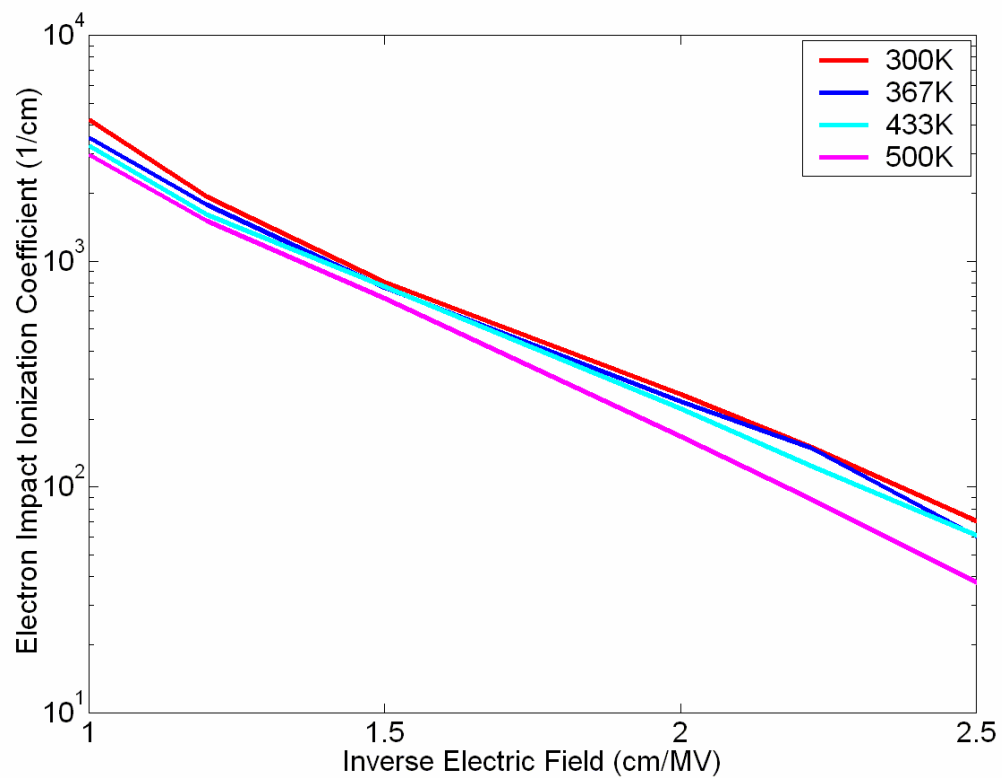


**Figure 39: Electron impact ionization coefficients in 3C-SiC as a function of temperature.**

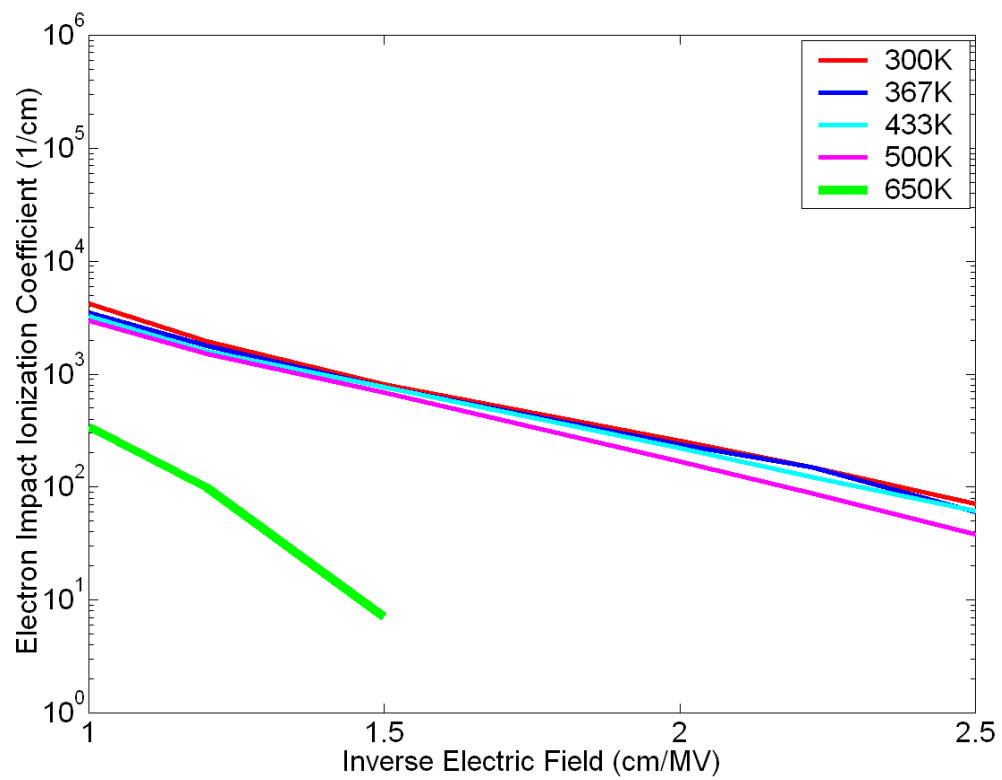


**Figure 40: Electron impact ionization coefficients in 3C-SiC as a function of temperature, with the additional temperature of 650K.**

## CHAPTER VII

### 7.1 Bipolar Simulations

One of the goals of this work has been the development of a fully numerical Monte Carlo simulator. This work began with the establishment of a simulator that could extract bulk electrical transport properties from the numerical electronic band structure. No assumptions are made about the nature of a material. By adding an additional layer to the bulk simulator, specifically the Poisson solver, and the simulator can be used to analyze device performance in a self-consistent manner. Results generated with this feature can be found in [116, 117].

The layer that includes the Poisson solver imposes boundary conditions and updates the potential and field throughout the device. The ohmic contacts and Schottky barrier are modeled numerically using Dirichlet conditions. All other boundaries on the device are modeled with Neumann conditions. Further detail on the device simulator can be found in the references.

In the device simulator and bulk results reported to this point, the electrical properties of a material are stated as a function of the majority carrier species, usually electrons. In almost all Monte Carlo semiconductor simulators in use [28, 29, 30, 32], only single carrier behaviors are studied.

This technique is not acceptable, however, in analyzing the behavior of devices whose performance is characterized by the transport properties of both carrier species. Device simulations that would require a bipolar simulator include bipolar junction transistors (BJTs), metal-oxide-semiconductor field effect transistors (MOSFETs), and heterojunction bipolar transistors (HBTs). In addition, included in the list of these devices are most semiconductor-based photodetectors, where device performance is a function of the production of an electron-hole pair (EHP). Upon absorption of a photon,

a single EHP is created, and each particle is collected at different locations within the device. Therefore, it is necessary to be able to follow both carriers simultaneously.

The ability to follow both carrier species simultaneously requires a bipolar simulator. An extension of the Monte Carlo simulator to a bipolar Monte Carlo simulator imposes technical challenges, some larger than others. It has been noted by Laux, et al [103] that conceptually at least, the inclusion of holes in the simulator is analogous to electrons and indeed, relatively simple.

In addition to the technical challenges posed, an opportunity exists to refine further the underlying numerics of the simulator with respect to the final state selector for impact ionization events. This opportunity and the associated challenges will be addressed in the following sections of this chapter.

## **7.2 General Bipolar Modifications to the Monte Carlo Simulator**

The most straightforward modification that is required of the simulator is statistical. It is necessary to double the number of statistical counters in order to be able to collect independent carrier data for both electrons and holes.

The second change required is also minor and regards the drift process. Since the electrons and holes have opposite charge, they will drift in opposite directions in response to an applied electric field. Therefore, before determining the outcome of a drift process, it is necessary to first identify the carrier species.

Next, it is necessary to store the entire electronic band structure, which includes the four conduction and four valence bands. Along with the required wave functions, this change doubles the amount of computer memory required to handle the band structure. This amount is non-negligible, particularly with respect to the wave functions.

In Chapter V, it was shown that for the carrier-phonon scattering events, a fine mesh was used to obtain the final state as a function of the final state energy. This mesh was generated with a mesh resolution of 0.0025 in normalized  $\mathbf{k}$ -space. There are 43,390,408 mesh points in a mesh of this resolution. Each mesh point includes the 3-dimensional  $\mathbf{k}$ -vector, the band index, the associated energy and the wave function database index. The memory requirement of a single point is 24 bytes; the entire mesh, then, consumes over 1 GB of memory, twice the requirements of the single carrier simulator in order to accommodate twice the number of carrier bands. This is a large amount of memory, even given today's relatively low computer memory prices.

The final general change to the Monte Carlo simulator is associated with the statistical reporting system; the number of output files doubles in order to provide separate statistics for both carrier species. Internal statistical variables also double in order to store identical transport data for both carrier types. After these general changes have been made, the simulator can be set for any number of initial electrons and holes. Both carrier species drift under the same user-defined applied electric field, and the simulator will produce the same transport properties for electrons and holes as are produced by the single carrier simulator beneath the threshold for breakdown.

### 7.3 Bipolar Impact Ionization Final States

With consideration to device breakdown [iii], however, there is an opportunity for refinement to the simulator. Specifically, the final state selector for impact ionization

<sup>iii</sup> A distinction is made here with respect to device and material breakdown, and which of the two is referred to here. Although bulk studies do not simulate a particular device, the "device" is the

events should be modified to portray more accurately a full-band model. The standard process for choosing a final state for impact ionization can be found in [22], and works as follows. The final state of the initiating carrier (assume an electron, in this case) is assigned a final energy,  $E_f = E_i - E_{gap}$ . A random wave vector at this energy,  $E_f$ , is selected. The secondary particle is assigned to the minimum of the conduction band.

While this is the most common formulation for the final state selector for impact ionization events, there are several weaknesses with this approach. First, it accounts poorly for DOS effects [22]. Also, no attention is paid to the matrix element and overlap integrals.

The method described above is not completely without merit, however, very near the breakdown threshold; it becomes questionable deeper into breakdown. Near breakdown, which generally occurs in the vicinity of carrier energies twice the band gap, it is reasonable to assume that the carrier loses energy of roughly the magnitude of the gap. The fundamental flaw with this approach is that momentum is not conserved. The importance of the conservation of momentum in the impact ionization process is easily illustrated by the contrast between the calculation of impact ionization rate with and without Umklapp processes.

The new final state selector conserves energy and momentum across four carrier states, and can accommodate the effects of the matrix element and wave function overlap integrals. As impact ionization was discussed in detail in Chapter IV, energy and momentum must be conserved across four carrier states, which are the initial and final states of the initiating carrier, and the initial and final states of the secondary carrier.

bulk material of infinite size, where carriers are generated as a result of impact ionization processes. In contrast, the entire model provided by the Boltzmann equation fails to remain valid under conditions of material breakdown.

The most direct approach that may be used in the selection of the final states is to use the identical algorithm as is employed in the Monte Carlo integration of the actual impact ionization transition rate. In this way, energy and momentum are conserved, the matrix element is considered, and Umklapp processes are also included.

The Monte Carlo integration approach is employed in the calculation of the impact ionization transition rate because the calculation is too time-consuming to compute entirely, as in the case of the carrier-phonon scattering rates. Even with the Monte Carlo integration, however, the task would still be too time-consuming to be incorporated into a final state selector for a Monte Carlo bulk/device simulator; only aspects of the Monte Carlo integration are incorporated.

During the Monte Carlo integration of the impact ionization rate, it is possible to calculate additional statistics as the rate is being computed. The most useful data for the final state selector are the average energies of the secondary carriers. Since the initiating carrier energy is already known, the fourth energy can be found with simple arithmetic. Then it will be necessary to take all of these possible cases where energy is conserved and find the subset where momentum is also conserved.

Elements of this approach were used by Jung, et al [104]. In this paper, the authors outline a method for an improved impact ionization model for use in Monte Carlo simulations of GaAs. They numerically calculate the impact ionization transition rate and fit two simple, linear functions to the resulting data in order to obtain the secondary electron energy given the energy of the initiating electron. The enhancements made to the final state selector in the Monte Carlo simulator discussed in this thesis go beyond the work of Jung, et al [104]. Jung, et al make an additional enhancement to the standard impact ionization final state model by not assuming that the energy lost to impact ionization is merely the energy gap. The work of Kunikyo, et al [118], addresses hole-initiated impact ionization and includes a model for the energy of both secondary



carriers. In this thesis, however, not only is the energy of the secondary hole considered, but momentum across all four states is also conserved.

The process begins by computing the impact ionization transition rate for both electrons and holes in GaN-ZB. The electron-initiated impact ionization transition rate was presented in Figure 21. The hole-initiated impact ionization rate is calculated in the same fashion, although not shown here.

During the calculation of both the hole- and electron-initiated impact ionization rates, the average energies of the secondary carriers are recorded. For the case of electron-initiated impact ionization in GaN-ZB, this is shown in Figure 41. Here, the average energies of the secondary electron and hole are plotted as a function of the energy of the initiating electron.

From the secondary carrier energy curves it is simple to extract functions, which, given the initiating carrier energy, provide the energies of the secondary electron and hole. The use of a software tool such as Matlab® is helpful for this task. The functions used in this simulator follow below.

$$E_e = \frac{\frac{0.007792}{eV^4} E_i^5 - \frac{0.2935}{eV^3} E_i^4 + \frac{3.973}{eV^2} E_i^3 - \frac{11.37}{eV} E_i^2 + 8.992 E_i - 1.074 eV}{\frac{E_i^2}{eV^2} + \frac{7.944}{eV} E_i + 88.95} \quad (25)$$

In (25),  $E_i$  is the initial energy of the initiating, high-energy electron, and  $E_e$  is the final energy of the secondary conduction electron created as a result of the impact ionization event. The function that determines the energy of the hole that is created,  $E_h$ , as a result of the event is shown here:

$$E_h = \frac{\frac{3.846}{eV^4} E_i^5 - \frac{104.8}{eV^3} E_i^4 + \frac{835.9}{eV^2} E_i^3 + \frac{175.2}{eV} E_i^2 - 135.7 E_i - 98.02 eV}{\frac{E_i^5}{eV^5} - \frac{29.46}{eV^4} E_i^4 + \frac{253.0}{eV^3} E_i^3 - \frac{200.7}{eV^2} E_i^2 + \frac{540.4}{eV} E_i + 369.9} \quad (26)$$

Note that the value obtained in (26) is greater than zero. Since the zero energy point is defined to be the minima of the conduction band, it should follow that all valence band energies are less than zero. In reality this is the case, but computationally, it is more natural to consider the hole energies as positive.

The final state energy functions are plotted over the results in Figure 41, and are shown in Figure 42. While the functions exist at energies below threshold, they produce values near zero. In addition, the determinant of an impact ionization event is the magnitude of the impact ionization transition rate, found in the scattering rate database. Therefore, given an initiating carrier energy of less than 5.0 eV, the impact ionization process would not be chosen.

The same process is repeated for hole-initiated impact ionization. Figure 43 and Figure 44 show the complementary results for holes. Again for computational purposes, the energies of the holes are considered positive, and the electron energies, then, are negative. The equations which describe the energy relationship are as follows:

$$E_e = \frac{\frac{0.1096}{eV^2} E_i^3 - \frac{1.043}{eV} E_i^2 + 2.643 E_i - 1.368 eV}{\frac{E_i^2}{eV^2} - \frac{19.41}{eV} E_i + 108.8} \quad (27)$$

In (27) the energy for the secondary electron is given, and again, the value of the energy is positive and the final state algorithm ensures that the particle is chosen from the correct band. The energy of the secondary hole is given as:

$$E_h = \frac{\frac{291.3}{eV^4} E_i^5 - \frac{5470.0}{eV^3} E_i^4 + \frac{3.844e4}{eV^2} E_i^3 - \frac{1.226e5}{eV} E_i^2 + 1.669e5 E_i - 6.464e4 eV}{\frac{E_i^5}{eV^5} + \frac{2448.0}{eV^4} E_i^4 - \frac{6.559e4}{eV^3} E_i^3 + \frac{6.748e5}{eV^2} E_i^2 - \frac{3.150e6}{eV} E_i + 5.60e6} \quad (28)$$

Since three of the four energy unknowns are now known, it is simple to obtain the final energy of the initiating carrier as a result of the impact ionization event. Once this occurs, the energies of all four carriers are known, and one step remains before the final

states can be selected. As was done for the phonon scattering events, given a final energy, it is possible to query the existing  $E-k$  database to find all possible final states with that energy.

Three lists of carriers are created, each corresponding to all possible final states that satisfy the energy requirements of the impact ionization event. It is necessary to test all combinations of the wave vector of the points in the three lists, along with the wave vector of the initiating carrier, in order to find all sets of points that now also satisfy the conservation of the wave vectors.

As was the case in the calculation of the impact ionization transition rates themselves, the satisfaction of momentum conservation is a computationally time-consuming process. Even with a relatively small number of points, say on the order of  $10^2$  in each of the energy conserving lists, it is easy to see that the total number of combinations that are to be tested for momentum conservation can be quite large. Once a list of the combinations of points that satisfy both energy and momentum conservation is obtained, it is possible to pick one set to be used as the final states of the three carriers.

## **7.4 Hole Transport in GaN-ZB**

The use of the Monte Carlo simulator for electron transport has consumed most of this thesis to this point. Before moving to the bipolar Monte Carlo simulator and a simple device example, it is useful to show that the simulator is effective in producing correct hole transport properties. Again, the material chosen will be GaN-ZB, since it will be used as the test material in the device application and because the hole transport properties can be compared to published data, specifically to the work published in [50].

As was the case with electron transport, it is first necessary to calculate the hole-phonon scattering rates and the hole-initiated impact ionization transition rate. Then, in line with Chapter V, the acoustic deformation potentials are chosen such that the hole transport properties agree with available data. The total energy-dependent hole scattering rate is shown in Figure 45. The acoustic scattering rate portion of the total scattering rate incorporates the chosen values of the acoustic deformation potentials. Next, the low- and high-field electronic transport properties of holes were simulated with the single carrier simulator. The results are shown in Figure 46, Figure 47, and Figure 48, and they agree with those reported in [50].

Accurate, unipolar hole and electron transport in GaN-ZB has now been summarized. All that remains before moving to the simple device simulation is to discuss the bipolar bulk transport properties. The discussion will address two separate regimes of transport, low-field and high-field.

In both cases, the coupling between electron and hole states is weak, since spontaneous generation and recombination is neglected. These events occur on time scales on the order of nanoseconds, whereas the entire bulk simulations take place in the time frame of picoseconds. Therefore, it is assumed that these events occur too rarely to contribute significantly to the transport properties.

Under the low-field regime, there is no interaction between electrons and holes as the simulator is formulated. It is therefore expected, and observed, that the low-field transport properties of electrons and holes with the bipolar simulator recover the results generated by the single species simulator. This is shown in Figure 49 and Figure 50 for the case of hole transport. The noisier bipolar data reflects a much smaller hole ensemble size and simulation time than was used in the unipolar simulation.

With the impact ionization coefficient work done previously, it was not unreasonable to analyze the behavior of 10,000 carriers for 3-5 ps to generate the

impact ionization coefficient for a single field. The time-consuming nature of the bipolar final state selector, and particularly at threshold energies and fields, prohibits a wide-spectrum study of the impact ionization coefficients at this time.

The impact ionization coefficients can be noisily observed for very small ensemble sizes (<100 carriers) and for simulation times (< 0.5 ps). Although the results for holes in GaN-ZB are somewhat noisy, they are within reason. It would seem that the impact ionization coefficients produced by the bipolar final state simulator follow the results shown in Figure 48 in slope, but with the entire curve shifted down to a lower magnitude at any given field.

A constant shift downward in the magnitude of the impact ionization coefficients for holes in GaN-ZB can be logically explained. With the unipolar final state selector, secondary holes are initialized to the top of the valence band, which is at  $\Gamma$ , with zero energy. At  $\Gamma$ , the density of states is very low, therefore given an applied electric field, the carrier heats up rapidly from this starting point, racing toward the threshold energy of impact ionization. The carriers generated with the bipolar final state selector are rarely initialized to  $\Gamma$ . Instead, they are initialized at points with much higher densities of states. In turn, these secondary carriers do not heat up as quickly and it therefore takes longer for the secondary carriers to impact ionize. In addition, since the secondary carriers are generated with an energy greater than zero, it means that the initiating carrier loses more energy than it did under the unipolar final state selector, and is therefore cooler after an impact ionization event. It is then harder for the carrier to reach impact ionization again.

One final factor contributes to the slightly lower impact ionization coefficients. With the unipolar final state selector, when impact ionization was selected as the scattering method, there was nothing to prohibit further the impact ionization process from occurring. In contrast, with the bipolar final state selector, when impact ionization is

chosen as the scattering mechanism, energy and momentum must still be conserved in order to produce a set of possible final states. Although it does not occur frequently, it is not uncommon for impact ionization to “fail”; if impact ionization is selected, but no final states can be found, the event does not occur

## **7.5 Avalanche Photo Diodes**

Gain in APDs occurs as a result of avalanche breakdown. Injected carriers are generated by the absorption of a photon. In theory, it is desirable to have a large difference between the electron ( $\alpha$ ) and hole ( $\beta$ ) ionization coefficients in the material of the multiplication region in order to minimize multiplication noise and as a result, maximize the bandwidth [63] of the device. If gain is generated by electron multiplication, it would be desirable to have the hole impact ionization coefficient be zero. Unfortunately, this is rarely the case with most direct band gap III-V semiconductors. In these materials, the impact ionization coefficients of electrons and holes are often comparable [119]. Device techniques can be used to minimize the noise associated with nonzero gain and multiplication of the minority species, such as the use of multi quantum well structures [119].

The simulation of the multiplication region of an APD is useful for many reasons. First, it appears that there has been little analysis, theoretical or experimental, of GaN-ZB APD devices. The results generated on the gain v. reverse bias profile can be compared to the performance of other semiconductors such as the AlGaAs/GaAs system. The results can also be incorporated into higher level drift-diffusion and/or hydrodynamic model simulators for further device trend analysis.

The choice of the multiplication region illustrates the usefulness of a bipolar simulator. In certain devices, such as MESFETs, where a single carrier species is responsible for device performance, the other carrier species can be neglected altogether with little concern for its effect on the generated results. In other devices, however, it is the combination of the behaviors of both species that dictate the performance of the device. In addition, since breakdown is an essential mechanism in the APD, the need for a bipolar final state selector for impact ionization is underscored.

With the inclusion of an additional “layer” to the bulk simulator, the APD multiplication region can be simulated with relative ease. The APD device layer includes the injection mechanism, whereby a given number of electrons and/or holes at the desired injection energy are inserted on the appropriate side of the multiplication layer relative to the direction of the applied bias. The spatial coordinates of the carriers are analyzed to determine when the particle leaves the multiplication region.

Electrons and/or holes are injected into the multiplication region of predetermined width. Carriers will drift under a constant [120], applied electric field, and the simulation will conclude when all carriers have exited the multiplication region for each given field.

Since the device performance is directly related to the impact ionization process, statistics will be recorded indicating the number of impact ionization events initiated per carrier species. These values will be used to calculate the gain and noise profiles of the device.

Other statistics are also collected. A more detailed analysis of dead space will be conducted in future work; however, the simulator already collects the required data. For each impact ionization event that occurs, the carrier species, wave vector, energy, band index, and real space coordinates are recorded, along with the current simulation time at which the event occurred.

## 7.6 APD Noise and Gain Theory

Assuming electron injection, an electron current,  $J_{ei}$  is injected at one end. Due to the multiplication, or gain, resulting from impact ionization events, a larger electron current,  $J_{eo}$ , exits. Therefore, the electron multiplication [121] can be expressed as:

$$M_e = \frac{J_{eo}}{J_{ei}} \quad (29)$$

Gain in an APD, then, is a simple function of the number of carriers injected into a multiplication region and the number that exit the other side. The multiplication equation written in (29) can be rewritten as:

$$M_e = \frac{\text{Number of electrons out}}{\text{Number of electrons in}} \quad (30)$$

Equation (30) will be used as the model for calculating gain due to electron injection in the remainder of this work. In like manner, the formulation of gain due to hole injection can be written:

$$M_h = \frac{\text{Number of holes out}}{\text{Number of holes in}} \quad (31)$$

Traditionally, the Monte Carlo method has not been a reliable tool for understanding the excess noise properties of APDs [122]. While the Monte Carlo method accurately recovers the carrier behaviors and trajectories in an APD, it is often limited by the completeness of the band structure and scattering models [122]. As such, efforts have been made to devise statistical models to examine the low-frequency properties (including the gain and noise profiles) in APDs [68].

McIntyre first attempted to formulate a local-field statistical model of multiplication noise in APDs [123]. The original McIntyre theory performed well with thick multiplication regions where the impact ionization coefficients could be reasonably



described as functions only of the local electric field, and impact ionization was a local process. In other words, when the multiplication region is large and “looks” like bulk material, the model works well. The local-field theory produces the well-known formulation of the excess noise factor,  $F$ , which is a function of the gain and the ratio of the hole and electron impact ionization coefficients, given here:

$$F(M) = kM + (1 - k)\left(2 - \frac{1}{M}\right) \quad (32)$$

In thin multiplication regions, nonlocal effects are significant. It is necessary to account for the minimum path that a carrier must drift in order to gain the required energy to cross the impact ionization threshold. This minimum path is often described in terms of the “dead space” [124, 125]; the dead space is the distance required by a carrier to acquire sufficient energy to impact ionize.

Although attempts have been made, such as by Saleh, et al [125], to include a consideration of the dead space within the framework of McIntyre’s original theory, the basis of the model was hampered by its dependence on locally determined impact ionization coefficients. As McIntyre notes [68] in the introduction to his modified theory, “there is no such thing as a definable ionization coefficient which is characteristic of a specific field in a semiconductor.” Furthermore, any ionization coefficients that are measured are characteristic only of that particular photodiode structure. McIntyre was prompted to devise a new theory employing history-dependent ionization coefficients. The details of the new history-dependent McIntyre theory can be found in [68] and [122].

McIntyre’s theories are needed in the absence of other analytical tools that can be used to obtain the low-frequency performance profiles of APDs. The history-dependent theory makes many assumptions, among which is that the initiating carrier loses roughly all of its energy (relative to the band edge) after an impact ionization event. This correlates with the old formulation of the impact ionization final state selector.

The new McIntyre theory states the formulation of the noise in terms of carrier population sizes, as is given here:

$$F(x') = \frac{\langle m^2(x') \rangle}{M^2(x')} = \frac{\left\langle \left( \frac{N_e(x') + n_h(x')}{2} \right)^2 \right\rangle}{M^2(x')} \quad (33)$$

The noise calculated by the equation in (33) is given for carrier injection at  $x'$ , and the terms in the numerator on the right hand side of (33) are related to ensemble averages of carrier populations, which are a function of the history-dependent ionization coefficients. The terms  $N_e(x')$  and  $n_h(x')$  are defined by McIntyre [122].

The use of a Monte Carlo model can directly calculate the gain in a simple fashion, provided the limitations of past Monte Carlo models are overcome. Given a single carrier injection, the gain is the number of carriers, of the same species as is injected that exit the device. It is then possible to calculate the excess noise factor. Ong, et al [126] do this for GaAs  $p^+i-n^+$  APDs.

The excess noise factor,  $F$ , is the normalized second moment of the multiplication random variable,  $M$ , when a single carrier initiates the multiplication. The excess noise factor is written:

$$F = \frac{\langle M^2 \rangle}{\langle M \rangle^2} \quad (34)$$

Ong, et al defines the multiplication,  $M$ , as:

$$M = N_T + 1 \quad (35)$$

In (35),  $N_T$  is the total number of ionization events assuming single carrier injection. Equation (35) is completely equivalent to the previous definition of gain in (30) and (31) when single carrier injection is considered. The technique is valid for both

single-hole and single-electron injection. Once the gain,  $M$ , is computed from the simulation statistics, the excess noise factor,  $F$ , is easily computed.

While the approach outlined by Ong, et al is valid, the authors use analytical approximations for the band structure and scattering mechanisms. The conduction band is represented by a three valley approximation, which comprises the lowest conduction band. Also, the impact ionization transition rate is described with a Keldysh formula, and the final state selector for impact ionization events is nearly identical to the original final state selector used in earlier parts of this work.

Satyanadh, et al [127] make a similar attempt in their analysis of InAs avalanche noise, and also include several analytical approximations, including a two-valley conduction band model, two nondegenerate valence bands and analytical scattering mechanisms. As discussed by Yuan, et al [122] the simplifications made by Ong, et al and by Satyanadh, et al inhibit the reliability of results generated by a Monte Carlo simulator in the investigation of the gain and noise properties of APDs. These concerns are ameliorated by the Monte Carlo model developed in this thesis, since the foundation of the simulator is solely the numerical electronic band structure. In addition, the final state selector for impact ionization developed earlier in this chapter removes one more analytical approximation of the actual transport dynamics.

## **7.7 APD Results and Analysis**

The gain and noise profile of GaN-ZB multiplication regions begins with single-electron injection at roughly zero energy, into multiplication regions with thicknesses of 0.125, 0.25, 0.50, and 1.0  $\mu\text{m}$ . The injected electron drifts under the applied, constant electric field. All secondary electrons and holes created because of any impact

ionization processes are also tracked. The simulation continues until all carriers exit the multiplication region. The gain is calculated according to equations (30) and (31).

A single iteration of the simulation includes the gain calculation for an entire set of electric fields. For instance, in the case of the 1.0  $\mu\text{m}$  GaN-ZB multiplication region, the set of electric fields includes fields regularly spaced between 1000 and 1525  $\text{kV}/\text{cm}$ . When all of the fields in the set have been simulated once, a single iteration of the simulator has occurred, and the statistics are logged. The sets of electric fields for the 0.125, 0.25 and 0.50  $\mu\text{m}$  multiplication regions also start at 1000  $\text{kV}/\text{cm}$ , however the final field is larger than 1525  $\text{kV}/\text{cm}$  in the 0.50  $\mu\text{m}$  device, and larger still in the 0.25  $\mu\text{m}$  and 0.125  $\mu\text{m}$  devices.

While the gain vs. electric field profile is clear after a relatively small number of iterations, the standard deviations are high. Therefore, it is necessary to perform a large number of iterations in order to obtain reliable noise figures. Ong, et al [126] note that for low gain ( $M \sim 2$ ), on the order of  $10^3$  iterations are necessary, while for high gain ( $M > 8$ ), the number of iterations exceeds  $10^4$ . For this reason, the noise graphs are restricted to gains less than 10.

The gain vs. electric field profiles for the 0.125, 0.25, 0.50, and 1.0  $\mu\text{m}$  devices are shown in Figure 51. The figure displays the typical exponential gain profile associated with gain in APDs. As expected, the curves shift toward lower electric fields for a given gain as the multiplication region becomes thicker. With a given multiplication region thickness and a given electric field strength, a certain number of impact ionization events can be expected, determining the gain. But if the region is thicker, there is then room for more impact ionization events to occur before the carriers exit the region. As the multiplication region continues to get thicker, the multiplication region layer will approach bulk-like conditions, where it becomes difficult to tune the gain by varying the applied electric field.

As is the case in the work by Ong, et al [126], the purpose of the work is to investigate the dependence of the excess noise factor on the multiplication region thickness. And as they report, over the range of gains shown in Figure 51, the excess noise factor,  $F$ , falls with decreasing multiplication region thicknesses. This is consistent with some experimental measurements [128]. This also reveals the inherent flaw in McIntyre's original model of noise in (32). This equation only considers the impact ionization coefficients of the material and is therefore independent of the multiplication region size.

The excess noise factors, calculated for the same APDs whose gain profiles are shown in Figure 51, are presented in Figure 52, for gains up to 3.0. As discussed by Ong, et al, as the gain increases, it becomes necessary to have larger and larger sample sizes in order to obtain reasonable values for the excess noise factors. The sample sizes for each multiplication region are presented below, in Table 4.

**Table 4: Sample sizes used in obtaining excess noise factors given the multiplication region size.**

Multiplication Region Size	Sample Size
0.125 $\mu\text{m}$	<b>42905</b>
0.25 $\mu\text{m}$	<b>55001</b>
0.50 $\mu\text{m}$	<b>44490</b>
1.0 $\mu\text{m}$	<b>27378</b>

The decrease in noise with thinner multiplication regions is not universally reported, however. Ma, et al [129] report that the excess noise factor decreases with increasing multiplication region thickness. The consensus, however, is in line with the results shown in Figure 52, and it is not immediately clear why the results of Ma, et al run contrary to this.

Finally, it is helpful to examine the excess noise factor results in the context of the standard deviation of the gain. The standard deviation v. mean gain is shown in Figure 53 as a function of the multiplication region size. Two observations are immediately made from the data. First, the standard deviation is always less than the mean, suggesting that the average deviations from the mean, the noise, is fairly stable. Second, it is clear that for any given gain, the standard deviation increases with multiplication region size. This follows and verifies the noise results in Figure 52.

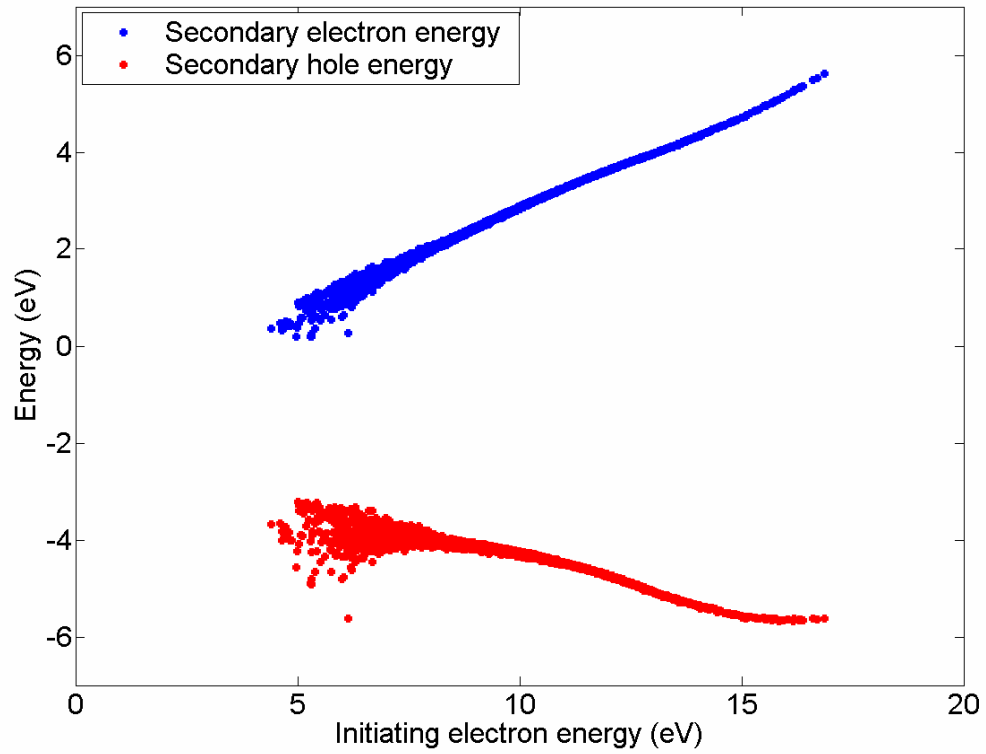


**Figure 41: Energies of secondary electron and hole created from impact ionization event as a function of the energy of the initiating electron in GaN-ZB.**

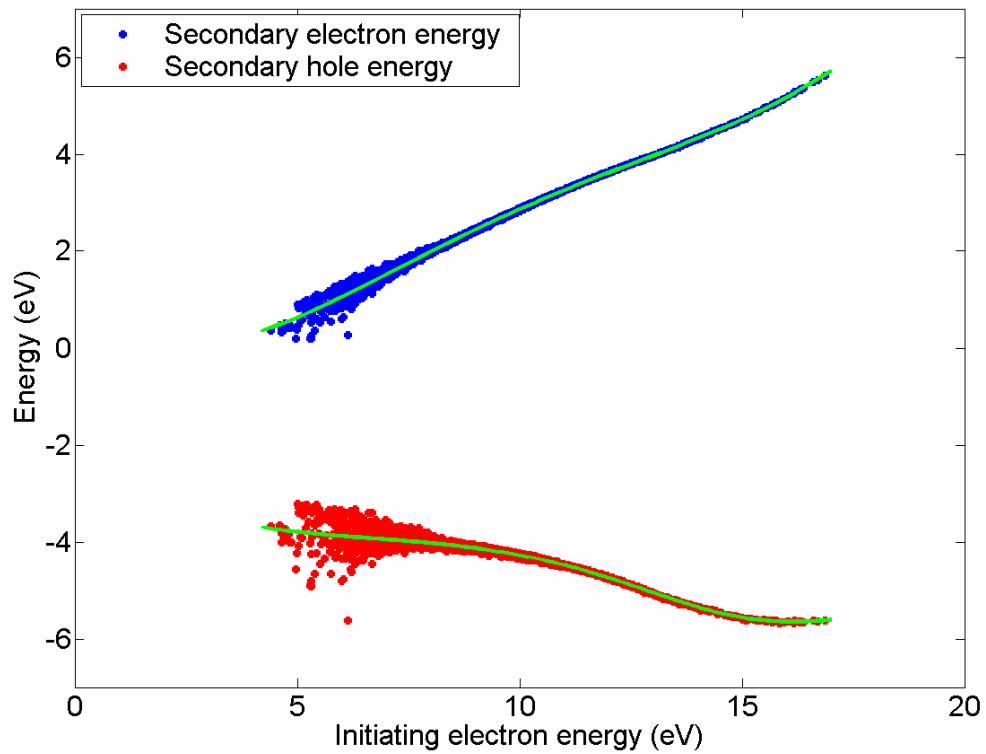


**Figure 42: Energies of secondary electron and hole created from impact ionization event as a function of the energy of the initiating electron with fitting functions included for comparison.**



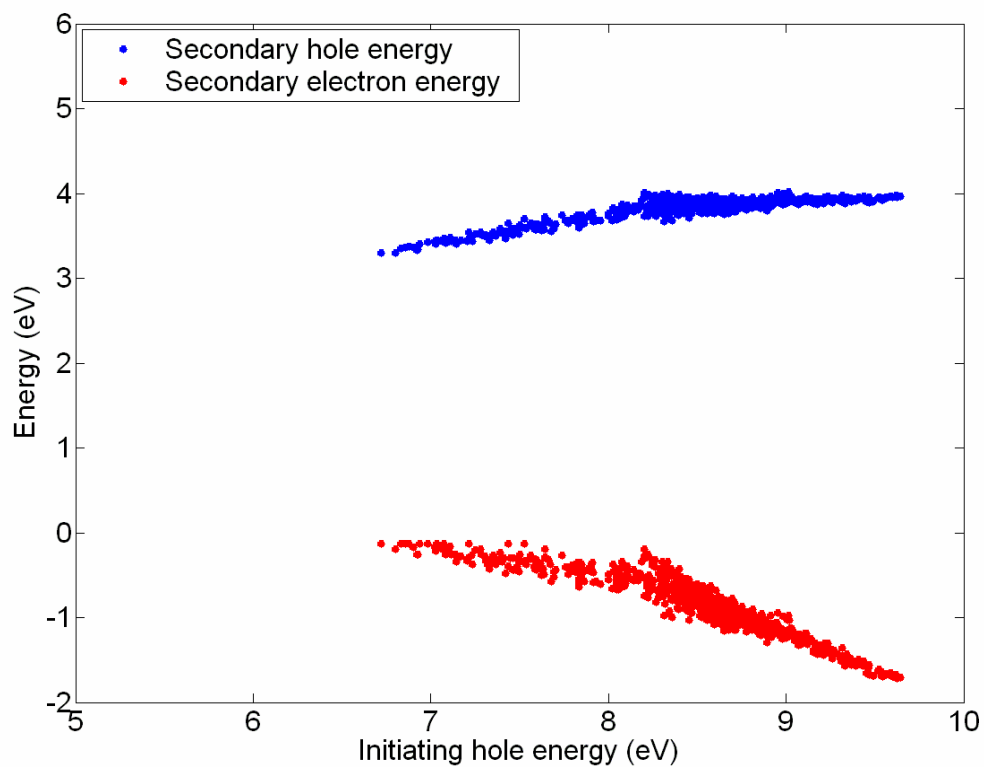


**Figure 43: Energies of secondary electron and hole created from impact ionization event as a function of the energy of the initiating hole in GaN-ZB.**

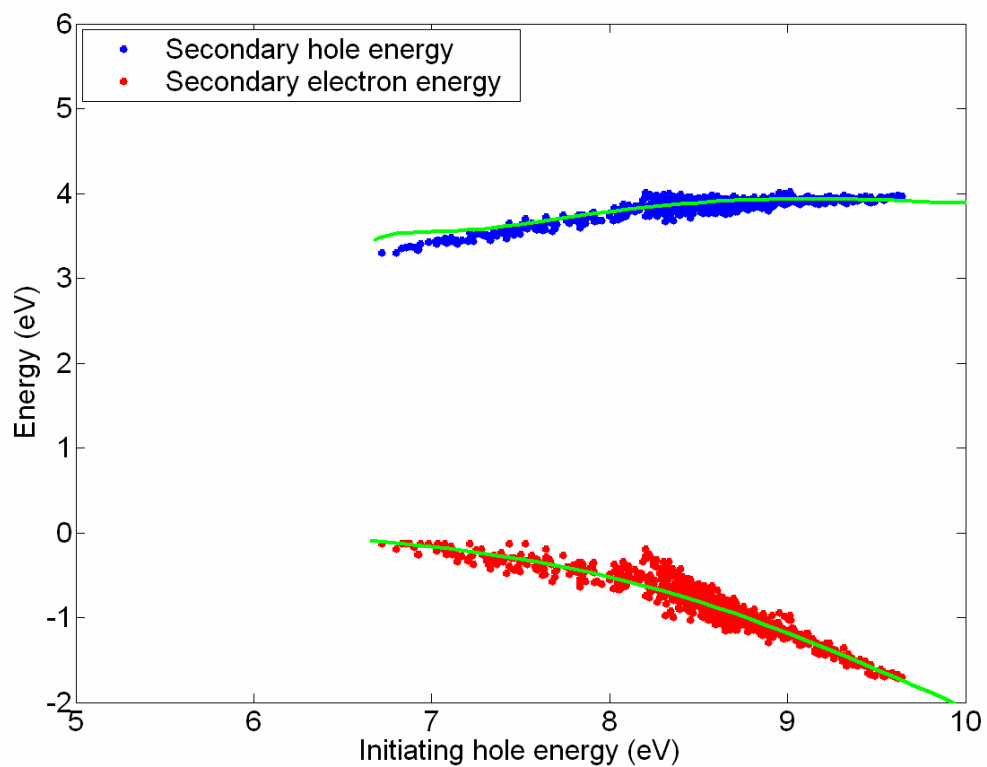


**Figure 44: Energies of secondary electron and hole created from impact ionization event as a function of the energy of the initiating hole with fitting functions included for comparison.**

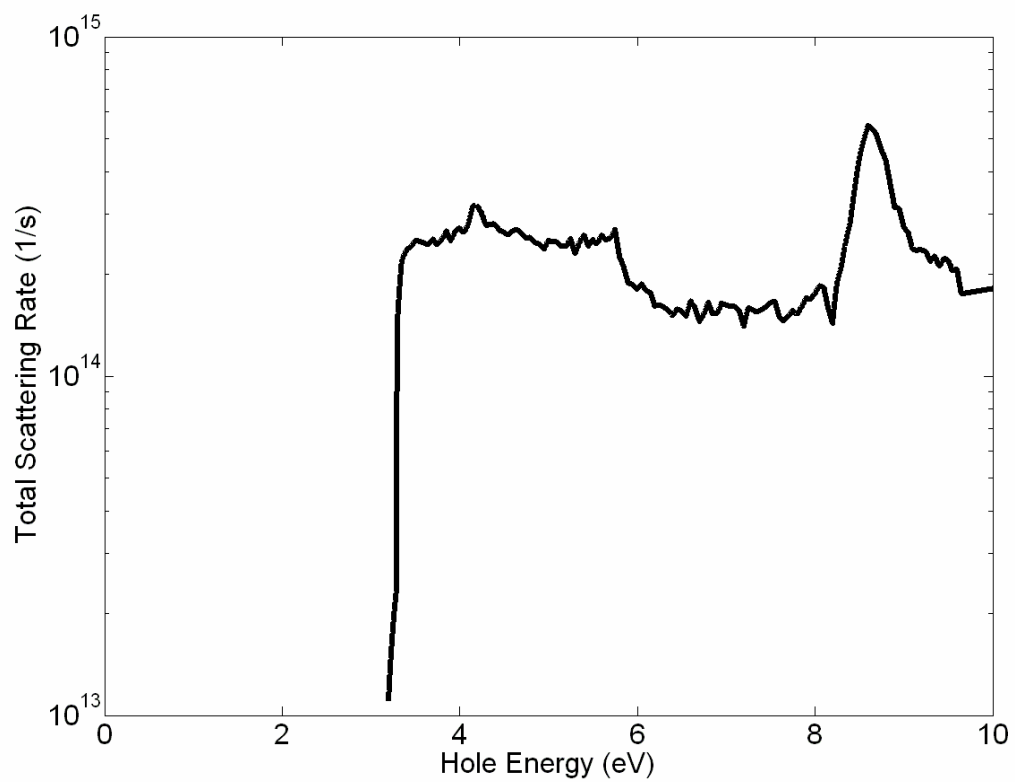


**Figure 45: Total energy-dependent hole scattering rate in GaN-ZB including impact ionization.**

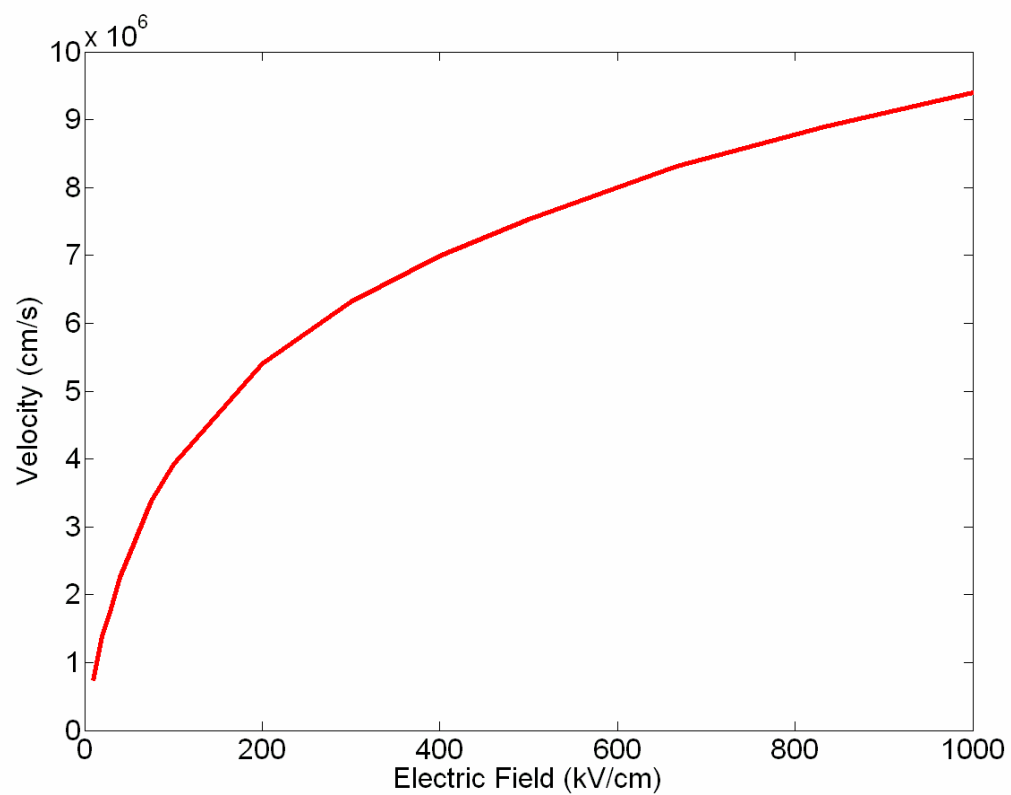


**Figure 46: Velocity v. electric field data for holes in GaN-ZB. The field range shown is the same as in [50] for comparison purposes.**

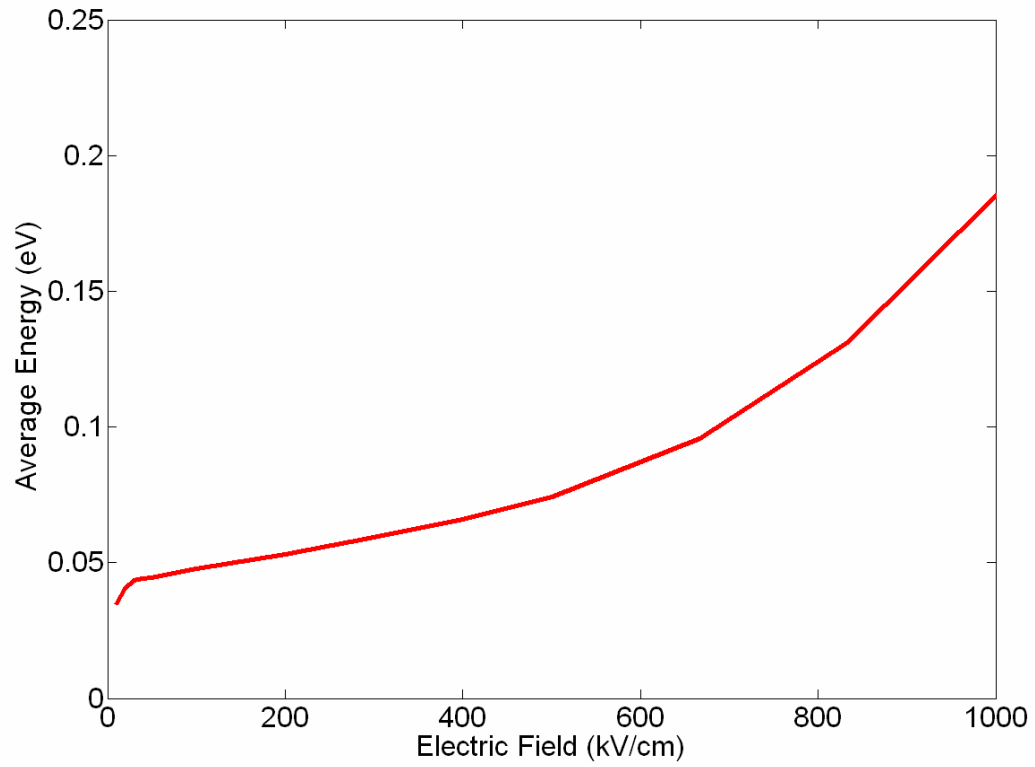


**Figure 47: Average carrier energy v. electric field data for holes in GaN-ZB. The field range shown is the same as in [50] for comparison purposes.**

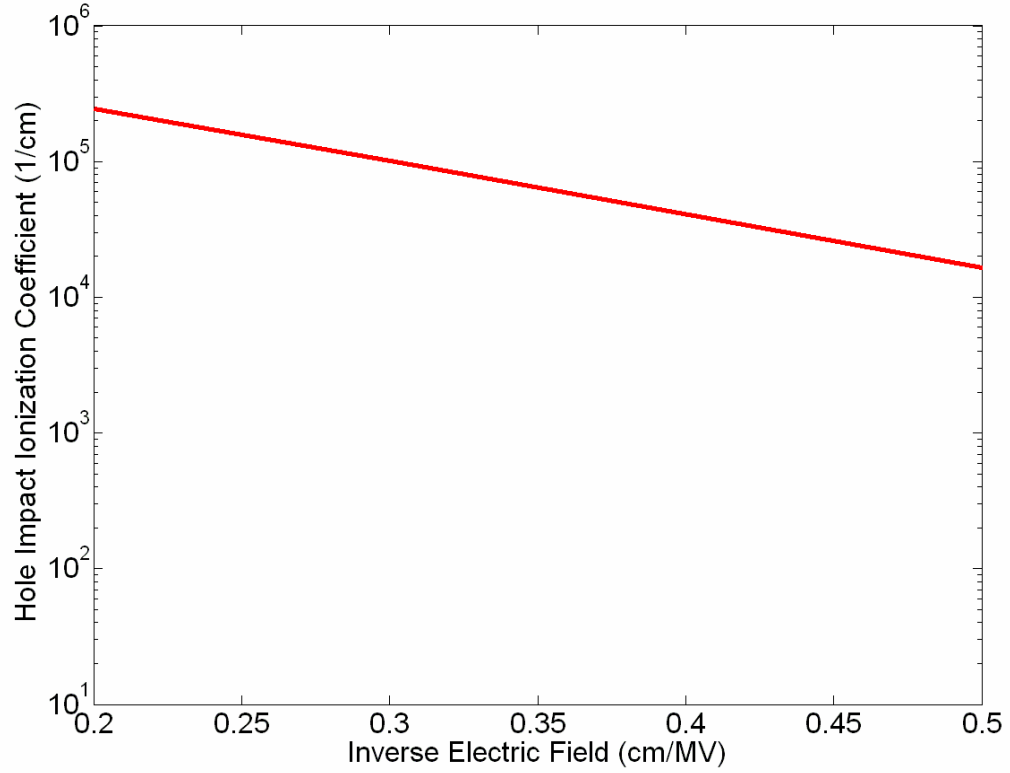


**Figure 48: Hole impact ionization coefficient v. the inverse of the applied electric field in GaN-ZB using the unipolar impact ionization final state selector. The field range shown is the same as in [50] for comparison purposes.**

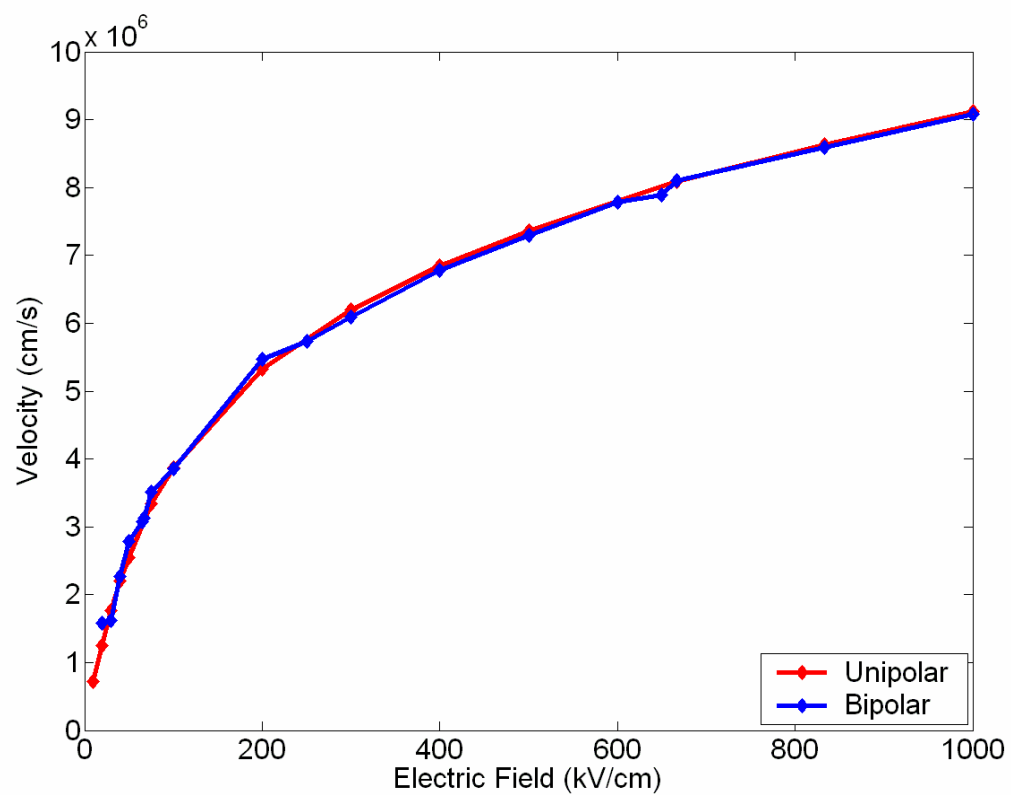


**Figure 49: Comparison of bipolar and unipolar low-field hole velocity in GaN-ZB.**

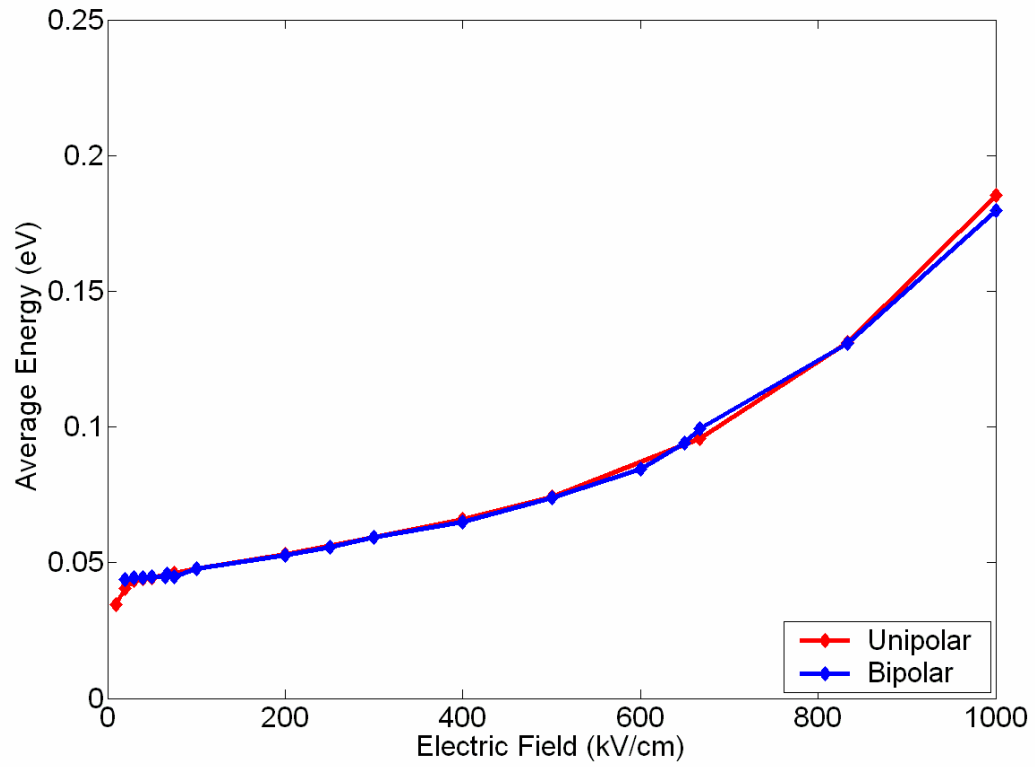


**Figure 50: Comparison of bipolar and unipolar low-field hole average carrier energy in GaN-ZB.**



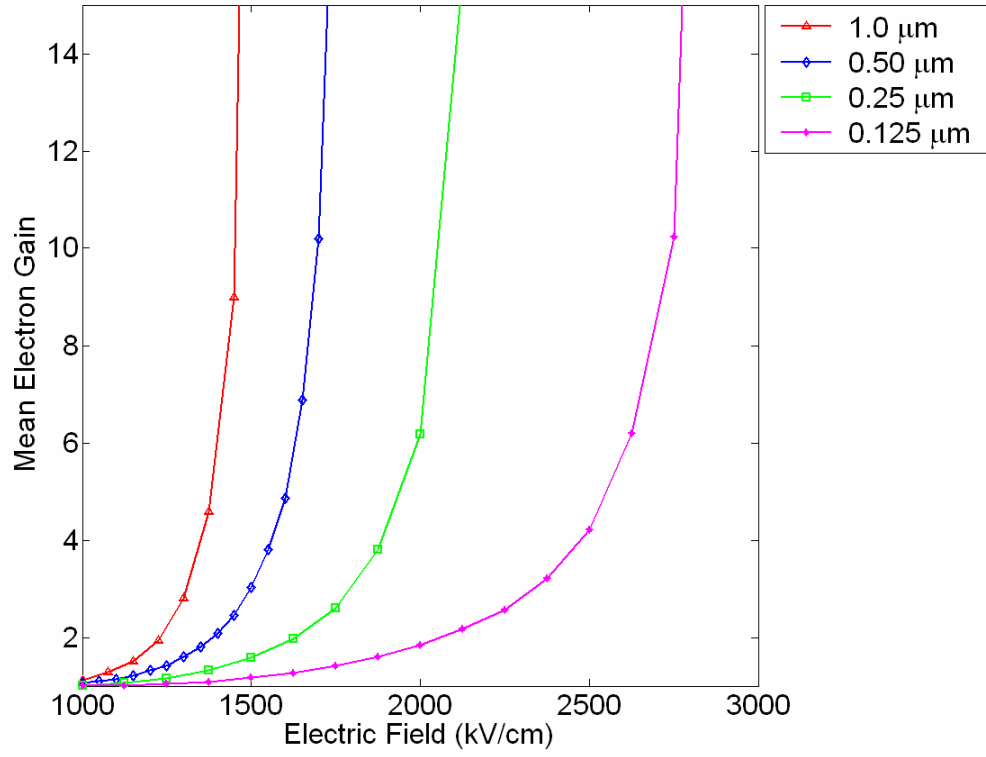


**Figure 51: Mean electron gain for single electron injection into GaN-ZB multiplication regions of 0.125, 0.25, 0.50, and 1.00  $\mu\text{m}$ .**

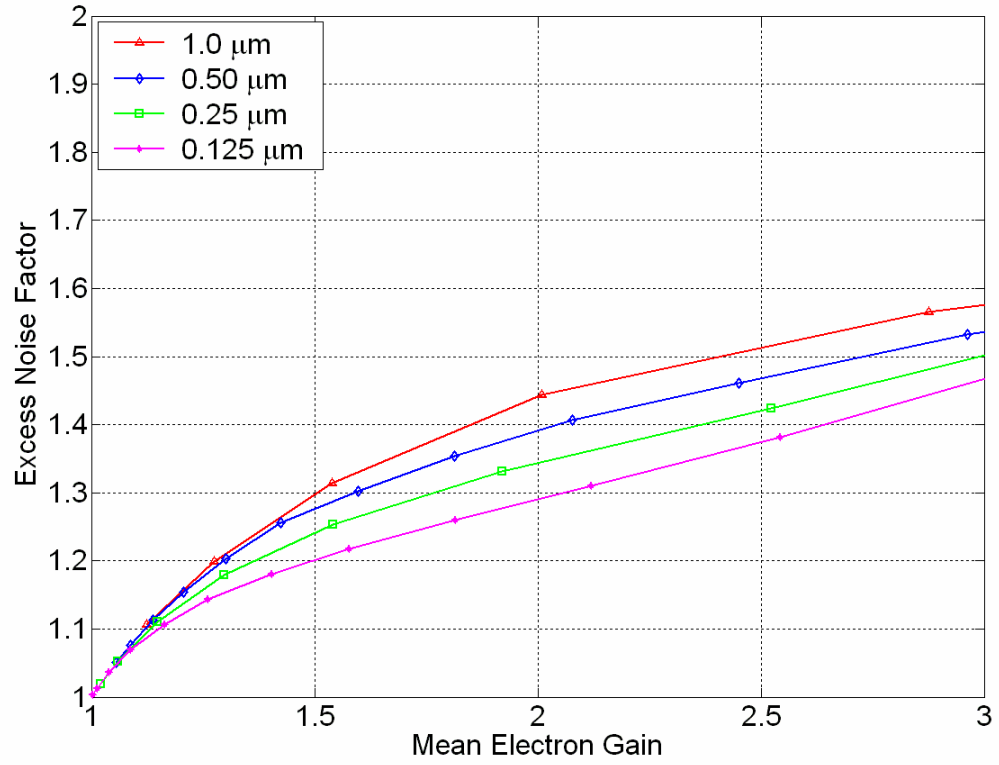


**Figure 52: Excess noise factor for single electron injection into GaN-ZB multiplication regions of 0.125, 0.25, 0.50, and 1.00  $\mu\text{m}$ .**

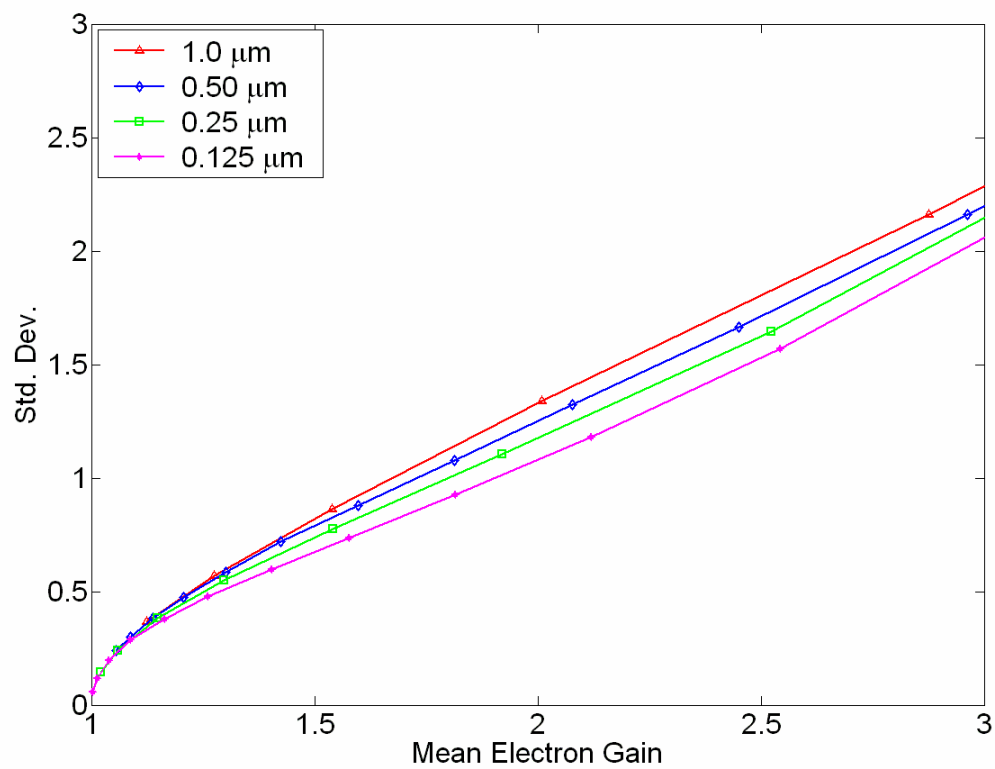


**Figure 53: Standard deviation of gain as a function of multiplication region size.**

## CHAPTER VIII

### 8.1 Summary of Results

Several goals have been achieved through the course of this work. The first accomplishment is the numerical calculation of the carrier-phonon scattering rates with an acknowledgement that arbitrary integration grid resolutions are unacceptable. A thorough convergence analysis provides a reasonable integration grid resolution while trading small amounts of accuracy with large gains in the computation time required. It was then possible to calculate both electron- and hole-phonon scattering rates for any of the zincblende wide band gap materials studied throughout the rest of the work.

After the scattering rates are reliably calculated, it is necessary to incorporate them into the numerical Monte Carlo simulator. This advanced simulator incorporates more completely numerical features in one simulator than have been used in past versions. The numerical scattering rates, along with the use of a numerical band structure, allow the implementation of the numerical final state selector, the biggest improvement. Analytical final-state selectors rely entirely on the state of the initiating carrier, with little regard for the inherent properties of the material or the electronic band structure. Advanced algorithm techniques also make it possible to incorporate the full wave vector overlaps in the selection of the final states.

The only user-adjustable parameters that remain in the simulator are the two acoustic deformation potentials. These values, which are incredibly difficult to calculate and not experimentally measurable, are generally assumed constant. These values can be selected, rather than using values published for use in other simulators, or calculated over very small regions of space, to make small modifications to the transport properties of the materials. In this way, it is possible to account for small band structure irregularities.

With the advanced Monte Carlo model and the new carrier-phonon scattering rates, it is then possible to examine electronic transport issues. Specifically, the question of temperature-dependent, high-field transport of wide band gap semiconductors is addressed. It is found that the controlling mechanism is the magnitude of the phonon energies. Materials with relatively large phonon energies exhibit smaller changes in the magnitudes of the carrier-phonon scattering rates than do materials with relatively small phonon energies. As a result, the transport properties of materials with large phonon energies are much less affected than the transport properties of materials with small phonon energies.

The last area of work addressed in this thesis is the extension of the single species Monte Carlo simulator to a bipolar simulator, where both electrons and holes are simulated simultaneously. In this way, it is possible to conduct future Monte Carlo analysis on devices that rely on both carrier species to dictate the device performance characteristics. To illustrate the utility of the bipolar model, the multiplication regions of avalanche photodiode are studied. The simulator produces gain and noise profiles for GaN-ZB APDs as a function of the multiplication region thickness.

The implementation of the bipolar, full-band simulator represents an enormous performance enhancement over existing bipolar simulators that rely on analytical energy bands and/or scattering rate formulations. This is particularly the case since these analytical bipolar simulators have been used to examine device performance at and into breakdown. In the breakdown regime of any material, analytical formulations of either energy bands or scattering mechanisms is questionable by its very nature. It is well known that parabolic or non-parabolic approximations of the energy band structure are valid only in the lowest energy valleys the approximations seek to represent. Assuming their validity at or near energies associated with breakdown is fundamentally flawed.

Analytically described scattering mechanisms are also flawed by their reliance on the analytical scattering mechanisms.

## **8.2 Recommendations for Future Work**

The Monte Carlo model that has been implemented in the course of this work is designed to rely on as few user-adjustable parameters as possible. Few Monte Carlo simulators incorporate as much physics, including a fully numerical description of both the electronic band structure and the carrier-phonon scattering rates, while requiring nearly no assistance from the user.

For different reasons, at different points along the way, however, some compromises are made. Some of the compromises are necessitated by the limits of computational horsepower available. Others are made as a reluctant acknowledgement that the numerical electronic band structure is not perfect throughout the entire irreducible wedge.

While a “perfectly” calculated electronic band structures may not be realistic under most circumstances, new technology will allow more instructions per cycle to be executed, and the advanced Monte Carlo simulator can be refined further. Other refinements are mandatory in order for the simulator to be used on the more complex semiconductors with wurtzite crystal symmetries.

To refine the model with respect to the electronic band structure, the primary improvement that can be made is the calculation of the wave-vector-dependent phonon dispersion. With the optical scattering mechanisms used now, the phonon energy is assumed constant, although it is not and varies as a function of the wave vector. The acoustic phonon energy is currently assumed to follow well-behaved function of the

wave vector magnitude. This approximation is adequate, particularly at long wave vectors. The inaccuracy at small wave vectors is tolerated because the acoustic phonon scattering mechanism is very weak at these wave vectors.

One of the primary ways of refining the interaction between the deviations from equilibrium of the crystal core ions and the charge carriers is to portray accurately the magnitude of the interactions by considering the wave vector of the carrier. The calculation of the phonon dispersion relations requires the use of a pseudo-rigid ion calculation. This calculation is nontrivial and time-consuming, but offers to provide fewer places for transport errors to hide.

With the wave vector-dependent phonon energies, a more accurate calculation of the scattering rates will be possible. While refining the integration mesh of the scattering rate calculations does not promise to offer significant improvement over the current parameters, it will be necessary to calculate the scattering rates at more query points. In particular, in order to study wurtzite crystals, the current energy-dependent scattering mechanism will not be reliable. The energy-dependent model was justified by the inherent symmetries of the zincblende crystal, in particular the symmetries offered in all three of the primary directions in wave vector space. Since there is less symmetry in wurtzite crystals, it is necessary to use wave vector-dependent scattering in the Monte Carlo simulator.

The challenge of using wave vector-dependent scattering is twofold. First, it will be necessary to calculate the scattering rates at a sufficient number of query points in an evenly spaced grid within the irreducible wedge. A natural grid spacing may be 0.02 in normalized units, as is done for the electronic band structure. It will then be necessary to devise an appropriate interpolation mechanism so that accurate scattering rates can be obtained between the grid points. It is expected that a linear interpolation mechanism

will provide sufficient accuracy, particularly in the critical low-energy regime where most mechanisms turn-on rather abruptly.

Simulating carrier transport in materials with the wurtzite crystal structure is inherently more data-intensive. The increase in the number of bands in the band structure has already been mentioned. Often, there are 12 conduction and eight valence bands, 2.5 times more bands than the eight used in zincblende crystals. While single species analysis may be manageable, the bipolar simulator will be hampered. Some considerations must be made in order to extend the simulator to the study of wurtzite crystal materials. Perhaps the simplest solution, an increase in the amount of physical memory available, will prove to be sufficient.

Finally, the work on the APD multiplication regions has only scratched the surface on possible configurations to examine. The first possible arrangement to investigate is the gain and noise profiles, given injection of carriers at energies greater than zero. Since carriers not photogenerated in the multiplication region drift there under the influence of an applied electric field, it is reasonable to assume that their energies are nonzero. Nonzero injection energies will effectively decrease the size of the initial dead space. Subsequent dead spaces will still be a function of the electric field and the material, however. It is unclear what the effect of nonzero injection energies will be on the gain and noise profiles.

The second interesting application of the APD simulator are the gain and noise profiles of hole injection. It is expected that hole injection would effectively shift the gain profiles to higher electric fields, for a given multiplication region thickness. This is due to the lower hole mobility and slightly lower impact ionization coefficients, although it is not clear what hole injection would imply about the noise profiles.



# APPENDIX I

## Derivation of Impact Ionization Matrix Element

Before attempting to assemble (21) with the different possible spin configurations, it is useful to first examine the definitions made in (16) and (20). To recall,

$$|n_1 k_1 \sigma_1; n_2 k_2 \sigma_2\rangle_A \equiv \frac{1}{\sqrt{2}} \left[ \begin{aligned} &\psi_{n_1 k_1}(\vec{r}_1) \psi_{n_2 k_2}(\vec{r}_2) \sigma_1(s_1) \sigma_2(s_2) \\ &- \psi_{n_1 k_1}(\vec{r}_2) \psi_{n_2 k_2}(\vec{r}_1) \sigma_1(s_2) \sigma_2(s_1) \end{aligned} \right] \quad (36)$$

Then with this definition, by simply swapping the order of the states:

$$|n_2 k_2 \sigma_2; n_1 k_1 \sigma_1\rangle_A \equiv \frac{1}{\sqrt{2}} \left[ \begin{aligned} &\psi_{n_2 k_2}(\vec{r}_1) \psi_{n_1 k_1}(\vec{r}_2) \sigma_2(s_1) \sigma_1(s_2) \\ &- \psi_{n_2 k_2}(\vec{r}_2) \psi_{n_1 k_1}(\vec{r}_1) \sigma_2(s_2) \sigma_1(s_1) \end{aligned} \right] \quad (37)$$

By superposition, it is possible to swap the order of the terms in each product.

This yields:

$$|n_2 k_2 \sigma_2; n_1 k_1 \sigma_1\rangle_A \equiv \frac{1}{\sqrt{2}} \left[ \begin{aligned} &\psi_{n_1 k_1}(\vec{r}_2) \psi_{n_2 k_2}(\vec{r}_1) \sigma_1(s_2) \sigma_2(s_1) \\ &- \psi_{n_1 k_1}(\vec{r}_1) \psi_{n_2 k_2}(\vec{r}_2) \sigma_1(s_1) \sigma_2(s_2) \end{aligned} \right] \quad (38)$$

The equations of (37) and (38) are the same, but these are not equivalent to (36).

One final manipulation is made to (38) – the order of the products is swapped:

$$|n_2 k_2 \sigma_2; n_1 k_1 \sigma_1\rangle_A \equiv \frac{-1}{\sqrt{2}} \left[ \begin{aligned} &\psi_{n_1 k_1}(\vec{r}_1) \psi_{n_2 k_2}(\vec{r}_2) \sigma_1(s_1) \sigma_2(s_2) \\ &- \psi_{n_1 k_1}(\vec{r}_2) \psi_{n_2 k_2}(\vec{r}_1) \sigma_1(s_2) \sigma_2(s_1) \end{aligned} \right] \quad (39)$$

The right-hand-side of (39) is a factor of (36), in other words:

$$|n_2 k_2 \sigma_2; n_1 k_1 \sigma_1\rangle_A = -(|n_1 k_1 \sigma_1; n_2 k_2 \sigma_2\rangle_A) \quad (40)$$

By (40), (20) can be written:

$$\begin{aligned} M_1 &= \langle 34 | V_{cc} | 12 \rangle = -\langle 34 | V_{cc} | 21 \rangle \\ M_2 &= \langle 43 | V_{cc} | 12 \rangle = -\langle 43 | V_{cc} | 21 \rangle \end{aligned} \quad (41)$$

Now it is possible to obtain (21) from the possible spin combinations and (19).

As Bude states [94], the squares of the matrix elements corresponding to the spin configurations along with (41) can be written in terms of  $M_1$  and  $M_2$  to obtain:

1.  $|M_1 - M_2|^2$
2.  $|M_1|^2$
3.  $|M_2|^2$

Using (19), the different spin possibilities are examined. To begin, it is assumed that  $\sigma_1 = \sigma_2 = \sigma_3 = \sigma_4$ . In this case, the delta functions in (19) are equal to one, and:

$$M(12;34) = \frac{1}{2} [\langle 34 | V_{cc} | 12 \rangle - \langle 43 | V_{cc} | 12 \rangle - \langle 34 | V_{cc} | 21 \rangle + \langle 43 | V_{cc} | 21 \rangle] \quad (42)$$

From (41), (42) is written:

$$M(12;34) = \frac{1}{2} [\langle 34 | V_{cc} | 12 \rangle - \langle 43 | V_{cc} | 12 \rangle + \langle 34 | V_{cc} | 12 \rangle - \langle 43 | V_{cc} | 12 \rangle] \quad (43)$$

$$M(12;34) = \frac{1}{2} [2 \langle 34 | V_{cc} | 12 \rangle - 2 \langle 43 | V_{cc} | 12 \rangle] \quad (44)$$

$$M(12;34) = [\langle 34 | V_{cc} | 12 \rangle - \langle 43 | V_{cc} | 12 \rangle] \quad (45)$$

$$M(12;34) = [M_1 - M_2] \quad (46)$$

Squaring the result in (46) gives the first item in the list on page 137. The next set of possible spin considerations is  $\sigma_1 \neq \sigma_2$ :  $\sigma_1 = \sigma_3$ ,  $\sigma_2 = \sigma_4$ . In this case, (19) becomes:

$$M(12;34) = \frac{1}{2} [\langle 34 | V_{cc} | 12 \rangle - 0 - 0 + \langle 43 | V_{cc} | 21 \rangle] \quad (47)$$

It is possible to write:

$$\langle n_1 k_1 \sigma_1; n_2 k_2 \sigma_2 | \equiv \frac{1}{\sqrt{2}} \left[ \begin{aligned} &\psi_{n_1 k_1}^* (\vec{r}_1) \psi_{n_2 k_2}^* (\vec{r}_2) \sigma_1(s_1) \sigma_2(s_2) \\ &- \psi_{n_1 k_1}^* (\vec{r}_2) \psi_{n_2 k_2}^* (\vec{r}_1) \sigma_1(s_2) \sigma_2(s_1) \end{aligned} \right] \quad (48)$$

The manipulation is done in a way such that results similar to (41) can be obtained [115], given a slightly different spin configuration. In this case, the following is found:

$$\begin{aligned} M_1 &= \langle 34 | V_{cc} | 12 \rangle = -\langle 43 | V_{cc} | 12 \rangle = -M_2 \\ M_2 &= \langle 43 | V_{cc} | 12 \rangle = -\langle 34 | V_{cc} | 12 \rangle = -M_1 \end{aligned} \quad (49)$$

Then (47) is rewritten:

$$M(12;34) = \frac{1}{2} [M_1 + (-M_2)] \quad (50)$$

Or:

$$M(12;34) = \frac{1}{2} [M_1 + (-(-M_1))] \quad (51)$$

$$M(12;34) = \frac{1}{2} [M_1 + M_1] \quad (52)$$

$$M(12;34) = M_1 \quad (53)$$

Thus, (53) is true when the second possible set of spin configurations is considered. Squaring this result, of course, provides the second numbered item on page 137.

The final spin configuration to consider is  $\sigma_1 \neq \sigma_2$ :  $\sigma_1 = \sigma_4$ ,  $\sigma_2 = \sigma_3$ . In this case:

$$M(12;34) = \frac{1}{2} [0 - M_2 - (-M_1) + 0] \quad (54)$$

And then again by (49),

$$M(12;34) = -M_2 \quad (55)$$

By squaring the matrix elements of (46), (53), and (55), the probabilities of the numbered list on page 137 are recovered. One final step is required to obtain the total matrix element, (21). Bude notes that the sum of the probabilities gives the square of the total effective matrix element,  $M_{tot}^2$ , summed over all internal spins for a given initial spin. Therefore:

$$M_{tot}^2 = |M_1|^2 + |M_2|^2 + |M_1 - M_2|^2 \quad (56)$$

This can be simplified slightly further by expanding the last term. The matrix elements are composed of real and imaginary parts; therefore the following is the result of multiplying the last term and writing each term:

$$|M_1 - M_2|^2 = (M_{1,R}^2 + M_{1,I}^2) + (M_{2,R}^2 + M_{2,I}^2) - 2(M_{1,R} M_{2,R} + M_{1,I} M_{2,I}) \quad (57)$$

The  $,R$  and  $,I$  represent the real and imaginary parts of  $M$  in (57), respectively. Since  $M$  has imaginary parts, the first two terms in (57) are easily recognized to simplify to:

$$|M_1 - M_2|^2 = |M_1|^2 + |M_2|^2 - 2(M_{1,R} M_{2,R} + M_{1,I} M_{2,I}) \quad (58)$$

It will now be shown that

$$(M_{1,R} M_{2,R} + M_{1,I} M_{2,I}) = \frac{1}{2} (M_1^* M_2 + M_2^* M_1) \quad (59)$$

Both terms on the right-hand-side of (59) will be expanded and then summed:

$$M_1^* M_2 = M_{1,R} M_{2,R} + i (M_{2,I} M_{1,R} - M_{1,I} M_{2,R}) + M_{1,I} M_{2,I} \quad (60)$$

And,

$$M_2^* M_1 = M_{1,R} M_{2,R} - i (M_{2,I} M_{1,R} - M_{1,I} M_{2,R}) + M_{1,I} M_{2,I} \quad (61)$$

Summing (60) and (61) yields:

$$M_1^* M_2 + M_2^* M_1 = 2 \left( M_{1,R} M_{2,R} + M_{1,I} M_{2,I} \right) \quad (62)$$

The equation in (62) is (59), therefore (58) becomes:

$$|M_1 - M_2|^2 = |M_1|^2 + |M_2|^2 - \left( M_1^* M_2 + M_2^* M_1 \right) \quad (63)$$

Finally, the last term in (56) is replaced with (63) to yield:

$$M_{tot}^2 = |M_1|^2 + |M_2|^2 + \left( |M_1|^2 + |M_2|^2 - \left( M_1^* M_2 + M_2^* M_1 \right) \right) \quad (64)$$

$$M_{tot}^2 = 2|M_1|^2 + 2|M_2|^2 + \left( M_1^* M_2 + M_2^* M_1 \right) \quad (65)$$

Therefore, (21) on page 56 is recovered. This matrix element is used in the calculations of the impact ionization transition rates for both electrons and holes in all of the work in this thesis.

## REFERENCES

- [1] M. Bhatnagar and B. J. Baligla, "Comparison of 6H-SiC, 3C-SiC, and Si for power devices," *IEEE Transactions on Electron Devices*, **40** (3), p. 645-55, March 1993.
- [2] C. E. Weitzel, J. W. Palmour, C. H. Carter, Jr., K. Moore, K. J. Nordquist, S. Allen, C. Thero, and M. Bhatnagar, "Silicon carbide high-power devices," *IEEE Transactions on Electron Devices*, **43** (10), p. 1732-41, October 1996.
- [3] J. A. Cooper, "Advances in SiC MOS technology," in *Physica Status Solidi (a), Special Review Issue on Silicon Carbide Technology*, J. Choyke, W. Pensl, and H. Matsunami, Eds., **162** (1), p. 305-20, July 1997.
- [4] A. Elasser and T. P. Chow, "Silicon carbide benefits and advantages for power electronics circuits and systems," *Proceedings of the IEEE*, **90** (6), p. 969-86, June 2002.
- [5] S. N. Mohammad, A. A. Salvador, and H. Morkoç, "Emerging gallium nitride-based devices," *Proceedings of the IEEE*, **83** (10), p. 1306-55, October 1995.
- [6] G. L. Harris, Ed., *Properties of Group III-Nitrides*, London: INSPEC, 1994.
- [7] G. L. Harris, Ed., *Properties of Silicon Carbide*, London: INSPEC, 1996.
- [8] C. Nguyen, and M. Micovic, "The state-of-the-art of GaAs and InP power devices and amplifiers," *IEEE Transactions on Electron Devices*, **48** (3), p. 472-8, March 2001.
- [9] S. Adachi, "GaAs, AlAs and  $\text{Al}_x\text{Ga}_{1-x}\text{As}$ : Material parameters for use in research and device applications," *Journal of Applied Physics*, **58** (3), p. R1-29, 1 August 1985.
- [10] M. A. Green, Solar Cells: Operating Principles. Technology and System Applications. Englewood Cliffs, NJ: Prentice-Hall, Inc., 1982.
- [11] J. G. Ruch and G. S. Kino, "Transport properties of GaAs," *Physical Review*, **174** (3), p. 921-31, 15 October 1968.

- [12] S. Zollner, S. Gopalan, and M. Cardona, "Microscopic theory of intervalley scattering in GaAs:  $k$ -dependence of deformation potentials and scattering rates," *Journal of Applied Physics*, **68** (4), p. 1682-93, 15 August 1990.
- [13] K. T. Tsen, R. Joshi, and H. Morkoç, "Direct measurements of electron-optical photon scattering rates in ultrathin GaAs-AlAs multiple quantum well structures," *Applied Physics Letters*, **62** (17), p. 2075-7, 26 April 1993.
- [14] M. Stobbe, R. Redmer, and W. Schattke, "Impact ionization rate in GaAs," *Physical Review B*, **49** (7), p. 4494-500, 15 February 1994-I.
- [15] P. Damayanthi, R. P. Joshi, and J. A. McAdoo, "Calculations of hole transport characteristics in bulk GaSb with comparisons to GaAs," *Journal of Applied Physics*, **88** (2), p. 817-21, 15 July 2000.
- [16] G. Theodorou, G. Tsegas, and E. Kaxiras, "Theory of electronic and optical properties of 3C-SiC," *Journal of Applied Physics*, **85** (4), p. 2179-84, 15 February 1999.
- [17] C. E. Weitzel, "Comparison of SiC, GaAs and Si RF MESFET power devices," *IEEE Electron Device Letters*, **16** (10), p. 451-3, October 1995.
- [18] K. Bhaumik, B. K. Ridley, and Y. Shacham-Diamand, "Hole-phonon scattering in strained SiGe quantum wells," *Journal of Applied Physics*, **74** (9), p. 5546-58, 1 November 1993.
- [19] S. Nakamura, "InGaN/AlGaIn blue-light-emitting diodes," *Journal of Vacuum Science & Technology A*, **13** (3), p. 705-10, May/June 1995.
- [20] S. Nakamura, M. Senoh, N. Iwasa, and S. I. Nagahama, "High-power InGaIn single quantum well structure blue and violet light emitting diodes," *Applied Physics Letters*, **67** (13), p. 1868-70, 25 September 1995.
- [21] A. W. Smith and K. F. Brennan, "Hydrodynamic simulation of semiconductor devices," *Progress in Quantum Electronics*, **21** (4), p. 293-360, 1998.

- [22] M. V. Fischetti and S. E. Laux, "Monte Carlo analysis of electron transport in small semiconductor devices including band-structure and space-charge effects," *Physical Review B*, **38** (14), p. 9721-45, 15 November 1988-I.
- [23] M. V. Fischetti and S. E. Laux, "Monte Carlo simulation of transport in technologically significant semiconductors of the diamond and zinc-blende structures – Part II: Submicrometer MOSFETs," *IEEE Transactions on Electron Devices*, **38** (3), p. 650-60, March 1991.
- [24] M. V. Fischetti, "Monte Carlo simulation of transport in technologically significant semiconductors of the diamond and zinc-blende structures – Part I: Homogeneous transport," *IEEE Transactions on Electron Devices*, **38** (3), p. 634-49, March 1991.
- [25] J. Y. Tang and K. Hess, "Impact ionization of electrons in silicon," *Journal of Applied Physics*, **54** (9), p. 5139-44, September 1983.
- [26] J. Y. Tang and K. Hess, "Theory of hot electron emission from silicon into silicon dioxide," *Journal of Applied Physics*, **54** (9), p. 5145-51, September 1983.
- [27] K. Brennan, K. Hess, J. Y. Tang, and G. J. Iafrate, "Transient electronic transport in InP under the conditions of high-field electron injection," *IEEE Transactions on Electron Devices*, **ED-30** (12), p. 1750-4, December 1983.
- [28] E. Bellotti, K. F. Brennan, R. Wang, and P. P. Ruden, "Monte Carlo study of electron initiated impact ionization in bulk zincblende and wurtzite phase ZnS," *Journal of Applied Physics*, **83** (9), p. 4765-72, 1 May 1998.
- [29] E. Bellotti, H-E Nilsson, K. F. Brennan, P. P. Ruden, and R. Trew, "Monte Carlo calculation of hole initiated impact ionization in 4H phase SiC," *Journal of Applied Physics*, **87** (8), p. 3864-71, 15 April 2000.



- [30] H-E Nilsson, E. Bellotti, M. Hjelm, and K. Brennan, "A comparison between different Monte Carlo models in simulation of hole transport in 4H-SiC," *Mathematics and Computers in Simulation*, **55**, p. 199-208, 2001.
- [31] C. Jacoboni and P. Lugli, The Monte Carlo Method for Semiconductor Device Simulation. Vienna: Springer-Verlag, 1989.
- [32] K. F. Brennan, E. Bellotti, M. Farhamand, J. Haralson II, P. P. Ruden, J. D. Albrecht, and A. Sutandi, "Material theory based modeling of wide band gap semiconductors: from basic to property devices," *Solid State Electronics*, **44** (2), p. 195-204, February 2000.
- [33] H. Kosina, "Theory of the Monte Carlo method for semiconductor device simulation," *IEEE Transactions on Electron Devices*, **47** (10), p. 1898-908, October 2000.
- [34] N. Cavassilas, F. Aniel, G. Fishman, and R. Adde, "Full-band matrix solution of the Boltzmann transport equation and electron impact ionization in GaAs," *Solid-State Electronics*, **46**, p. 559-66, 2002.
- [35] E. Gnani, S. Reggiani, M. Rudan, "Full-band transport properties of silicon dioxide using the spherical-harmonics expansion of the BTE," *Physica B*, **314**, p. 193-7, 2002.
- [36] N. Goldsman, Y.-J. Wu, and J. Frey, "Efficient calculation of ionization coefficients in silicon from the energy distribution function," *Journal of Applied Physics*, **68** (3), p. 1075-81, 1 August 1990.
- [37] K. F. Brennan, J. Kolník, I. H. Oğuzman, E. Bellotti, M. Farhamand, P. P. Ruden, R. Wang, and J. D. Albrecht, "Materials Theory Based Modeling of GaN Devices," in GaN and Related Materials III-Volume 7, S. J. Pearton, Ed., Amsterdam: Gordon and Breach, pp. 305-59.
- [38] M. Goano, E. Bellotti, K. F. Brennan, and G. Ghione, "Material theory based modeling of GaN and other III-Nitrides," presented at 11<sup>th</sup> III-V Semiconductor Device Simulation Workshop, IEMN Villeneuve d'Ascq, 1999.

- [39] E. Bellotti and K. F. Brennan, "Physics and transport properties of SiC polytypes," presented at Euroconference on Advanced Heterostructure Devices for Micro and Optoelectronics III, Villa Gualino, Torino, Italy, 1998.
- [40] E. Ghillino, C. Garetto, M. Goano, G. Ghione, E. Bellotti, and K. F. Brennan, "Simplex algorithm for band structure calculation of noncubic symmetry semiconductors: application to III-nitride binaries and alloys," *VLSI Design*, **13** (1-4), p. 63-8, 2001.
- [41] H-E Nilsson, U. Englund and M. Hjelm, "Full-Band Monte Carlo Simulation of Electron Transport in 3C-SiC," *Materials Science Forum*, **389-393**, p. 537-40, 2002.
- [42] M. L. Cohen and T. K. Bergstresser, "Band structure and pseudo-potential form factors for fourteen semiconductors of the diamond and zincblende structures," *Physical Review*, **141** (2), p. 789-96, January 1966.
- [43] M. L. Cohen and J. R. Chelikowsky, Electronic Structure and Optical Properties of Semiconductors. Berlin: Springer, 1988.
- [44] M. Goano, E. Bellotti, E. Ghillino, G. Ghione and K. F. Brennan, "Band structure nonlocal pseudopotential calculation of the III-nitride wurtzite phase materials system. Part I. Binary compounds GaN, AlN, and InN," *Journal of Applied Physics*, **88** (11), p. 6467-75, 1 December 2000.
- [45] M. Goano, E. Bellotti, E. Ghillino, C. Garetto, G. Ghione and K. F. Brennan, "Band structure nonlocal pseudopotential calculation of the III-nitride wurtzite phase materials system. Part II. Ternary alloys  $\text{Al}_x\text{Ga}_{1-x}\text{N}$ ,  $\text{In}_x\text{Ga}_{1-x}\text{N}$ , and  $\text{In}_x\text{Al}_{1-x}\text{N}$ ," *Journal of Applied Physics*, **88** (11), p. 6476-82, 1 December 2000.
- [46] C. Persson and U. Lindefelt, "Relativistic band structure calculation of cubic and hexagonal SiC polytypes," *Journal of Applied Physics*, **82** (11), p. 5496-508, 1 December 1997.

- [47] S. K. O’Leary, B. E. Foutz, M. S. Shur, L. F. Eastman, “Polar optical phonon instability and intervalley transfer in III-V semiconductors,” *Solid State Communications*, **118** (2), p. 79-83, 3 April 2001.
- [48] W. Fawcett, A. D. Boardman, and S. Swain, “Monte Carlo determination of electron transport properties of gallium arsenide,” *Journal of Physics and Chemistry of Solids*, **31**, p. 1963-90, 1970.
- [49] H-E Nilsson, U. Sannemo, and C. S. Petersson, “Monte Carlo simulation of electron transport in 4H-SiC using a two-band model with multiple minima,” *Journal of Applied Physics*, **80** (6), p. 3365-9, 15 September 1996.
- [50] I. H. Oğuzman, E. Bellotti, K. F. Brennan, J. Kolník, R. Wang, and P. P. Ruden, “Theory of hole initiated impact ionization in bulk zincblende and wurtzite GaN,” *Journal of Applied Physics*, **81** (12), p. 7827-34, 15 June 1997.
- [51] H-E Nilsson, A. Martinez, E. Ghillino, U. Sannemo, E. Bellotti, and M. Goano, “Numerical modeling of hole interband tunneling in wurtzite GaN and SiC,” *Journal of Applied Physics*, **90** (6), p. 2847-52, 15 September 2001.
- [52] K. A. Mäder and A. Zunger, “Empirical atomic pseudopotentials for AlAs/GaAs superlattices, alloys, and nanostructures,” *Physical Review B*, **50** (23), p. 17393-405, 15 December 1994-I.
- [53] S. L. Chuang and C. S. Chang, “**k•p** method for strained wurtzite semiconductors,” *Physical Review B*, **54** (4), p. 2491-504, 15 July 1996-II.
- [54] H-E Nilsson, E. Bellotti, K. F. Brennan and M. Hjelm, “A full-band Monte Carlo study of high field carrier transport in 4H-SiC,” *Materials Science Forum*, **338-342**, p. 765-8, 2000.

- [55] H-E Nilsson, A. Martinez, U. Sannemo, M. Hjelm, E. Bellotti, and K. Brennan, "Monte Carlo simulation of high field hole transport in 4H-SiC including band to band tunneling and optical interband transitions," *Physica B*, **314**, p. 68-71, 2002.
- [56] K. F. Brennan, The Physics of Semiconductors. Cambridge, MA: Cambridge University Press, 1999.
- [57] B. K. Ridley, Quantum Processes in Semiconductors, 3<sup>rd</sup> Edition. Oxford: Oxford University Press, 1993.
- [58] L. Tirino, M. Weber, K. F. Brennan, and E. Bellotti, "A general Monte Carlo model including the effect of the acoustic deformation potential on the transport properties," submitted to *Journal of Computational Electronics*, August 2002.
- [59] K. F. Brennan and N. S. Mansour, "Monte Carlo calculation of electron impact ionization in bulk InAs and HgCdTe," *Journal of Applied Physics*, **69** (11), p. 7844-7, 1 June 1991.
- [60] G. E. Bulman, V. M. Robbins, K. F. Brennan, K. Hess and G. E. Stillman, "Experimental determination of impact ionization coefficients in (100) GaAs," *IEEE Electron Device Letters*, **EDL-4** (6), p. 181-5, June 1983.
- [61] X. G. Zheng, P. Yuan, X. Sun, G. S. Kinsey, A. L. Holmes, B. G. Streetman, and J. C. Campbell, "Temperature dependence of the ionization coefficients of  $\text{Al}_x\text{Ga}_{1-x}\text{As}$ ," *IEEE Journal of Quantum Electronics*, **36** (10), p. 1168-73, October 2000.
- [62] F. Capasso, in Semiconductors and Semimetals, **22**, Part D, R. K. Willardson and A. C. Beer, Eds., New York: Academic, 1985.
- [63] C. A. Armiento and S. H. Groves, "Impact ionization in (100)-, (110)-, and (111)-oriented InP avalanche photodiodes," *Applied Physics Letters*, **43** (2), p. 198-200, 15 July 1983.

- [64] N. Tabatabaie, V. M. Robbins, N. Pan, and G. E. Stillman, "Impact ionization coefficients in (111) InP," *Applied Physics Letters*, **46** (2), p. 182-4, 15 January 1985.
- [65] C. R. Crowell and S. M. Sze, "Temperature dependence of avalanche multiplication in semiconductors," *Applied Physics Letters*, **9** (6), p. 242-4, 1966.
- [66] B. K. Ridley, "Lucky-drift mechanism for impact ionisation in semiconductors," *Journal of Physics C: Solid-State Physics*, **16**, p. 3373-88, 20 June 1983.
- [67] H. Shichijo and K. Hess, "Band-structure-dependent transport and impact ionization in GaAs," *Physical Review B*, **23** (8), p. 4197-207, 15 April 1981.
- [68] R. J. McIntyre, "A new look at impact ionization – Part I: A theory of gain, noise, breakdown probability, and frequency response," *IEEE Transactions on Electron Devices*, **46** (8), p. 1623-31, August 1999.
- [69] B. K. Ng, J. P. R. David, S. A. Plimmer, M. Hopkinson, R. C. Tozer, and G. J. Rees, "Impact ionization coefficients of  $\text{Al}_{0.8}\text{Ga}_{0.2}\text{As}$ ," *Applied Physics Letters*, **77** (26), p. 4374-6, 25 December 2000.
- [70] W. Shockley, "Problems related to p-n junctions in silicon," *Solid-State Electronics*, **2** (1), p. 35-67, 1961.
- [71] P. A. Wolff, "Theory of electron multiplication in silicon and germanium," *Physical Review*, **95**, p. 1415-20, 1954.
- [72] G. A. Baraff, "Distribution functions and ionization rates for hot electrons in semiconductors," *Physical Review*, **128**, p. 2507-17, 1962.
- [73] M. S. Shur, "GaN based transistors for high power applications," *Solid-State Electronics*, **42** (12), p. 2131-8, December 1998.
- [74] C. Bulutay, B. K. Ridley, and N. A. Zakhleniuk, "High-energy electron relaxation and full-band electron dynamics in aluminum nitride," *Physica B*, **314**, p. 63-7 2002.

- [75] W. J. Fan, M. F. Li, T. C. Chong, and J. B. Xia, "Electronic properties of zinc-blende GaN, AlN, and their alloys  $\text{Ga}_{1-x}\text{Al}_x\text{N}$ ," *Journal of Applied Physics*, **79** (1), p. 188-94, 1 January 1996.
- [76] P. G. Neudeck, "Progress in silicon carbide semiconductor electronics technology," *Journal of Electronic Materials*, **24** (4), p. 283-8, April 1995.
- [77] S. C. Binari, K. Doverspike, G. Kelner, H. B. Dietrich, and A. E. Wickenden, "Fabrication and characterization of GaN FETs," *Solid-State Electronics*, **41** (10), p. 1549-54, October 1997.
- [78] R. J. Trew, "Experimental and simulated results of SiC microwave power MESFETs," *Physica Status Solidi A*, **162** (1), p. 409-19, July 1997.
- [79] Y.-F. Wu, B. P. Keller, P. Fini, S. Keller, T. J. Jenkins, L. T. Kehias, S. P. Denbaars, and U. K. Mishra, "High Al-content AlGaIn/GaN MODFETs for ultrahigh performance," *IEEE Electron Device Letters*, **19** (2), p. 50-3, February 1998.
- [80] R. J. Trew, "SiC and GaN Transistors – Is there one winner for microwave power applications?" *Proceedings of the IEEE*, **90** (6), p. 1032-47, June 2002.
- [81] R. F. Davis, A. M. Roskowski, E. A. Preble, J. S. Speck, B. Heying, J. A. Freitas, Jr., E. R. Glaser, and W. E. Carlos, "Gallium Nitride materials – Progress, status, and potential roadblocks," *Proceedings of the IEEE*, **90** (6), p. 993-1004, June 2002.
- [82] P. G. Neudeck and L-Y Chen, "High-temperature electronics – A role for wide bandgap semiconductors?" *Proceedings of the IEEE*, **90** (6), p. 1065-76, June 2002.
- [83] F. Capasso, R. E. Nahory, and M. A. Pollack, "Temperature dependence of impact ionisation rates in GaAs between 20 degrees and 200 degrees C," *Electronics Letters*, **15** (4), p. 117-8, 15 February 1979.
- [84] X. G. Zheng, X. Sun, S. Wang, P. Yuan, G. S. Kinsey, A. L. Holmes, Jr., B. G. Streetman, and J. C. Campbell, "Multiplication noise of  $\text{Al}_x\text{Ga}_{1-x}\text{As}$  avalanche

photodiodes with high Al concentration and thin multiplication region,” *Applied Physics Letters*, **78** (24), p. 3833-5, 11 June 2001.

[85] L. S. Yeh, M. L. Lee, J. K. Sheu, M. G. Chen, C. J. Kao, G. C. Chi, S. J. Chang, and Y. K. Su, “Visible-blind GaN p-i-n photodiodes with an  $\text{Al}_{0.12}\text{Ga}_{0.88}\text{N}/\text{GaN}$  superlattice structure,” *Solid-State Electronics*, **47** (5), p. 873-8, May 2003.

[86] H.-E. Nilsson, U. Englund, M. Hjelm, E. Bellotti, and K. Brennan, “Full band Monte Carlo study of high field transport in cubic phase silicon carbide,” *Journal of Applied Physics*, **93** (6), p. 3389-94, 15 March 2003.

[87] M. V. Fischetti, Z. Ren, P. M. Solomon, M. Yang, and K. Rim, “Six-band  $\mathbf{k}\cdot\mathbf{p}$  calculation of the hole mobility in silicon inversion layers: Dependence on surface orientation, strain, and silicon thickness,” *Journal of Applied Physics*, **94** (2), p. 1079-95, 15 July 2003.

[88] G. B. Ren, Y. M. Liu, and P. Blood, “Valence-band structure of wurtzite GaN including the spin-orbit interaction,” *Applied Physics Letters*, **74** (8), p. 1117-9, 22 February 1999.

[89] A. Baldanzi and M. Goano, unpublished work.

[90] A. Baldanzi, “Electronic Structure and Transport Properties of 3C and 2H Silicon Carbide,” Master of Science Thesis, University of Illinois at Chicago, Chicago, IL, 2001.

[91] L. Tirino, M. Weber, K. F. Brennan, E. Bellotti, M. Goano, and P. P. Ruden, “Fully numerical Monte Carlo simulator for noncubic symmetry semiconductors,” *Journal of Computational Electronics*, **1**, p. 231-4, 2002.

[92] W. Quade, E. Sholl, and M. Rudan, “Impact ionization within the hydrodynamic approach to semiconductor transport,” *Solid State Electronics*, **36** (10), p. 1493-505, October 1993.

- [93] J. Kolník, I. H. Oğuzman, K. F. Brennan, R. Wang, and P. P. Ruden, "Calculation of the wave-vector-dependent interband impact-ionization transition rate in wurtzite and zinc-blende phases of bulk GaN," *Journal of Applied Physics*, **79** (11), p. 8838-40, 1 June 1996.
- [94] J. Bude, "Scattering mechanisms for semiconductor transport calculations," in The Monte Carlo Device Simulation: Full-Band and Beyond, K. Hess, Ed., Boston, MA: Kluwer, 1991, pp. 27-66.
- [95] T. Kunikyo, M. Takenaka, M. Morifuji, K. Taniguchi, and C. Hamaguchi, "A model of impact ionization due to the primary hole in silicon for a full band Monte Carlo simulation," *Journal of Applied Physics*, **79** (10), p. 7718-25, 15 May 1996.
- [96] N. Sano and A. Yoshii, "Impact-ionization theory consistent with a realistic band structure of silicon," *Physical Review B*, **45** (8), p. 4171-80, 15 February 1992-II.
- [97] Y. Wang and K. F. Brennan, "Semiclassical study of the wave vector dependence of the interband impact ionization rate in bulk silicon," *Journal of Applied Physics*, **75** (1), p. 313-9, 1 January 1994.
- [98] T. Kunikyo, M. Takenaka, Y. Kamakura, M. Yamaji, H. Mizuno, M. Morifuji, K. Taniguchi, and C. Hamaguchi, "A Monte Carlo simulation of anisotropic electron transport in silicon including full band structure and anisotropic impact-ionization model," *Journal of Applied Physics*, **75** (1), p. 297-312, 1 January 1994.
- [99] S. Brand and R. A. Abram, "Calculations of the commonly neglected terms in the matrix element for Auger and impact ionisation processes in semiconductors," *Journal of Physics C (Solid-State Physics)*, **17** (22), p. L571-4, 10 August 1984.
- [100] R. Wang, P. P. Ruden, J. Kolnik, I. Oguzman, and K. F. Brennan, "Dielectric properties of wurtzite and zincblende structure gallium nitride," *Journal of Physics and Chemistry of Solids*, **58** (7), p. 913-8, June 1997.



- [101] J. R. Madureira, D. Semkat, M. Bonitz, and R. Redmer, "Impact ionization rates of semiconductors in an electric field: The effect of collisional broadening," *Journal of Applied Physics*, **90** (2), p. 829-36, 15 July 2001.
- [102] S. E. Laux and M. V. Fischetti, "Numerical aspects and implementation of the DAMOCLES Monte Carlo device simulation program," in The Monte Carlo Device Simulation: Full-Band and Beyond, K. Hess, Ed., Boston, MA: Kluwer, 1991, pp. 1-26.
- [103] S. E. Laux, M. V. Fischetti, and D. J. Frank, "Monte Carlo analysis of semiconductor devices: The DAMOCLES program," *IBM Journal of Research and Development*, **34** (4), p. 466-93, July 1990.
- [104] H. K. Jung, K. Taniguchi, and C. Hamaguchi, "Impact ionization model for full band Monte Carlo simulation in GaAs," *Journal of Applied Physics*, **79** (5), p. 2473-80, 1 March 1996.
- [105] H.-E. Nilsson, private communication.
- [106] L. Tirino, M. Weber, K. F. Brennan, E. Bellotti, M. Goano, "Temperature dependence of the impact ionization coefficients in GaAs, cubic SiC, and zincblende GaN," *Journal of Applied Physics*, **94** (1), p. 423-30, 1 July 2003.
- [107] J. Kolník, I. H. Oğuzman, K. F. Brennan, R. Wang, and P. P. Ruden, "Monte Carlo calculation of electron initiated impact ionization in bulk zinc-blende and wurtzite GaN," *Journal of Applied Physics*, **81** (2), p. 726-33, 15 January 1997.
- [108] R. Mickevičius and J. H. Zhao, "Monte Carlo study of electron transport in SiC," *Journal of Applied Physics*, **83** (6), p. 3161-7, 15 March 1995.
- [109] E. Bellotti, H-E Nilsson, K. F. Brennan, and P. P. Ruden, "Ensemble Monte Carlo calculation of hole transport in bulk 3C-SiC," *Journal of Applied Physics*, **85** (6), p. 3211-7, 15 March 1999.

- [110] M. Yamanaka, H. Daimon, E. Sakuma, S. Misawa, and S. Yoshida, "Temperature dependence of electrical properties of  $n$ - and  $p$ -type 3C-SiC," *Journal of Applied Physics*, **61** (2), p. 599-603, 15 January 1987.
- [111] K. P. O'Donnell and X. Chen, "Temperature dependence of semiconductor band gaps," *Applied Physics Letters*, **58** (25), p. 2924-6, 24 June 1991.
- [112] Y. Ando, Y. Hori, W. Contrata, and N. Samoto, "Full band Monte Carlo simulation of temperature-dependent electron transport in gallium nitride," *Physica B*, **272** (1-4), p. 253-5, 1 December 1999.
- [113] K. Roze, N. A. Bannov, K. W. Kim, W. C. Holton, and M. A. Littlejohn, "Temperature dependence of impact ionization coefficients in  $p$ -Si," *Journal of Applied Physics*, **83** (9), p. 4988-90, 1 May 1998.
- [114] B. G. Streetman, Solid State Electronic Devices. Englewood Cliffs, NJ: Prentice Hall, 1995.
- [115] E. Bellotti, private communication.
- [116] M. Farahmand, M. Weber, L. Tirino, K. F. Brennan, "Theoretical study of direct-current and radio-frequency breakdown in GaN wurtzite- and zinc-blende-phase MESFETs (metal-semiconductor field-effect transistors)," *Journal of Physical Chemistry B: Condensed Matter*, **13**, p. 10477-86, 19 November 2001.
- [117] M. T. Weber, L. Tirino, and K. F. Brennan, "Comparison of zincblende-phase GaN, cubic-phase SiC, and GaAs MESFETs using a full-band Monte Carlo simulator," *IEEE Transactions on Electron Devices*, **50** (11), p. 2202-7, November 2003.
- [118] T. Kunikiyo, K. Ishikawa, Y. Inoue, Y. Kamakura, K. Taniguchi, and N. Kotani, "Model of hole-initiated impact-ionization rate in  $\alpha$ -quartz for a full band Monte Carlo simulation," *Journal of Applied Physics*, **94** (2), p. 1096-104, 15 July 2003.

- [119] Y. Wang, "Theory of Impact Ionization in Multiquantum Well Structures and its Application to the Modeling of Avalanche Photodiodes," Ph.D. dissertation, Georgia Institute of Technology, Atlanta, GA, May 1990.
- [120] S. M. Sze, Physics of Semiconductor Devices, 2<sup>nd</sup> Edition. New York, NY: Wiley Interscience, 1981.
- [121] P. Bhattacharya, Semiconductor Optoelectronic Devices, 2<sup>nd</sup> Edition. Englewood Cliffs, NJ: Prentice-Hall, 1997.
- [122] P. Yuan, K. A. Anselm, C. Hu, H. Nie, C. Lenox, A. L. Holmes, B. G. Streetman, J. C. Campbell, and R. J. McIntyre, "A new look at impact ionization – Part II: Gain and noise in short avalanche photodiodes," *IEEE Transactions on Electron Devices*, **46** (8), p. 1632-9, August 1999.
- [123] R. J. McIntyre, "Multiplication noise in uniform avalanche photodiodes," *IEEE Transactions on Electron Devices*, **ED-13** (3), p. 164-8, January 1966.
- [124] M. M. Hayat, W. L. Sargeant, and B. E. A. Saleh, "Effect of dead space on gain and noise in Si and GaAs avalanche photodiodes," *IEEE Journal of Quantum Electronics*, **28** (5), p. 1360-5, May 1992.
- [125] M. A. Saleh, M. M. Hayat, B. E. A. Saleh, and M. C. Teich, "Dead-space-based theory correctly predicts excess noise factor for thin GaAs and AlGaAs avalanche photodiodes," *IEEE Transactions on Electron Devices*, **47** (3), p. 625-33, March 2000.
- [126] D. S. Ong, K. F. Li, G. J. Rees, G. M. Dunn, J. P. R. David, and P. N. Robson, "A Monte Carlo investigation of multiplication noise in thin  $p^+i-n^+$  GaAs avalanche photodiodes," *IEEE Transactions on Electron Devices*, **45** (8), p. 1804-10, August 1998.
- [127] G. Satyanadh, R. P. Joshi, N. Abedin, and U. Singh, "Monte Carlo calculation of electron drift characteristics and avalanche noise in bulk InAs," *Journal of Applied Physics*, **91** (3), p. 1313-8, 1 February 2002.

- [128] K. F. Li, D. S. Ong, J. P. R. David, G. J. Rees, R. C. Tozer, P. N. Robson, and R. Grey, "avalanche multiplication noise characteristics in thin GaAs  $p^+i-n^+$  diodes," *IEEE Transactions on Electron Devices*, **45** (10), p. 2102-7, October 1998.
- [129] F. Ma, S. Wang, X. Li, K. A. Anselm, X. G. Zheng, A. L. Holmes, Jr., and J. C. Campbell, "Monte Carlo simulation of low-noise avalanche photodiodes with heterojunctions," *Journal of Applied Physics*, **92** (8), p. 4791-5, 15 October 2002.